AD621501

UACRL D-920252-6

INVESTIGATION OF BASIC CONTAMINANT REACTIONS IN RE-ENTRY WAKES

FINAL REPORT
JUNE 1965

SEP 22 1965
TISIA B

BY

United Aircraft Research Laboratories
UNITED AIRCRAFT CORPORATION
EAST HARTFORD, CONNECTICUT

CLEARINGHOUSE
FOR FEDERAL SCIENTIFIC AND
TECHNICAL INFORMATION
Hardcopy | Microfiche
$3.00 | $0.75 | 85 pp
PROCESSING COPY

SPONSORED BY

ADVANCED RESEARCH PROJECTS AGENCY
PROJECT DEFENDEP
ARPA ORDER NO. 553

ARCHIVE COPY

UNITED AIRCRAFT CORPORATION
Research Laboratories
East Hartford, Connecticut

Report No.: D-920252-6
Date of Reporting Period: June 1, 1964, to May 31, 1965

INVESTIGATION OF THE BASIC CONTAMINANT REACTIONS IN RE-ENTRY WAKES

This research was supported by the Advanced Research Projects Agency (Project DEFENDER) and was monitored by the U. S. Army Research Office - Durham under Contract DA-31-124-ARO-D-221.

Reported By: R. H. Bullis
R. H. Bullis

R. J. Andersen
R. J. Andersen

T. L. Churchill
T. L. Churchill

V. E. Grob
V. E. Grob

Approved By: H. D. Taylor
H. D. Taylor, Manager
Physics Department

Date: June 28, 1965

Report D-920252-6

Final Report Under
Contract DA-31-124-ARO-D-221
for the Period of June 1, 1964, through May 31, 1965

Investigation of the Basic Contaminant Reactions in Re-entry Wakes

TABLE OF CONTENTS

	Page
SUMMARY	1
ELECTRON-MOLECULE COLLISION FREQUENCY MEASUREMENTS	2
Introduction	2
Theory of Microwave Power Absorption in a Plasma Under Cyclotron Resonance Conditions	3
Outline of Experiment	9
Thermochemical Calculations	14
Experimental Measurements and Results	16
Summary	17
ION-MOLECULE TOTAL COLLISION CROSS-SECTION MEASUREMENTS	18
Introduction	18
Outline of Experimental Technique	18
Description of Experimental Components	19
Experimental Results	24
Atmospheric Gas Ion Source	27
Summary	27
ELECTRON ATTACHMENT INVESTIGATIONS	29
Introduction	29
Outline of Experimental Technique	29
Experimental Results	33
Summary	35
REFERENCES	36
LIST OF FIGURES	38
FIGURES	41

Summary

The results obtained from a basic research program conducted by the United Aircraft Research Laboratories during the period from June 1, 1964, through May 31, 1965, under Contract DA-31-124-ARO-D-221 to investigate the basic contaminant reactions in re-entry wakes are summarized herein. Three different experimental laboratory investigations were conducted to determine the effect of the presence of impurities which exist in re-entry wakes in the form of alkali metals and their compounds on the electron number density and effective collision frequency.

In the first experimental investigation, electron cyclotron resonance techniques were used to measure the equilibrium electron number density and effective electron collision frequency in sodium hydroxide vapor over the energy range from 0.09 to 0.126 eV. The equilibrium number densities detected in these experimental investigations indicate that by using the JANAF thermochemical data, an electron concentration is predicted which is an order of magnitude higher than the present experimental results at 1200°K and a factor of 5 higher at 1466°K for sodium hydroxide pressures of 1 to 10 mm. The effective cross section determined from these measurements, which shows a strong velocity dependence, is approximately 10 cm^{-1} mm^{-1}.

In the second investigation, a modified Ramsauer beam experiment was used to determine the total collision cross section of sodium ions with several of the atmospheric constituents, such as oxygen, nitrogen, and nitric oxide, over the energy range of 1.08 to 10.35 eV. The cross section for these interactions ranges from 65 cm^{-1} mm^{-1} at energies of 10 eV to approximately 310 cm^{-1} mm^{-1} at energies of 1.08 eV. The energy dependence of the cross sections indicates that no chemical reactions occur between sodium ions and the various atmospheric species at these energies.

In the third investigation, a crossed-beam double modulation technique, in which an electron beam was interacted with a molecular beam of sodium hydroxide, was used to study negative ion production by electron impact. Over the electron energy range of 0.05 eV to 10 eV, negative currents were detected which could be directly attributable to the interaction of the two beams. The magnitude of the cross section for the interaction exhibits a maximum of 3 x 10^{-16} cm^2 at an energy slightly less than 2 eV. Further investigations are required to definitively determine the species formed by the interaction.

ELECTRON-MOLECULE COLLISION FREQUENCY MEASUREMENTS

Introduction

The electrical transport properties of re-entry wakes which influence the effective radar cross section are determined by the magnitude of the electron density and the electron collision frequency for momentum transfer. A knowledge of these two parameters is fundamental to an understanding of the physics and chemistry of such flows and reactions. Of particular interest are the transport properties of the alkali metals and many of their compounds because alkali metal impurities in re-entry wakes can cause significant increases in the electron concentration.

The most versatile and accurate methods for the determination of very low-energy electron collision cross sections and low electron concentrations are microwave techniques. Of these, the electron-cyclotron resonance microwave technique (Refs. 1, 2, 3) is the most sensitive. With this technique, independent measurements can be made of electron density and collision frequency. The collision frequency is determined from measurements of the line width of the microwave cyclotron resonance absorption spectrum, and the electron density is determined from measurements of the absolute magnitude of the absorption together with the total area of the absorption curve.

Because of the extremely high sensitivity that can be achieved with the electron-cyclotron resonance technique, the properties of plasmas with low degrees of ionization can be investigated. For the case of the alkali metals and several of their compounds, sufficient ionization can be produced solely by thermal oven heating of the vapor of these materials, due to their low ionization potential, to produce detectable signal levels. Because a true equilibrium plasma can be generated by simple oven heating of the vapor under study, it is insured that in complex systems, such as sodium hydroxide, various species are not preferentially produced over those that would be present under conditions of true thermodynamic equilibrium.

The purpose of the present investigation was to experimentally determine the electron number density and the effective collision frequency existing in a thermally generated sodium hydroxide plasma over the temperature range of 1000° to 1500°K. These measurements were to be made using cyclotron resonance techniques similar to those previously employed to measure the collision frequency of electrons in cesium vapor over the energy range of 0.05 eV to 1.0 eV.[4] One of the results generated by this experimental investigation was that the electron concentration was lower by a factor of 10 at a temperature of 1200°K and lower by a factor of about 5 at a temperature of 1466°K compared to that predicted by thermodynamic calculations based upon the JANAF thermochemical data. Measurements

indicated that less than 10^5 electrons cm^{-3} are generated at 1200°K in this vapor even with pressures between 1 and 10 mm, but between 10^7 to 10^8 electrons are generated around 1466°K for the same pressures. It was also determined that the collision frequencies measured indicate a rather low cross section, approximately 2.5×10^{-16} cm^2, for momentum transfer collisions in the superheated mixture. Also the measured difference between the dc and ac collision frequencies indicates a rather strong velocity dependence on this cross section.

Theory of Microwave Power Absorption in a Plasma Under Cyclotron Resonance Conditions

When the cyclotron frequency of the electron is equal to the frequency of an applied microwave electric field, the collective motion of a group of electrons is in phase with their acceleration due to the applied microwave electric field, and they are able to absorb an appreciable amount of the rf power. The shape of such a cyclotron absorption curve as a function of frequency in a fixed magnetic field is related to the electron heavy-particle collision frequency, and the total power absorbed integrated over all frequencies is directly related to the electron density. The area of the integrated power absorption spectrum is independent of the velocity dependence of the collision frequency so that the electron density can be readily measured independent of the species involved.

A good electrical analogy of a plasma in a dc magnetic field is a simple electrical inductance and capacitance (L-C) tank circuit. If there is no resistance in this tank circuit, the frequency response for power absorption is monochromatic. The inclusion of resistance in the tank circuit lowers the Q of the circuit and broadens the spectral line width. The magnitude of the line width can be directly related to the magnitude of the resistance in the tank circuit. Electron collisions play the same role as the resistance in the tank circuit. They represent a viscous damping force on the motion of the electrons and contribute to the real part of the complex electrical conductivity.

The equation describing the electron current flow through a plasma under the combined influence of electric and magnetic fields may be derived on the basis of the physical model for a plasma originally developed by Lorentz.[5,6] In this approach it is assumed that collisions are instrumental in setting up a nearly spherically symmetric velocity distribution of electrons and that small deviations from spherical symmetry are described accurately enough by the second term in the spherical harmonic expansion of the velocity distribution function. Upon substitution of this first order expansion into the Boltzmann equation, two coupled equations containing the terms of the expansion result. If it is assumed that a long wavelength electromagnetic wave is propagating through the plasma in

the "x" direction, that the ac electric field associated with the wave is along the "y" direction, and that an applied dc magnetic field points along the "z" direction, the relationship between terms of this expansion and the equation for particle current result in the following expression relating electron current density to electric field

$$\vec{J} = \frac{4\pi}{3} \cdot \frac{n_e e^2}{m} E_y \int_0^\infty \left[\frac{-\omega_b}{(\nu(v) + j\omega)^2 + \omega_b^2} \hat{i} + \frac{\nu(v) + j\omega}{(\nu(v) + j\omega)^2 + \omega_b^2} \hat{j} \right] \frac{\partial f_o}{\partial v} v^3 dv \qquad (1)$$

where

m - electron mass
e - electronic charge
v - electron velocity
n_e - electron number density
J - current density
E_y - electric field intensity
f_o - isotropic part (first term in spherical harmonic expansion) of the velocity distribution function normalized to unity
$\nu(v)$ - elastic electron-atom collision frequency for momentum transfer
ω - radian frequency of electromagnetic wave
ω_b - electron-cyclotron frequency = eB_z/m (where B_z is the dc magnetic flux density)
$\hat{i},\hat{j},\hat{k}$ - unit vectors in the x, y, and z directions
j - $\sqrt{-1}$

In this derivation it has been assumed that the ac magnetic fields are negligible in comparison with the applied dc magnetic field, that the plasma is homogeneous, that the collision friction force exerted on electrons is due to elastic momentum transfer encounters with neutral particles, and that electron-electron encounters have no direct influence on the momentum of the electron gas. The form of the electric field used in the derivation of Eq. 1 is given by

$$\vec{E} = \hat{j} E_y(z,y) e^{j(\omega t + kx)} \qquad (2)$$

where

t - time
k - phase constant of the electromagnetic wave

The average electromagnetic power absorbed by the plasma is given by

$$P_{abs} = -1/2 \mathrm{Re} \int_V \vec{E}^* \cdot \vec{J}\, dV \qquad (3)$$

Pabs - power absorbed
E^* - complex conjugate of electric field intensity
V - volume occupied by plasma
R_e - "real part of"

Combining Eqs. 1, 2, and 3 results in the following expression for the absorbed power

$$P_{abs} = \frac{-2\pi}{3}\frac{e^2}{m}\int_V\int_0^\infty E_y^2(z,y)n_e \frac{\nu(v)\left[\nu^2(v)+\omega^2+\omega_b^2\right]}{\left[\nu(v)^2+(\omega-\omega_b)^2\right]\left[\nu(v)^2+(\omega+\omega_b)^2\right]}\cdot\frac{\partial f_o}{\partial v}\,v^3\,dv\,dV \tag{4}$$

It will now be assumed that the plasma under consideration fills a portion of a rectangular waveguide as in Fig. 1. In the absence of plasma the waveguide propagates the dominant transverse electric mode which is given by[7]

$$\vec{E} = \hat{j}E_o \sin\frac{\pi z}{a}e^{j(\omega t+kx)} \tag{5}$$

where

E_o - maximum amplitude of the electric field intensity
a - waveguide width in "z" direction

If it is assumed that the plasma is so rare (fractional power absorbed per wavelength << 1) that the electric field is unperturbed by the presence of the plasma, then from Eqs. 2, 4, and 5 the power absorbed becomes

$$P_{abs} = -\frac{2\pi}{3}\cdot\frac{e^2}{m}\int_V\int_0^\infty E_o^2\sin^2\frac{\pi z}{a}\,n_e\,\frac{\nu(v)\left[\nu^2(v)+\omega^2+\omega_b^2\right]}{\left[\nu^2(v)+(\omega-\omega_b)^2\right]\left[\nu^2(v)+(\omega+\omega_b)^2\right]}\cdot\frac{\partial f_o}{\partial v}\,v^3\,dv\,dV \tag{6}$$

In the analytical development leading up to Eq. 6, it was assumed that the plasma was homogeneous. For the case of the rarefied plasma under consideration, gradients may exist. However, because there are no significant plasma gradients in the direction of the electric field and because of the tenuous nature of the plasma, the plasma behaves as though it were homogeneous and a simple averaging process can be used to account for gradients in electron density. Therefore, Eq. 6 becomes

$$P_{abs} = -\frac{2\pi}{3}\frac{e^2}{m}\int_x\int_y\int_0^a\int_0^\infty E_o^2\sin^2\frac{\pi z}{a}\,n_e(x,y)\,\frac{\nu(v)\left[\nu(v)^2+\omega^2+\omega_b^2\right]}{\left[\nu^2(v)+(\omega-\omega_b)^2\right]\left[\nu^2(v)+(\omega+\omega_b)^2\right]}\,\frac{\partial f_o}{\partial v}\,v^3\,dv\,dz\,dx\,dy \tag{7}$$

where the electron density has been assumed uniform in the "z" direction. Upon integration Eq. 7 becomes

$$P_{abs} = -\frac{\pi}{6}\frac{(eE_0)^2}{m} N_e \left[\underbrace{\int_0^\infty \frac{\nu(v) v^3 \partial f_0/\partial v}{\nu^2(v) + (\omega - \omega_b)^2} dv}_{\text{resonant term}} + \underbrace{\int_0^\infty \frac{\nu(v) v^3 \partial f_0/\partial v}{\nu^2(v) + (\omega + \omega_b)^2} dv}_{\text{nonresonant term}} \right] \quad (8)$$

where

N_e - total number of electrons in the waveguide

It is apparent from Eq. 8 that near resonance ($\omega \sim \omega_b$) the resonant term will be much larger than the nonresonant term when the square of the radian frequency of the electric field is much larger than the square of the collision frequency, i.e., ($\omega^2 \sim \omega_b^2 \gg \nu^2(v)$). Therefore, near resonance the power absorbed becomes

$$P_{abs} = -\frac{\pi}{6}\frac{(eE_0)^2}{m} N_e \int_0^\infty \frac{\nu(v) v^3 \partial f_0/\partial v}{\nu^2(v) + (\omega - \omega_b)^2} dv \quad (9)$$

The power absorption will exhibit resonance behavior whenever the cyclotron frequency equals the microwave radian frequency. This condition can be achieved by holding the applied microwave frequency constant and varying the applied magnetic field, which was the method employed in this experiment.

The area under the absorption curve of Fig. 1 is given by

$$A = \int_{-\infty}^{\infty} P_{abs}\, d\Omega = -\frac{\pi}{6}\frac{(eE_0)^2}{m} N_e \int_{-\infty}^{\infty}\int_0^\infty \frac{\nu(v) v^3 \partial f_0/\partial v}{\nu^2(v) + \Omega^2} dv\, d\Omega \quad (10)$$

where

A - area under absorption curve

Ω - $\omega - \omega_b$

Since Ω and v are independent, the order of integration is immaterial. Integrating first with respect to Ω yields

$$A = -\frac{\pi}{6}\frac{(eE_0)^2}{m} N_e \cdot \frac{\pi}{2} \int_0^\infty v^3 \partial f_0 / \partial v dv \quad (11)$$

Of significance is the fact that the velocity dependent collision frequency has been canceled by the first integration. Integrating with respect to electron velocity yields

$$A = \frac{\pi}{8}\frac{(eE_0)^2}{m} N_e \quad (12)$$

Equation 12 points out the significant fact that the area under the absorption curve is, subject to the assumptions outlined previously, directly proportional to the total number of electrons in the plasma-filled waveguide, independent of the form of the velocity-dependent collision frequency or the form of the isotropic part of the velocity distribution function. Since the electric field strength and the volume of the plasma container are presumed to be known, the electron density can be determined from a measurement of the area under a single absorption curve.

The average power incident on the plasma for the case of the dominant TE_{01} mode propagation can be shown to be[7]

$$P_{INC} = \sqrt{\frac{\epsilon_o}{\mu_o}} \left(1 - \frac{\omega_c^2}{\omega^2}\right)^{\frac{1}{2}} \frac{E_o^2 ab}{4} \tag{13}$$

where

P_{inc} - power incident
E_o - permittivity of free space
μ_o - permeability of free space
ω_c - cutoff radian frequency ($\omega_c = \pi/a\sqrt{\mu_o \epsilon_o}$)
b - waveguide dimension in "y" direction

The fractional power absorbed is now defined

$$\frac{P_{INC} - P_{OUT}}{P_{INC}} = \frac{P_{abs}}{P_{INC}} \tag{14}$$

where

P_{out} - power incident on plasma reduced by the power absorbed

Integrating this expression over Ω as in Eq. 10 results in the following combination of Eqs. 12 and 13

$$\frac{\int_{-\infty}^{\infty} P_{abs}\, d\Omega}{P_{INC}} = A^* = \frac{\pi}{2} \frac{e^2}{m} \sqrt{\frac{\mu_o}{\epsilon_o}} \frac{N_e}{ab} \left(1 - \frac{\omega_c^2}{\omega^2}\right)^{-\frac{1}{2}} \tag{15}$$

Therefore, the electron density becomes

$$n_e = \frac{N_e}{V} = A^* \frac{2}{\pi} \frac{m}{e^2} \sqrt{\frac{\epsilon_o}{\mu_o}} \frac{ab \left(1 - \omega_c^2/\omega^2\right)^{1/2}}{V} \tag{16}$$

where

A^* - area under absorption curve normalized with respect to the incident power

V - volume of plasma container

Equation 16 relates the electron density directly to the normalized area under the absorption curve; all other quantities in Eq. 16 are known.

If it is now assumed that the isotropic part of the electron velocity distribution is Maxwellian and this form is combined with Eqs. 9 and 10, the following expression results

$$\frac{P_{abs}}{P_{inc}} = \frac{e^2}{2m}\sqrt{\frac{\mu_0}{\epsilon_0}}\frac{N_e}{ab}\left(1-\frac{\omega_c^2}{\omega^2}\right)^{-1/2}\frac{8}{3\sqrt{\pi}}\left(\frac{m}{2kT_e}\right)^{5/2}\int_0^\infty \frac{\nu(v)v^4 e^{-\frac{mv^2}{2kT_e}}}{\nu^2(v)+\Omega^2}\,dv \tag{17}$$

where

T_e - electron temperature (equal to the background gas temperature under thermodynamic equilibrium conditions)

At resonance $\Omega = 0$, and Eq. 17 becomes

$$\left.\frac{P_{abs}}{P_{inc}}\right|_{\Omega=0} = \frac{e^2}{2m}\sqrt{\frac{\mu_0}{\epsilon_0}}\frac{N_e}{ab}\left(1-\frac{\omega_c^2}{\omega^2}\right)^{-1/2}\frac{8}{3\sqrt{\pi}}\left(\frac{m}{2kT_e}\right)^{5/2}\int_0^\infty \frac{v^4 e^{-\frac{mv^2}{2kT_e}}}{\nu(v)}\,dv \tag{18}$$

which defines an effective dc collision frequency.[8] Therefore,

$$\left.\frac{P_{abs}}{P_{inc}}\right|_{\Omega=0} = \frac{e^2}{2m}\sqrt{\frac{\mu_0}{\epsilon_0}}\frac{N_e}{ab}\left(1-\frac{\omega_c^2}{\omega^2}\right)^{-\frac{1}{2}}\nu_{eff(dc)}^{-1} \tag{19}$$

Well off resonance, $\Omega^2 >> \nu^2/v)$ and Eq. 17 becomes

$$\left.\frac{P_{abs}}{P_{inc}}\right|_{\Omega^2>>\nu^2} = \frac{e^2}{2m}\sqrt{\frac{\mu_0}{\epsilon_0}}\frac{N_e}{ab}\left(1-\frac{\omega_c^2}{\omega^2}\right)^{-\frac{1}{2}}\frac{1}{\Omega^2}\frac{8}{3\sqrt{\pi}}\left(\frac{m}{2kT_e}\right)^{\frac{5}{2}}\int_0^\infty \nu(v)v^4 e^{-\frac{mv^4}{2kT_e}}\,dv \tag{20}$$

As in the previous case, an ac effective collision frequency can be defined.

$$\left.\frac{P_{abs}}{P_{inc}}\right|_{\Omega^2>>\nu^2} = \frac{e^2}{2m}\sqrt{\frac{\mu_0}{\epsilon_0}}\frac{N_e}{ab}\left(1-\frac{\omega c^2}{\omega^2}\right)^{-\frac{1}{2}}\frac{\nu_{eff(ac)}}{\Omega^2} \tag{21}$$

Equations 19 and 21 relate the power absorbed by the plasma to an effective collisional parameter, which describes the over-all resistive effect of collisions. Near resonance the cyclotron motion of the electrons is in phase with their motion due to the electric field, collisions impede power absorption, and the plasma behaves as in the dc case. Far removed from resonance, collisions enhance the power absorption, and the plasma behaves as in the standard ac case.[6] Although the effective collision frequencies defined by the previous equations are useful plasma parameters, it should be noted that the averaging of the actual velocity dependent collision frequency is different for each case, and consequently,

the ac and dc effective collision frequencies are not equal. However, if the velocity-dependent collision frequency is not a strong function of electron velocity over the range of interest, the ac and dc effective collision frequencies are approximately the same, effectively independent of the averaging process.

The total momentum transfer collision frequency arising from a mixture of different chemical species is related to the various momentum transfer collision cross sections by the following relationship:

$$\nu(v) = \sum n_j Q_{ej}(v) v \qquad (22)$$

where

n_j - neutral particle density of the j^{th} species
Q_{ej} - momentum transfer cross section for electrons and molecules of the j^{th} species

Thus it is apparent from Eq. 22 and Eq. 17 for the fractional power absorbed that an analysis of cyclotron resonance absorption spectra (fractional power absorbed vs. Ω) can result in information leading to the determination of the momentum transfer cross sections. The extraction of the cross section from the integral equation is quite difficult and usually requires considerable numerical experimentation in order to generate a cross-section curve which will be consistent with the measured transport property (i.e., microwave attenuation). However, this information is not really desired in this study. The two important measurables in this case are the effective collision frequency, which can be used directly to estimate microwave absorption and reflection coefficients in re-entry plasmas and the measurement of the equilibrium electron density as a verification of the JANAF thermochemical data.

Outline of Experiment

Microwave System

Conventional microwave spectroscopy techniques are usually designed to provide a spectral display where the principal parameters to be measured are line structure and resonant frequency. If the magnitude of the interaction is to be measured, the customary approach has been to compare the observed line to that of a standard also housed in the waveguide measurement region. This is not possible in microwave cyclotron resonance measurements in plasmas.

As has been pointed out in the theory, the approach in this experiment instead has been to compare the absorption magnitude with a similar change introduced by a very precise and accurate attenuator. This was accomplished by using a parallel substitution technique in a microwave bridge. A description

and analysis of this attenuator is given in the next subsection.

A block diagram of the apparatus is shown in Fig. 2. In taking data, the microwave bridge was first nulled out for zero signal and then the magnetic field scanned automatically. The resultant unbalance as cyclotron resonance was approached was recorded directly. Finally, two time sweeps were superimposed on the recording, first with the bridge nulled and then with it unbalanced by a known amount as determined by the attenuator. Since the microwave bridge output was linear for small unbalances, the ordinate sensitivity was readily calculated in fractional absorption per inch of displacement. The abscissa was determined by the current flowing through the magnet which was directly proportional to the magnetic field generated. This proportionality constant was determined in a calibration using an N.M.R. gaussmeter accurate to 1 part in 10^5. Once nulled, this bridge would drift less than an equivalent power change of 5 parts in 10^4 over a three-minute period. The noise level (which determines the sensitivity) was equivalent to a power change of 1 part in 10^4. This level, together with the minimum line width, determined the minimum electron density which could be detected.

For a plasma of finite size, several effects other than volume collisions can broaden the cyclotron absorption line. Magnetic field inhomogeneities over the sample volume produce a distribution of cyclotron frequencies resulting in an instrumental line width in the absence of collisions. Estimates of this effect based upon the N.M.R. magnet calibration yielded a full width at half power of about 2 gauss. Doppler broadening of the line width can be produced by electrons traveling toward or away from the direction of microwave propagation. However, Doppler broadening effects are small in comparison to pressure broadening when the ratio of the collision frequency to the frequency of the microwave signal is large compared with the electron velocity to the speed of light. It was easily estimated that this condition held for the experimental temperatures involved. At low pressures where the electron mean free path is comparable to the dimension of the container, along the direction of the magnetic field, electron collisions with the walls establish a minimum line width which is termed transit time broadening. This particular mechanism seemed to be the one which generated the observed minimum line width of about 3.5 gauss. Lastly, significant heating of the plasma by the probing microwave field can produce a broadening of the line width and also change the validity of the assumption that the electron temperature is equal to the gas temperature. To show that the cyclotron heating was negligible compared to the ambient gas temperature required that[6]

$$\frac{E^2}{12}\frac{M}{m}\frac{e^2}{m^2}\frac{1}{\nu^2} \ll kT_g \qquad (23)$$

where

E - electric field strength of the microwave
T_g - temperature of the gas

This condition is easily satisfied by using a power level of 10^{-9} watts in the microwave bridge.

Using measured minimum line widths together with the minimum detectable signal yielded a sensitivity of the apparatus of 10^5 electrons/cm^3.

Microwave Bridge Attenuator

This device is used to produce minute power changes of microwaves with a high degree of accuracy and precision with excellent reproducibility. A block diagram of the bridge is shown in Fig. 3. This apparatus works by splitting the microwave signal into two paths. One path contains two rotary vane precision attenuators and the other a rotary vane precision phase shifter. The upper arm as shown in the block diagram is capable of transmitting a highly attenuated signal with respect to the lower arm by setting one attenuator for high levels of absorption. For this reason a small variation in the power output can be simulated with a readable large variation in the other control attenuator. The minimum change that can be produced is only limited by the magnitude of the fixed attenuation in the upper arm and the stability of the microwave source and various microwave components. The phase shifter is merely used to combine the signals in phase which simplifies the analysis of the device. To obtain good agreement between a predicted power variation and the measured value, it was found that the arms of the bridge must be sufficiently isolated from each other by at least 60 db of attenuation, and that the fixed transmission coefficient of each arm must be accurately known.

Analysis of the bridge attenuator was carried out in the following manner. The vector fields are the quantity which combines from the upper and lower paths to produce the output power from the device. Therefore, the analysis must be expressed in terms of the fields. As pointed out above, the inclusion of a phase shifter in the device expedites the formulation, in that once the output is maximized with the phase shifter, the addition of the vectors can be treated as addition of scalars, where only the magnitudes are important. This approach is valid as long as the attenuators do not introduce any phase shift as they are varied. The rotary vane attenuators used in this experiment introduced only about 3° phase shift from one end of the scale to the other. This was small enough to neglect. The electric field into the device is divided into the upper and lower arms by the 3 db coupler so that

$$E_{in} = \gamma E_o + \delta E_o \qquad \text{where} \quad \gamma + \delta = 1$$
$$= E_{upper} + E_{lower} \tag{24}$$

As the microwaves pass through the device, both upper and lower waves are attenuated. For the top wave there is some minimum insertion loss that results even with the attenuators set equal to 0 db so that the field is reduced by some fraction. Then there is the deliberate attenuation introduced by the attenuators.

Superimposing these effects, the reduced field strength just before the waves combine is given by

$$E'_{upper} = \alpha\beta\rho\gamma E_0 \tag{25}$$

where

α - transmission coefficient of the first attenuator
β - transmission coefficient of the second attenuator
ρ - transmission coefficient due to insertion losses in the upper arm

The bottom wave is similarly attenuated by some insertion loss so that

$$E'_{lower} = \mu\delta E_0 \tag{26}$$

where

μ - transmission coefficient due to insertion losses in the lower arm

Combining these two waves at the output directional coupler yields the output electric field strength

$$E_{out} = E'_{upper} + E'_{lower} = (\alpha\beta\rho\gamma + \mu\delta)\ E_0 \tag{27}$$

Expressing these results in terms of power-in and power-out, because these are the real quantities that are measured by microwave detectors, yields

$$\frac{P_{OUT}}{P_{IN}} = (\alpha^2\beta^2\rho^2\gamma^2 + \mu^2\delta^2 + 2\alpha\beta\rho\mu\delta\gamma) \tag{28}$$

To evaluate these constants the power transmitted through the device must be measured when the attenuators are set at 0 db ($\alpha = \beta = 1.00$). Power through the top arm alone also must be measured. For this purpose a shorting switch was included.

Calibration was performed using a thermoelectric type of microwave power detector, which had good square law response over a wide dynamic range and excellent temperature stability. A number of experimental measurements of the power-in and the power-out yielded determinations of the products

$$\rho^2\gamma^2 = .155 \pm .001$$

$$\text{and } \mu^2\delta^2 = .206 \pm .001$$

With the first attenuator set at 0 db ($\alpha^2 = 1.00$) the second attenuator was varied in 1-db steps, and the combined power measured. Comparing these

experimental results with the numbers which would be calculated on the basis of the attenuator dial setting and the insertion loss coefficients yields agreement closer than one per cent. Experimentally, it made no difference which attenuator was designated number one or number two. Thus when the first attenuator was set on 10, 20, or 30 db to reduce the effect of attenuator number two, high confidence could be place on the calculated effect of varying attenuator number two.

In using this device with the microwave spectrometer, only differences in power outputs are important so that the final analytical expression for determining power differences is

$$\frac{P_{out} - P_{out}'}{P_{in}} = (\alpha^2 - \alpha'^2)(\beta^2\rho^2\gamma^2) + (\alpha - \alpha')(2\beta\rho\mu\delta\gamma) \qquad (29)$$

Using the specified accuracy of the attenuators, together with the error associated in determining the insertion losses, yielded a probable error for specifying a given power change of about 1 to 2 per cent.

Measurement Cell

The sodium hydroxide plasma was contained in a high-purity magnesium oxide tube, shown in Fig. 4. This material was found to be nearly unique in that it did not react chemically with the sodium hydroxide, was capable of operating at 1500°K, was vacuum tight, and maintained a reasonably constant dielectric strength with a low loss tangent at microwave frequencies and high temperatures. The top section of the tube was inserted through the narrow wall of an X Band (9.375 kmcs) waveguide section containing one-half inch tubular projections on each side which represented waveguide beyond cutoff to the probing microwave signal. The main body of the tube carried the sodium hydroxide vapor between upper and lower oven chambers. The upper oven chamber heated the whole middle portion of the waveguide section and magnesia tube to a uniform high temperature which in effect superheated the NaOH vapor. The bottom oven chamber, which was much cooler, established the total vapor pressure of the system. The bottom section of the magnesia tube contained the solid and molten sodium hydroxide. Both upper and lower ovens were surrounded by a high-vacuum stainless steel shell which provided the measurement cell with thermal isolation. A picture of the vacuum chamber as it fits between the pole pieces of the magnet is shown in Fig. 5. The procedure for working with the chemical was to load the bottom portion of the magnesia tube with sodium hydroxide pellets and assemble the vacuum system leaving the bottom piece and middle piece of the tube separated. By pumping on the system and heating the bottom and top ovens to around 250°C, all excess water vapor was driven off. Then the two pieces were pressed together using a mechanical feedthrough.

The pressed joint at these two lapped surfaces had been previously checked for pressure tightness, and a leak conductance of 10^{-5} l/sec was measured. This leak conductance was small enough to insure that the pressure inside the tube was effectively that of the true vapor pressure.

The temperatures of the upper and lower portion of the measurement cell were measured using chromel-alumel thermocouples. The upper oven temperature was found to be constant within 10^{o}K over the volume occupied by the measurement cell. The very low coefficient of thermal conductivity in the Inconel waveguide that was used helped maintain this temperature uniformity and also reduced heat losses to the outside. In order to stop self-welding of metal parts at these high temperatures, boron nitride was used as a lubricant on the surfaces.

Even though the magnesia tube had a dielectric strength of relatively fixed magnitude with respect to temperature variation, the magnitude of that constant ($\epsilon \cong 10$) was such that a large portion of the microwave signal was reflected from the interface. In order to reduce this reflection to a negligible value so it would not mask the true absorption, symmetrical tuning screws were placed on each side of the ceramic tube through the broad side of the waveguide. This reduced the reflection coefficient to less than 1×10^{-3}. These tuning screws were attached to long shafts that fed through the top flange to the outside of the oven. This allowed tuning to be done under vacuum at operating temperatures. Because the plasma was so tenuous, there was very little change in the reflection coefficient at resonance. Consequently, true absorption was measured by the microwave attenuation.

Thermochemical Calculations

Prior to making electron density and electron collision frequency measurements, a computer program was initiated to predict the various species concentrations in the superheated sodium hydroxide vapor. These predictions were based on the most recent JANAF thermochemical data for seventeen possible equilibria. The species considered were: NaOH, $(NaOH)_2$, Na, H_2O, O_2, NaO, OH, H_2, O, H, Na^+, electrons, Na_2, NaH, OH^-, O^-, H^-. Figures 6 to 20 show the concentration of each species as a function of temperature. The main parameter in this analysis was the total vapor pressure of the system. It was seen for the temperature range considered (1000^{o}K to 1600^{o}K) the order of species concentration does not change except for the position of $(NaOH)_2$. As pressure is lowered with fixed temperature, the dimer tends to separate back to the monomer state. The predominant species was the NaOH monomer at all temperatures and pressures considered. The concentration of the next most prevalent species, sodium vapor and water vapor, was an order of magnitude smaller.

Generation of free electrons in the mixture comes directly from the following reaction

$$Na \rightleftharpoons Na^{+} + e \qquad (30)$$

because of the low ionization potential of sodium and because of the predominance of that species. It should be pointed out that the calculation of electron concentration using the thermodynamic equilibrium constant was entirely equivalent to calculating the percentage ionization of sodium vapor by means of the Saha equation. And since it turned out that electron attachment by OH, O, and H was quite small in the NaOH vapor, one check on the computer solution of the seventeen coupled equations was to compare the percentage ionization of sodium as predicted by each method. The results in all cases were found to be consistent. As pointed out in the next section on experimental results, the measured electron density was found to be lower than that predicted from these computer calculations.

To resolve this inconsistency, it was decided to further check the chemistry involved in the system. One possibility that existed was that the magnesium oxide tube was reacting with the NaOH to disturb the equilibria. Inclusion of this compound in the computer program predicted almost zero interaction with the liquid NaOH or the superheated vapor. Figure 21 shows the consistency of the electron concentration even with the magnesium oxide comprising nearly 100 per cent of the two compounds. All other species were similarly unaffected.

Another possibility which was considered and may account for part of the discrepancy is the presence of excess water vapor. A similar computer run was made with this condition existing. Figure 22 shows a definite decrease in electron concentration. It is interesting to note that on a percentage basis most of this decrease takes place at high pressures and that most of the reduction occurs with the first 20 per cent excess weight fraction of H_2O. Experimentally, it is felt that the bakeout to 250°C before closing the magnesia tube would have removed any excess water present. There is, however, a possible 5 per cent water of hydration bound up in the crystal that may be released at high temperatures. This would seem to contribute only a factor of three at most on the basis of the computer calculations. Upon still further investigation it appeared that reasonable errors in the measured thermodynamic quantities (e.g., heat of formation of NaOH vapor) that go into the calculation of the equilibrium constant could account for a factor of as much as 5 in electron concentration which would readily account for the variance of results with JANAF predictions.

Experimental Measurements and Results

Electron density and collision frequency measurements were initially attempted with sodium hydroxide at vapor temperatures of approximately 1200°K and vapor pressures in the 1 to 10 torr range. The choice of these conditions was based on the corresponding JANAF predictions of approximately 10^6 electrons/cc, which was well within the range of the sensitivity of the microwave system. Under these conditions, no cyclotron absorption was observed. This result indicated that the electron density within the magnesia container was less than 10^5 electrons/cc, which was the lower limit of the sensitivity of the microwave system. However, as the temperature was raised to approximately 1300°K, absorption curves were recorded with amplitudes well above the noise level. A typical curve is shown in Fig. 23. This result indicates a very abrupt increase of electron density with temperature in this range. Further measurements were made at higher temperatures in order to determine the electron number density dependence on temperature. All these observations possessed half widths which indicated that the spectra were truly pressure broadened. The results of these measurements are presented in tabular form in Fig. 24 as a function of the two experimental variables, vapor pressure and temperature. The electron density was determined from the measurement of the area under the fractional absorption curve using Eq. 16. It is seen to be a strong function of vapor temperature. The densities shown in Fig. 24 are approximately 5 to 10 times lower than what would be predicted from the JANAF data presented in Fig. 15, except for two spurious points obtained at 1162 and 1164°K, which were inconsistent with several previous measurements made at 1200°K. The dc effective collision frequency was determined from the fractional power absorbed at peak resonance together with the electron density using Eq. 10. The last column in Fig. 24, "$\Omega_{1/2}$" refers to the shift in frequency off resonance where the power absorbed has dropped to one half of its peak value. For the case where the collision frequency is independent of velocity, "$\Omega_{1/2}$" can be shown to be equal to the effective collision frequency. For the contrasting case where ν is a function of velocity, "$\Omega_{1/2}$" represents an intermediate value between the true ac effective collision frequency and the dc effective collision frequency. As shown in Fig. 24, "$\Omega_{1/2}$" is approximately two to three times larger than $\nu_{eff\ (dc)}$*. This is evidence that there may be a fairly strong velocity dependence of the collision frequency. An approximation of the effective cross section inferred from the dc effective collision frequency data in Fig. 24 yields a value of about 5 to 20 $cm^{-1}\ mm^{-1}$ for the ranges of these investigations. This value is considerably less than what would be expected on the basis of the available cross-section information on the sodium hydroxide vapor constituents.

Although it would have been somewhat more desirable to extract the true ac effective collision frequency from data taken farther into the wings of the absorption curve, the value based on the "$\Omega_{1/2}$" is probably correct to within a factor of 2.

In conclusion, since spectrochemical analysis on the residue of sodium hydroxide in the magnesia tube showed no reaction between the container and the liquid sodium hydroxide, it is strongly felt that the superheated vapor showing the cyclotron resonance absorption is the true thermodynamic mixture of pure sodium hydroxide vapor.

Consequently, the cyclotron resonant measurement of the electron density is felt to be a true indication that the JANAF prediction of the electron densities is high by approximately an order of magnitude.

Summary

Using microwave cyclotron resonance techniques, the electron density and dc effective collision frequency have been measured in sodium hydroxide vapor under conditions of thermodynamic equilibrium for vapor temperatures ranging from 1000° to 1466°K and for vapor pressures in the 1.0 to 10.0 torr range as determined from the JANAF NaOH vapor pressure data. Results of this investigation indicate that the equilibrium electron concentration is significantly lower than is predicted by the JANAF thermochemical data. In addition, the dc effective collision frequency, as determined from the power absorption at cyclotron resonance, results in an effective collision cross section considerably lower than would be indicated by the available cross-section information pertaining to the NaOH vapor constituents, which also lends support to the possibility that the JANAF data may be in error in this range of pressures and temperatures.

ION-MOLECULE TOTAL COLLISION CROSS-SECTION MEASUREMENTS

Introduction

The processes governing the degree of ionization and rate of decay of re-entry wake plasmas are, in part, dependent upon the elastic interactions between ions and molecules. Furthermore, it is expected that the important ion-molecule interactions will involve ions having very low ionization potentials, since plasma temperatures in the far wake have been estimated to be less than 1 eV. One low ionization potential material which may be present in the form of an impurity in the re-entry wake is sodium, since it occurs naturally in the upper atmosphere and is also a heat shield ablation product. Therefore, it is desirable to know the characteristics of the interactions of low-energy sodium ions with various atmospheric constituents. A modified Ramsauer experiment, similar in design to one which has been previously employed to investigate cesium ion-atom interactions over the energy range from 0.12 to 9.7 eV,[9] has been used to determine the total collision probability of sodium ions interacting with nitrogen, nitric oxide, and oxygen over the energy range from 1.08 eV to 10.35 eV. The corresponding collision probabilities for these measurements ranged from 65 cm^{-1} mm^{-1} at an energy of 10.35 eV to 310 cm^{-1} mm^{-1} at an energy of 1.08 eV with an energy dependence which indicates that no chemical reactions are occurring between the various species under investigation. Further studies are required to extend the energy range to 0.1 eV.

Outline of Experimental Technique

The modified Ramsauer experiment, which was used to measure low-energy, ion-molecule collision cross sections, is comprised of a contact ion source, electroformed collision chamber, and a low-current ion detector. The various components are arranged as shown schematically in Fig. 25. A uniform magnetic field, which was used to energy-select the ions produced by the contact ion source, was oriented perpendicularly to the plane of the schematic. The unique geometry of the collision chamber served to define three points of constraint, which were the entrance aperture, the necked-down portion in the center of the chamber, and the exit aperture. These three points of constraint served to define uniquely the radius of a circle. Therefore, the energy of any ion which exited the collision chamber could be determined by knowing the radius of curvature and the magnitude of the applied magnetic field. At ion beam energies below several electron volts, small electric fields on the order of millivolts per centimeter can significantly perturb the trajectory of an ion in the magnetic field. Therefore, 60-degree total included angle re-entrant end surfaces were employed on the collision chamber to prevent the penetration into the chamber of the external electric fields produced in other portions of the system. Metal

interfaces, which could give rise to possible contact potentials within the chamber, were eliminated by electroforming the collision chamber. In an effort to increase the current available for cross-section measurements at low energies, a series of focusing and extracting electrodes were placed directly in front of the ionizer cap. These focusing electrodes served to extract ions from the ionizer cap and to produce a well-collimated ion beam.

The collision cross-section measurement consists of determining the magnitude of the ion current that emerges from the collision chamber as a function of the target gas pressure within the collision chamber. The probability of collision, P_T, is then obtained from the relation

$$i(p) = i(0)e^{-pxP_T} \tag{31}$$

where

p - absolute pressure at 273°K
x - interaction path length
i(0) - unattenuated ion current

The total collision cross section Q_T is defined at a reduced pressure of 1 mm and is related to P_T by

$$Q_T = \frac{760}{N_o} P_T \text{ cm}^2 \tag{32}$$

where

N_o - Loschmidt's number = 2.6871×10^{19} cm^{-3}

By repeating these measurements at successive levels of magnetic field strength, P_T is obtained as a function of ion energy.

Description of Experimental Components

Vacuum System

In making a total collision cross-section measurement, it was generally necessary to vary the target gas pressure in the collision chamber from 10^{-6} to 10^{-3} mm in order to obtain sufficient attenuation of the ion beam. Furthermore, to insure against the possibility of the ion beam making a significant number of additional collisions in transit between the collision chamber and the ion detector, which would give rise to an erroneously high cross section, it was important that the collision chamber pressure exceed the ambient pressure in the vacuum system by at least two orders of magnitude. Therefore, in these measurements a vacuum system with an ambient background pressure of at least 10^{-8} mm

was essential to prevent secondary scattering events. To meet these requirements, an all stainless steel, ultrahigh vacuum system was designed and fabricated. The resulting system is shown installed with the magnetic field coils in position in Fig. 26.

The main vacuum chamber consisted of a cylindrical tank 33 in. in diameter and 15 in. deep with a demountable cover. The interior of the tank was divided into two compartments by an ion dense baffle. The ion gun was located in one compartment, and the ion detection system, which was an electron multiplier, was located in the adjacent compartment. The collision chamber protruded through a close-fitting alumina plate mounted on the baffle and, therefore, provided the only possible path for ions to get from the gun to the detector.

Each tank compartment was individually pumped through a port located on the bottom of the main tank by a vacuum system consisting of an 1800 liter per second oil diffusion pump, a water-cooled oil baffle, a zeolite baffle, and a liquid nitrogen cold trap. This combination provided each chamber with an effective pumping speed conservatively rated at 200 liters per second for noncondensable gases, such as nitrogen, nitric oxide, and oxygen, and 3000 liters per second for condensable gases, such as sodium. In addition to vacuum pumping ports, each tank compartment had several access ports for providing feed throughs for thermocouples, coolants, and the various electrode power leads.

Although the vacuum system was capable of being baked at 670°K, it was not found necessary to do this as the system base pressure after one or two days of operation was typically 10^{-8} mm on the electron multiplier side and 10^{-5} mm on the ion gun side. The lower pressure in the gun chamber was due to the breaking down of residual hydrocarbons by the alkali vapor and to the pumping or gas gettering characteristics of the tantalum electrodes.

Sodium Ion Source

Sodium ions were produced by surface contact ionization of sodium atoms which diffuse through a heated, porous tungsten button. Maximum ion beam current levels were achieved by using an accel-decel system to extract ions from the porous tungsten cap surface. Proper alignment of the ion beam with the collision chamber was achieved with a series of deflection plates located along the path of the beam.

The net energy of the ion beam was approximately controlled by referring the accel-decel electrode power supplies to the ionizer and then biasing the ionizer with respect to the collision chamber. The sodium surface coverage of the ionizer, though constant for a constant set of operating conditions, was not precisely predictable. Consequently, the effective work function of the ionizer cap was not known. Furthermore, at the energy levels of interest (0.1 eV to 10.0 eV) the change in the effective work function of the ionizer cap was found

in many conditions to be considerably larger than the ionizer cap bias.[9] Therefore, the true energy of the ion beam could only be obtained from a knowledge of radius of curvature defined by the geometry of the collision chamber and the magnitude of the applied magnetic field.

Collision Chamber

The determination of the ion beam energy, which was based on the assumption of constant curvature of the ion beam trajectory in the magnetic field, could be seriously in error if any stray electric fields were present within the collision chamber. At energies of a few tenths of an electron volt, fields as low as millivolts per centimeter would produce significant deflections of the ion beam trajectory in the magnetic field. Therefore, the collision chamber had to be designed to exclude from its interior any fields arising from neighboring high-potential structures and to minimize internal thermoelectric fields arising from metal interfaces. To this end, the collision chamber was patterned after a type previously used to measure the total collision cross section of low-energy cesium ion-cesium atom interactions.[9] For example, re-entrant type apertures, as shown in Fig. 25, with a total included angle of 60 degrees were used for the entrance and exit apertures of the collision chamber. Analog field plots have shown that this particular geometry attenuates external electric fields typical of those existing in the system to essentially zero at the plane of the aperture. In addition, the collision chamber shown in Fig. 25 was electroformed so that there were no metal interfaces which could give rise to contact potential effects within the chamber. Actual construction of the collision chamber was accomplished by fabricating a high-purity aluminum mandrel to the chamber shape and then electroplating the desired chamber material over the mandrel to a thickness of approximately 0.060 in. The mandrel was then removed from the electroformed chamber by using a caustic solution which etched the aluminum but did not react with the electroplated material. Electroformed chambers produced by this process have been found to be leak tight and completely free from residual surface impurities. By controlling the rate of deposition of the plating material and the surface finish of the aluminum mandrel, the metallic grain size of the inner surface of the chamber was maintained on the micron scale. When the inner surface of the collision chamber used in these measurements was inspected under a microscope, it was found that instead of a grainy structure, the initial plating layer on the inner surface was actually amorphous with no indication of grain boundaries. Electric fields produced by inhomogeneities in surface grain structure would be, to the first approximation, expected to penetrate into the collision chamber over dimensions which are comparable to the average metallic grain size. Therefore, since the characteristic aperture dimensions of the chamber were on the order of 0.05 in. and the metallic grain size was maintained on the micron scale, electric fields produced by surface inhomogeneities could not significantly penetrate into the chamber. With the absence of even micron size grain boundaries on the inner chamber surfaces, possible electric field perturbations were reduced even further.

The shape of the collision chamber was similar to that shown schematically in Fig. 25. Dimensionally the chamber consisted of a 1.5-in. square duct with a passage radius of 10.0 in. and a circumferential length of 10.5 in. from entrance to exit aperture. The diameters of the entrance and exit apertures were 0.050 in. and 0.150 in., respectively, and the width of the center constraint was 0.100 in. The resulting minimum scattering angle of the collision chamber was 0.41 degrees. Target gas was introduced into the chamber on both sides of the center constraint. The chamber was fabricated of pure gold which was selected on the basis of being the only practical electroforming material that will not acquire surface oxides at the operating temperatures of the system. The elimination of the possible formation of oxides on the inner surfaces of the collision chamber was extremely critical, since the presence of oxides can give rise to electric fields within the chamber which can influence the ion beam trajectory.

Target Gas Metering System

The maximum operating pressure in the collision chamber was established primarily by two factors. First, the pressure in the main vacuum tank had to be limited to less than 10^{-6} mm in order to prevent high-voltage arcing in the electron multiplier. Second, a pressure ratio of at least two orders of magnitude was needed between the collision chamber and the vacuum chamber in order to minimize ion-particle collisions between the exit aperture of the collision chamber and the multiplier. Consequently, the maximum operating pressure in the collision chamber had to be maintained below approximately 10^{-3} mm.

Direct-pressure measuring techniques are extremely inaccurate at typical collision chamber operating pressures which are 10^{-6} to 10^{-3} mm. McLeod gauges, for example, are subject to significant pressure errors arising from the streaming of mercury vapor from the gauge to the cold trap.[10] Consequently, the target gas pressure in the collision chamber could not be measured directly but was determined by regulating the mass flow of the target gas that escaped from the collision chamber exit and entrance apertures. Since the mean-free path of any one of the target gases (N_2, NO, O_2) was at least twice that of the largest dimension of the collision chamber at pressures of 10^{-3} mm, the flow was well established in the free-molecular regime. Under this condition the collision chamber end apertures formed choked orifices whose conductance depended only on gas temperature, molecular weight, and aperture area. Since these quantities were directly measurable with adequate precision, the uncertainty in the measurement of collision chamber gas pressure depended primarily on the accuracy to which the incoming target gas flow rate was known.

The target gas metering system that was used to provide the collision chamber with accurately known, preselected levels of target gas flow was patterned after a type used to measure noncondensable expellant mass flows in ion

engine efficiency tests.[11] A functional diagram of the system with its associated calibration system is shown in Fig. 27. The philosophy of the gas flow metering system was based on the fact that the conductance of the fixed leak depends only upon the applied pressure. In the system shown schematically in Fig. 27, the pure gas regulator was used to control the applied pressure to the calibrated leak. To insure that conductance was not affected by other factors, the leak was kept in a constant temperature environment and was protected from dust particles with submicron particle filters. Therefore, by employing a pressure gauge that was repeatable within the desired level of certainty, the mass flow rate was precisely known.

The conductance of the fixed leak was calibrated as a function of the applied pressure. This was done by setting the pure gas regulator at different pressure levels and measuring the rate of rise of pressure in a calibrated volume. The measured rate of rise was directly proportional to the conductance of the fixed leak at any applied pressure level. The rate of rise was obtained by measuring the time required for the pressure in the calibrated volume to change from 0 to 10 mm with constant pressure applied to the leak. When the calibrated volume pressure reached 10 mm, a capacitance manometer, which was connected between the calibrated volume and a 10-mm reference plenum, indicated a null. The pressure in the reference plenum was checked with a liquid nitrogen-trapped McLeod gauge, which is extremely accurate as an absolute pressure gauge in the 1 to 10 mm pressure range.

The mass flow system that was used to control the collision chamber pressure is shown in its constant temperature enclosure in Fig. 28. A calibration curve for nitrogen gas pressure at 298°K within the collision chamber as a function of the leak pressure (read on the gauge visible in Fig. 28) is shown in Fig. 29. Calibration curves for nitric oxide and oxygen were almost identical to the one for nitrogen. Repeatability of the calibration data taken on different days and after pressure cycling the leak was found to be within 0.2 per cent. However, this level of repeatability lost its significance due to the combinations of random and systematic errors that occurred in the calibration process. These errors were calculated to amount to ± 0.35 per cent probable and ± 0.62 per cent maximum.

Since the pressure in the collision chamber was determined by dividing the mass flow of the target gas by the total free-molecular conductance of the end apertures, it was necessary to accurately determine the dimensions of each aperture. To this end, the chamber apertures and a precision scale were each photographed with a precision microscope set at about 30 power. The total cross-sectional aperture area was obtained by using a planimeter which was calibrated by the use of the precision scale. The finite "tube" length of the aperture was obtained from a picture taken at an angle of 60 degrees from the plane of the aperture. The total free-molecular conductance was then obtained from the thin orifice equation with the Clausing correction for finite length included.[12] With

the geometrical characteristics of the apertures known the only additional corrections on collision chamber pressure were for temperature and molecular weight of the gas.

Ion Detection System

The basic measurement in the total collision cross-section experiment is the accurate determination of the ratio of i(p) to i(0). This measurement was made by observing the ion current level emerging from the collision chamber either as time-averaged current or as a discrete number of events per unit time. The choice depended upon the available current level of the ion beam.

The detection system that was used in this experiment was patterned after one which was successfully used in measuring cesium ion-cesium atom cross sections at energies as low as 0.12 eV.[9] Ions emerging from the exit aperture of the collision chamber were accelerated by an electric field into the first dynode of a 20-stage electron multiplier having an ultrastable current gain of approximately 10^6. The output of the multiplier was measured by an electrometer input picoammeter at current levels greater than 10^{-15} amperes. At very low ion beam current levels, the output of the electron multiplier was an irregular series of current pulses which corresponded to the arrival of ions at the first dynode. In this case the output of the multiplier was used to trigger a tunnel-diode pulse generator. The output of the pulse generator was registered on a 1-mc frequency counter whose gate time could be varied from 0.01 sec. to 1000 sec. Thus at very low values of ion beam current, the data was taken as a discrete number of events per unit time.

Experimental Results

The separate interactions of a sodium ion beam with nitrogen, nitric oxide, and oxygen gas were investigated using a modified Ramsauer experiment. Total probabilities of collision were measured over an ion energy range of 1.08 eV to 10.35 eV for scattering events which produced beam deflections greater than 0.41 degrees. A minimum detectable scattering angle of 0.41 degrees was chosen in these experiments to insure that the cross-section information obtained could be analyzed on a completely classical basis. The collision chamber, which was designed to provide a field free region through which the beam could pass without suffering any changes in energy, also served to uniquely define the beam energy. However, due to the required finite size of the entrance and exit apertures and the width of the center constraint of the collision chamber, the ion beam was not monoenergetic. Geometrically, the maximum energy window of the collision chamber was $\pm$10 per cent of the center energy. An energy distribution which was typical of those obtained in the course of the measurements is shown in Fig. 30. For energies above one electron volt, all the energy distributions

were essentially defined by the geometrical constraints of the collision chamber, which is to be theoretically expected.

Cross-section information was taken by observing the attenuation of the ion beam current as a function of the target gas pressure in the collision chamber. An example of a typical attenuation measurement obtained with nitrogen as the scattering gas is shown in Fig. 31. The probability of collision is proportional to the slope of the resulting curve in semi-logarithmic coordinates and can be determined from Eq. 31. In determining the cross section, the leak pressure, hence the collision chamber target gas pressure, was increased until the ion beam current had decreased to at least 25 per cent of its unattenuated value. At this point the flow of target gas to the collision chamber was interrupted and the collision chamber pressure subsequently returned to the equilibrium base pressure of the vacuum system within about 20 seconds. If the ion gun was functioning properly and no drifting in ion beam current level was present, the ion beam would return to its original unattenuated level. If, after obtaining a pressure attenuation, the ion beam current level did not return to its original value for conditions of base pressure in the collision chamber, it was assumed that beam conditions changed during the course of the measurement and, subsequently, the run was invalidated. Invariably, failure to achieve initial conditions could be attributed to drifting of the ion beam current level due to an improper adjustment of the ion gun optics.

The resulting total collision probability data are presented for sodium ions interacting with nitrogen, nitric oxide, and oxygen in Figs. 32, 33, and 34, respectively. The collision probability for sodium ions interacting with nitrogen (Fig. 32) increased monotonically with decreasing ion energy in a manner consistent with elastic scattering interactions. The collision probability data for the other two gases behaved in a similar manner down to energies of about three electron volts. None of the gases yielded collision probabilities higher than would be expected from an elastic scattering interaction. Therefore, chemical reactions, which would tend to increase the collision probabilities above the elastic scattering curve, can be ruled out in the one to ten electron volt energy range.

Below the three electron volt level the measured cross-section data for nitric oxide and oxygen fell below the classically predicted elastic scattering behavior for reasons that are not yet fully understood. The attenuation data in this region continued to produce straight lines in semi-logarithmic coordinates, and the ion beam current always returned to initial conditions after removal of the target gas. Inasmuch as the attenuations were linear, there apparently was an increase in the ion beam current that was proportional to the target gas pressure in the collision chamber. Since the target gas leaks from the collision chamber entrance aperture into the gun region in proportion to the collision chamber pressure, there is a good probability that both the nitric oxide and the oxygen changed the focusing characteristics of the system by altering contact

potentials on the various electrode surfaces. There is an additionally good possibility that the presence of oxygen increased the work function of the tungsten contact ionizer, producing increased emission which would tend to partially offset the effects of the pressure attentuation. There were potentials in the gun region that were more than adequate to dissociate nitric oxide. The effect of increased emission due to changes in the ionizer work function would be most pronounced at the low ion beam current levels associated with the lower energies. The solution to either of these possible effects will be to purposely leak oxygen into the gun region at a rate that exceeds the maximum leak rate from the collision chamber by an appreciable amount. This additional amount of gas will not significantly increase the pressure in the gun region, due to the high pumping speed of the vacuum system, but will be sufficient to overshadow any contribution to electrode work function changes due to the target gas.

A comparison of the data for sodium ions interacting with each of the three gases on the higher end of the energy range shows the collision probabilities to be very nearly the same. This is to be expected, since the potential functions for the elastic interactions scale directly as the polarizability of the target gas. In this case the polarizabilities of nitrogen, nitric oxide, and oxygen are essentially the same, varying only $\pm$ 5 per cent from their average value. In view of the unexpected nature of the low energy end of the collision probability curves for nitric oxide and oxygen, this data should be considered preliminary and further experimental effort will be required before any interpretation can be affixed to the low energy drop off in the cross section.

Efforts to measure cross sections at energies of less than one electron volt have not been successful due to a low energy cutoff of the ion beam current. There are no theoretical reasons that would limit sodium ion beams to the one electron volt cutoff. In fact, in a recently conducted symmetrical on-atom cross-section experiment, a cesium ion beam was used that was intelligible down to less than 0.05 electron volts. Therefore, it is believed that a sodium ion beam at 0.1 electron volts is attainable by making certain improvements in the components. Several such improvements have already been made. For example, the addition of vertical deflect plates in front of the collision chamber to correct for elevation misalignment of the beam has helped to lower the energy cutoff of the system. Further lowering of the energy cutoff was obtained by shortening the isothermal support block on the multiplier end of the collision chamber until the chamber protruded from the block. The purpose of the change was to eliminate the off-trajectory deflection of the ion beam by contact potentials appearing at the end of the support block. Additional improvements are planned, particularly in the sodium ion beam gun where special emphasis will be placed on the alignment with respect to the collision chamber. With further investigations it is anticipated that all three collision probability curves can be extended down to 0.1 electron volts.

Atmospheric Gas Ion Source

A new type of atmospheric ion source was investigated during the latter part of the contract period. The source, which is shown schematically in Fig. 35, is an application of the hollow cathode discharge that is presently being used to provide monoenergetic electron beams for high-power welding. Ions are produced in the electron beam, which is formed at the aperture of the hollow cathode, and are accelerated back toward the cathode due to the gradient in the electron beam. Use is made of these ions which are at essentially anode potential by allowing them to pass out the back of the cathode and down a drift tube to the vacuum system. As a hollow cathode discharge requires pressures on the order of 10^{-2} to 10^{-1} mm in order to operate, gas is introduced into the discharge region directly. The only way for it to escape is through the exit hole in the cathode. Thus a very high pressure ratio can be realized between the discharge region and the vacuum system where the experiment is to be performed.

A hollow cathode discharge ion source was built and operated in conjunction with a small 40 liter per second vacuum system. Nitrogen gas was admitted directly into the glass envelope containing the hollow cathode discharge. The diameter of the exit hole in the rear of the hollow cathode was 0.12 in. Ions passed through the exit hole and into a 0.38-in. diameter, 10-in. long drift tube. After exiting the drift tube into the vacuum system, the ions were collected by a target that was connected to a microammeter. The cathode and drift tube in these measurements were maintained at ground potential.

Pressures in the discharge tube were typically 2×10^{-2} to 8×10^{-2} mm, and pressures in the vacuum system were between 10^{-5} and 10^{-4} mm. Under these conditions the voltage drop across the discharge, which was constant for constant pressure, was approximately 400 volts. Current through the discharge could be readily controlled by varying the output of the power supply. Ion currents measured at the target were approximately proportional to the discharge current and were found to range as high as 10^{-5} amperes. The high current levels and relative simplicity of design make this type of ion source extremely attractive for cross-section measurements. The only factor which remains to be investigated is the possible production of ionized excited states which could alter significantly the characteristics of a collisional interaction.

Summary

An all stainless steel ultrahigh vacuum system was designed and constructed for use in a modified Ramsauer total collision cross-section experiment. The total probability of collision was determined from 1.08 eV to 10.35 eV for sodium ions interacting with three atmospheric constituents, nitrogen, nitric oxide, and oxygen. The probabilities were found to vary from approximately 65 cm^{-1} mm^{-1} to 310 cm^{-1} mm^{-1} depending on the target gas and the ion energy.

On the basis of the energy dependence of the cross sections measured, it is concluded that there are no contributions to the total cross sections due to chemical interactions. Several atmospheric gas ion sources have been investigated, and one particularly simple source was constructed and tested which has produced ion beam current levels sufficient for cross-section measurements.

ELECTRON ATTACHMENT INVESTIGATIONS

Introduction

The alkali metal compounds that result from the presence of alkali metal impurities in re-entry wakes can significantly change the effective radar cross section of the wake by the formation of negative ions. Electron attachment investigations were undertaken to study the formation of negative ions in sodium hydroxide, which is one of the possible alkali metal compounds that can be present in re-entry wakes.

A crossed-beam double modulation technique was used for this investigation in which an electron beam is interacted with a molecular beam of sodium hydroxide to study negative ion production by electron impact. A monopole mass spectrometer was constructed to mass analyze the species of charged particles produced by the interactions of the two beams. Over the electron energy range from 0.05 eV to 10 eV, negative currents that could be directly attributable to the interaction of the crossed electron and sodium hydroxide beams have been detected. The maximum cross section for the interaction was found to be $3 \times 10^{-16} cm^2$ for an electron energy slightly less than 2 eV. Further investigations are required to definitely determine the species produced in the interaction.

Outline of Experimental Technique

A crossed-beam apparatus, which had been previously used to measure electron interactions with potassium chloride, was used in the present investigations to study the formation of negative ions by electron impact in sodium hydroxide vapor. In this experiment a beam of electrons intersects a neutral beam of sodium hydroxide molecules at right angles within a collision chamber, which has been designed to prevent penetration into the interaction region of perturbing external electric fields. A double oven configuration was used to generate and superheat a molecular beam of sodium hydroxide. The cross section for the interactions of the molecular beam with the electron beam was determined by measuring the negative current produced by the interaction.

Electron Beam

Shown in Fig. 36 is a schematic diagram of the crossed-beam apparatus. Electrons emitted from a planar Philips Type B electron emitter are constrained to move along the axis of the collision chamber by the applied magnetic field and are collimated into a well-defined beam by a set of focusing and retarding potential apertures located directly in front of the emitter surface. The

collimating and focusing apertures of the electron beam optics system were gold plated to reduce contact potential effects and to minimize any possible changes in applied potentials in the course of the measurements produced by absorption of sodium hydroxide on these surfaces. The electron beam passes through the collision chamber and intersects the neutral sodium hydroxide beam at right angles. Those electrons which do not interact with the neutral sodium hydroxide beam exit the collision chamber and are collected by a positive-biased electron collection electrode. By applying a retarding potential, V_1, between the electron emitter and the modulating aperture, only electrons emitted with energies greater than eV_1 overcome the potential barrier and enter the collision chamber. On reducing this retarding potential by an amount ΔV, an increased number of electrons, those with energies between eV_1 and $e(V_1 - \Delta V)$, have sufficient energy to overcome the retarding potential barrier. The difference between the number of negative particles collected on the ion collector with and without the incremental retarding potential, ΔV, applied is due to the interaction between the molecular beam and the electrons with initial energies between eV_1 and $e(V_1 - \Delta V)$. By employing phase-sensitive detection techniques, only the difference signal is recorded. Thus the negative current observed results from the interaction of the sodium hydroxide beam with a group of electrons whose spread in energy is only $e\Delta V$. An accelerating voltage, V, is used to control the energy of this group of electrons permitting the interaction cross section to be examined as a function of electron energy. By this retarding potential difference technique, which was first reported by Fox and Hickam[13], an electron beam of known energy, eV, with a narrow, effective energy distribution, ΔV is created. In these crossed-beam investigations, the retarding potential difference technique was successfully applied to produce effective electron energy distributions with half-widths of 0.20 eV. Use of a narrower distribution was not warranted because the energy dependence of the cross section was not found to vary extremely rapidly with energy.

Molecular Beam

A molecular beam of sodium hydroxide was produced by heating sodium hydroxide pellets in a platinum-lined nickel oven. The reservoir portion of the oven which contained the sodium hydroxide was mounted in a semivertical position to eliminate creep problems usually associated with molten sodium hydroxide. Some degree of superheating of the beam was achieved by maintaining the front compartment of the oven at an elevated temperature in comparison to the reservoir. This superheating of the front end of the oven source also served to prevent condensation of the beam at the source exit hole. Bifilar-wound heaters were employed to heat the source oven to prevent possible perturbations of the electron beam caused by small magnetic fields produced by the heater current. The nickel oven source in these measurements was operated above the Curie point to prevent magnetic field perturbations. Only nickel and platinum were found to be suitable materials to use in this high-temperature sodium hydroxide environment.

The molecular beam source oven was located in the first of three vacuum chambers, which were differentially pumped in order to achieve the highest vacuum possible in the collision chamber region. A series of small orifices were located along the sodium hydroxide beam trajectory for the purpose of collimation. In the second differentially pumped vacuum chamber, the molecular beam was chopped mechanically at 100 cps prior to passing into the interaction region in the collision chamber which was located in the third vacuum chamber. The neutral beam density of the sodium hydroxide beam was determined by measuring the positive ion current that was produced at a hot wire surface ionization gauge located directly beyond the molecular beam exit port of the collision chamber.

Collision Chamber

Shown in Fig. 37 is a photograph of the collision chamber. The chamber employed in these measurements had an inside diameter of 1/4 in. and a total length of 1 3/4 in. The electron entrance and exit holes were 1/8 in. and 9/64 in. in diameter, respectively, and the molecular beam entrance and exit holes were both 1/8 in.-square holes. The chamber, which was heated to prevent the condensation of molecules on to the inner surface of the chamber, was constructed from a single piece of oxygen-free, high-conductivity copper in order to minimize internal contact potentials and to decrease any thermal gradients which might be produced by the heating. A platinum-rhodium thermocouple was embedded in the side of the chamber for monitoring the temperature.

Detection System

The electron beam was modulated at 1040 cps and retarding potential techniques as outlined previously were employed to obtain the effect of a narrow electron distribution. The mechanical wheel, which was used to modulate the molecular beam at 100 cps, was constructed with two additional series of holes located along the periphery of the wheel that were used to generate 940 and 1040 signals. By this technique all three detection signals, critical to the measurements, were phased locked. The purpose for using double beam modulation was to employ phase-sensitive detection techniques to detect at the sideband frequency of 940 cps the signal produced by the interaction of the electron beam with the sodium hydroxide beam. A schematic of the electronics employed in the measurements is shown in Fig. 38. Detection at the difference frequency of 940 cps discriminates against the following interactions: (1) The interference of the scattered electrons and negative ions at the harmonics of 100 cps, which are produced by the dc component of the electron beam interacting with the 100 cps molecular beam; (2) the interference of the negative ions at the harmonics of 1040 cps, which are produced by the electron beam interacting with the unmodulated background gas; (3) the interference of the harmonics at 100 cps, caused by charged particles produced in the molecular beam source, which is modulated at 100 cps; and (4) the possible interactions of either beam with the walls of the chamber or the background gas existing in the system.

Detection at the difference frequency of 940 cps insures that only the interactions between the two beams will produce a phaseable signal. Collection of positive ions is discriminated against by the detector because the ion collecting electrodes, which were located astride the molecular beam exit port of the collision chamber, were biased positive with respect to ground potential. A transverse electric field was applied between the plates of the ion collector. Pure electron scattering events at 940 cps produced by the interaction of the 1040 electron beam with the 100 cps molecular beam were not discriminated against by the phase-sensitive detector system. However, the magnetic field, which was applied along the axis of the collision chamber, was adjusted so that the electron Larmor radius was small in comparison to the radius of the inside of the collision chamber while the lightest negative ion Larmor radius anticipated in the interactions was large enough to allow the particles to exit the chamber. By this technique electron scattering interactions could be discriminated from interactions which produce negative ions if perturbing electric fields do not penetrate into the collision chamber.

Mass Analysis

A monopole spectrometer was constructed for the purpose of mass analyzing the various species of ions formed in the electron sodium hydroxide beam interaction investigations. The mass spectrometer operates with an rf electric field applied between a two-electrode configuration for analyzing ions of different e/m ratios. Since the interaction region or collision chamber was run at ground potential, the spectrometer had to be operated in an unconventional mode; that is, the whole monopole structure was raised to some accelerating potential. The spectrometer was designed to have a mass resolution in excess of 100. A minimum mass resolution of 40 was required to distinguish between the negative ions NaO^- and $NaOH^-$. The ion detector, a 19-stage venetian blind type electron multiplier with a gain of about 10^6, was located at the exit slit of the monopole.

Initial calibration of the spectrometer was made with a CsCl impregnated zeolite, which yield a source of positive cesium ions.[14] Figure 39 is a typical recorder trace of the mass spectrum emitted by the Cs^+ source. Note that the mass scale in this figure is nonlinear. The resolution calculated with the Cs^+ peak was approximately 42. The insert of the figure is a semilogarithmic plot of the relative intensities of the alkali positive ion peaks detected with the monopole.

Tests on the stability of the electronics and the actual geometric tolerances of the monopole spectrometer indicate that the resolution should be in excess of 100, well within the resolution of 40 required for the negative ion experiment. To verify this resolution, a KCl beam was surface ionized and the positive ion spectrum determined. The spectrometer easily resolved the isotop of potassium, thus yielding a resolution of at least 40.

A duplicate sodium hydroxide source to the one being used in the negative ion investigations was constructed and installed in a separate vacuum system with the spectrometer to analyze the effusing neutral beam. The first tests were made by surface ionizing the neutral sodium hydroxide beam on a hot tungsten filament. With the rear of the oven at 250°C and the front at 340°C, Na^+ and $NaOH^+$ were the predominant ions detected. Figure 40 is a recorder trace of the spectrum obtained. Note that the ratio $I_{Na^+}/I_{NaOH^+} = 2.2$. The source was heated to rear and front temperatures of 340° and 440°C, respectively. The resulting ratios for this conditon were $I_{Na^+}/I_{NaOH^+} = 27$ and $I_{NaOH^+}/I_{Na_2OH^+} = 100$. After keeping the source temperatures constant for one hour, another spectrum was taken with the results $I_{Na^+}/I_{NaOH^+} = 2500$ and $I_{NaOH^+}/I_{Na_2OH^+} = 400$. Approximately the same results were obtained using a crossed-beam apparatus similar in design to the negative ion investigation system. These large observed changes in the molecular species of the effusing vapors indicate a possible thermodynamically non-equilibrium condition. Although the reason for this non-equilibrium is not understood at the present time, it may explain the very large nonreproducibility reported in the literature concerning the temperature dependence of the molecular species of sodium hydroxide vapors.[15]

Experimental Results

A double modulated crossed-beam apparatus has been used to investigate the interactions of electrons with sodium hydroxide over an energy range from 10 eV to near thermal energies. Detectable 940 cps negative currents which could be directly attributable to the interactions of the two beams were obtained over the entire energy range. Shown in Fig. 41 is a plot of the negative ion current to the collector detected at 940 cps and the electron current distribution as a function of the electron accelerating potential.

The observed negative current arriving at the ion collector i, as a function of the electron accelerating energy w is given by

$$i(w) = KNL \int_0^\infty \sigma(E) \left[i_e(u) \right]' du$$

where L is the length of the molecular beam intercepted by the electron beam, N is the molecular beam density, $\sigma(E)$ is the effective cross section for the observed reaction which is a function of the absolute electron energy E, and $\left[i_e(u) \right]' du$ is the electron current in the energy range u to u + du. The constant K takes into consideration the divergence of the molecular beam between the point of interaction with the electron beam to the surface ionization gauge where the molecular beam is monitored, the efficiency with which the individual species in the molecular beam are surface ionized (the efficiency of ionization of sodium hydroxide was assumed to be equal to that reported for sodium[15]), and a factor which takes into account that the ions are observed at the sideband frequency of 940 cps.

When the electron distribution is narrow compared to the change in the negative current over the same energy interval, as in Fig. 41, then the equation reduces to

$$i(w) = KNL\, i_e(u)\, \sigma(E)$$

where the observed current i is proportional to the cross section. When the appropriate substitutions are made in the above equation, the value of the cross section at the negative current peak was 3×10^{-16} cm^2.

A monopole spectrometer was employed to investigate both the negative and positive ion species formed from the interaction of the two beams. In initial spectrometer measurements positive ion species of Na^+, $NaOH^+$, and Na_2OH^+ were detected. Negative ions were not detected with this system.

In an effort to ascertain whether or not the negative current detected at 940 cps was produced by electron scattering interactions with the 100 cps modulated sodium hydroxide beam, electron interactions with helium beams were investigated in the same experimental apparatus. In this case it would not be expected that negative current signals would be detected because of the low helium attachment cross section. Shown in Fig. 42 is the detected 940 cps phaseable negative current signal obtained from these investigations. The detected 940 cps signal was found to be phaseable over several orders of magnitude change in neutral beam density. The negative current curve shown in Fig. 42 can be directly related to a cross section since the electron current distribution in these measurements was 0.2 eV wide at half height and the negative current curve was not a rapidly varying function of energy. The relative shape of this cross-section curve is in fair agreement with the reported total electron helium scattering cross section.[17] The fact that the detected 940 cps signal in these measurements did not change phase with changes in neutral beam pressure serves to indicate that multiple scattering of electrons along the beam is not producing the detectable signal. As pointed out earlier, the experiment was designed so that the magnitude of the applied magnetic field along the axis of the collision chamber would confine electrons which interacted with the beam within the collision chamber. On the basis of the helium results, there appears to be a good possibility that electron scattering interactions in both measurements are contributing to the detectable 940 cps negative current signal. It is also interesting to note that the magnitude of the cross section determined from these investigations is the same order of magnitude as that reported in the first part of this report for electron sodium hydroxide collision cross sections for momentum transfer. Subsequent to these measurements, the sensitivity of the monopole spectrometer was improved by a factor of 10^2, and negative ion species were successfully detected in background vapors. Further measurements must be obtained, however, before these ions can be definitively attributed to negative ions formed by electron impact on sodium hydroxide.

Therefore, on the basis of these results, it should be concluded that the cross section reported for the interaction of electrons with sodium hydroxide should be considered as the maximum upper limit for possible negative ion formation. It should also be recognized that on the basis of the helium results, a large portion of the detected 940 cps signal could be attributed to electron scattering interactions. These results could also imply that external potentials are penetrating into the collision chamber, and therefore, the uncertainty in the electron energy at lower energies for the data reported in Figs. 41 and 42 should be at least 0.5 eV.

Summary

Electron interactions with sodium hydroxide beams have been investigated over the energy range from thermal energies to 10 eV. The cross section for the interaction exhibited a maximum of 3×10^{-16} cm^2 at an energy near 2 eV. This cross section should be considered only as the maximum possible attachment cross section for this system until a definitive mass analysis is obtained of the species of particle produced by the interactions.

REFERENCES

1. R. M. Hill, Sylvania Technical Report MPL-13 (1958).

2. J. L. Hirshfield and S. C. Brown, Phys. Rev. 122, 719 (1961).

3. F. C. Fehsenfeld, J. Chem. Phys. 39, 1653 (1963).

4. R. K. Flavin and R. G. Meyerand, Jr., "Collision Cross Section of Low-Energy Electrons with Cesium Atoms," Proceedings of the IEEE Thermionic Conversion Specialist Conference held in Gatlinburg, Tennessee, October 7, 8, and 9, 1963.

5. W. P. Allis and S. J. Buchsbaum, Proceedings of the Third Biennial Gas Dynamics Symposium (Northwestern University Press, Evanston, Illinois, 1960), p. 3.

6. W. P. Allis, Handbuch der Physik XXI (Springer-Verlag, Berlin, 1956), p. 383.

7. S. Ramo and J. R. Whinnery, Fields and Waves in Modern Radio (J. Wiley & Sons, Inc., New York, 1960), Chap. 7.

8. M. A. Heald and C. B. Warton, Plasma Diagnostics with Microwaves (J. Wiley & Sons, Inc., New York, 1965), p. 71.

9. R. H. Bullis, "Low-Energy Cesium Ion-Atom Collision Cross Sections," published in the Proceedings of the IEEE Thermionic Conversion Specialist Conference held in Gatlinburg, Tennessee, October 7, 8, and 9, 1963.

10. H. Ishii, K. Nakayama, "A Serious Error Caused by Mercury Vapour Stream in the Measurement with a McLeod Gauge in the Cold Trap System," Vacuum Symposium Transactions 1, 1961.

11. E. A. Pinsley, A. P. Walch, C. M. Banas, J. W. Davis, and T. L. Churchill, "Applied Research on the Oscillating Electron-Ion Engine," UAC Research Laboratories Report B-910065-9 on Contract AF 33(616)-8376, ASD-TDR-63-253, April, 1963, Confidential.

12. S. Dushman and J. M. Laffery, "Scientific Foundations of Vacuum Technique," (J. Wiley & Sons, Inc., New York, 1962), pp. 93-94.

13. R. E. Fox, W. M. Hickam, D. J. Grove, and T. Kjeldaas, Jr., Rev. Sci. Instr. 26, 1101 (1955).

14. R. E. Weber and L. F. Cordes, "Aluminosilicate Alkali Ion Sources," to be published in the Proceedings of the Twenty-fifth Annual Conference on Physical Electronics, M.I.T., March 25, 26, and 27, 1965.

15. For example, V. S. Rao and R. C. Schoomaker, "Velocity Analysis of Molecular Beams Generated from NaOH Vapors," J. Chem. Phys. 33 (6) 1718 (1960).

16. S. Datz and E. H. Taylor, Jour. Chem. Phys. 25, (1956), "Ionization on Platinum and Tungsten Surfaces. I. The Alkali Metals".

17. L. S. Frost and A. V. Phelps, Phys. Rev. 136 (1964), "Momentum Transfer Cross Sections for Slow Electrons in He, Ar, Kr, and Xe from Transport Coefficients".

LIST OF FIGURES

Fig. 1 - Plasma Waveguide Geometry. Schematic of Cyclotron Absorption Line

Fig. 2 - Microwave Spectrometer

Fig. 3 - Microwave Bridge Attenuator

Fig. 4 - High-purity Magnesium Oxide Measurement Tube

Fig. 5 - Vacuum Oven for High-Temperature Cyclotron Resonance Experiments

Fig. 6 - NaOH and $(NaOH)_2$ Concentration in Superheated NaOH Vapor

Fig. 7 - Na Concentration in Superheated NaOH Vapor

Fig. 8 - H_2O Concentration in Superheated NaOH Vapor

Fig. 9 - O_2 Concentration in Superheated NaOH Vapor

Fig. 10 - NaO Concentration in Superheated NaOH Vapor

Fig. 11 - OH Concentration in Superheated NaOH Vapor

Fig. 12 - H_2 Concentration in Superheated NaOH Vapor

Fig. 13 - O Concentration in Superheated NaOH Vapor

Fig. 14 - H Concentration in Superheated NaOH Vapor

Fig. 15 - Electron and Na^+ Concentration in Superheated NaOH Vapor

Fig. 16 - Na_2 Concentration in Superheated NaOH Vapor

Fig. 17 - NaH Concentration in Superheated NaOH Vapor

Fig. 18 - OH^- Concentration in Superheated NaOH Vapor

Fig. 19 - O^- Concentration in Superheated NaOH Vapor

Fig. 20 - H^- Concentration in Superheated NaOH Vapor

Fig. 21 - Electron Concentration in NaOH Vapor with Excess MgO Present

Fig. 22 - Electron Concentration in NaOH Vapor with Excess H_2O Present

Fig. 23 - Typical Cyclotron Resonance Absorption Curve

Fig. 24 - Table of Results

Fig. 25 - Schematic of Ion Collision Cross-Section Apparatus

Fig. 26 - Ion-Molecule Cross-Section Experiment. Bakeable Ultrahigh Vacuum System

Fig. 27 - Target Gas Flow Metering and Calibration System

Fig. 28 - Target Gas Metering System

Fig. 29 - Collision Chamber Pressure Calibration for N_2 at 25°C

Fig. 30 - Normalized Ion Beam Energy Distribution

Fig. 31 - Typical Ion Beam Attenuation with Increasing Collision Chamber Pressure

Fig. 32 - Total Collision Probability for Sodium Ions Interacting with Nitrogen at 0°C

Fig. 33 - Total Collision Probability for Sodium Ions Interacting with Nitric Oxide at 0°C

Fig. 34 - Total Collision Probability for Sodium Ions Interacting with Oxygen at 0°C

Fig. 35 - Hollow Cathode Atmospheric Ion Source

Fig. 36 - Diagram of Apparatus

Fig. 37 - Copper Collision Chamber

Fig. 38 - Diagram of Electronics

Fig. 39 - Calibration Run

Fig. 40 - Surface Ionized Spectrum

Fig. 41 - Negative Current as a Function of Electron Accelerating Potential (Electron Sodium Hydroxide Interactions)

Fig. 42 - Electron Current as a Function of Electron Accelerating Potential (Electron Helium Interactions)

PLASMA WAVEGUIDE GEOMETRY

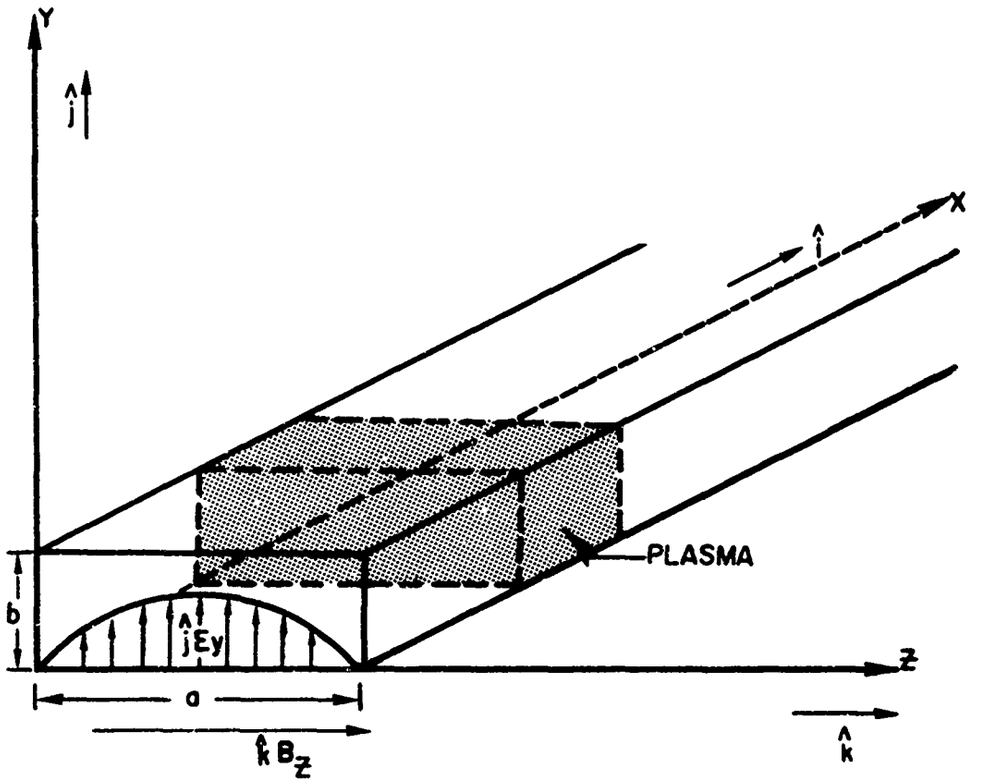

SCHEMATIC OF CYCLOTRON ABSORPTION LINE

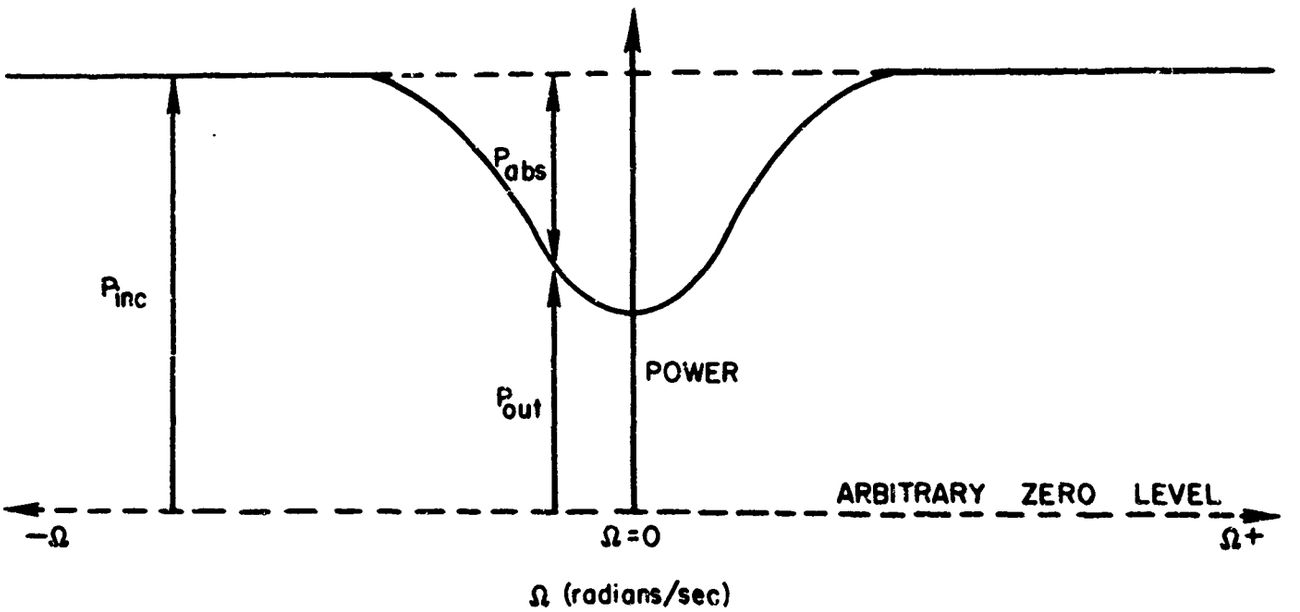

MICROWAVE SPECTROMETER

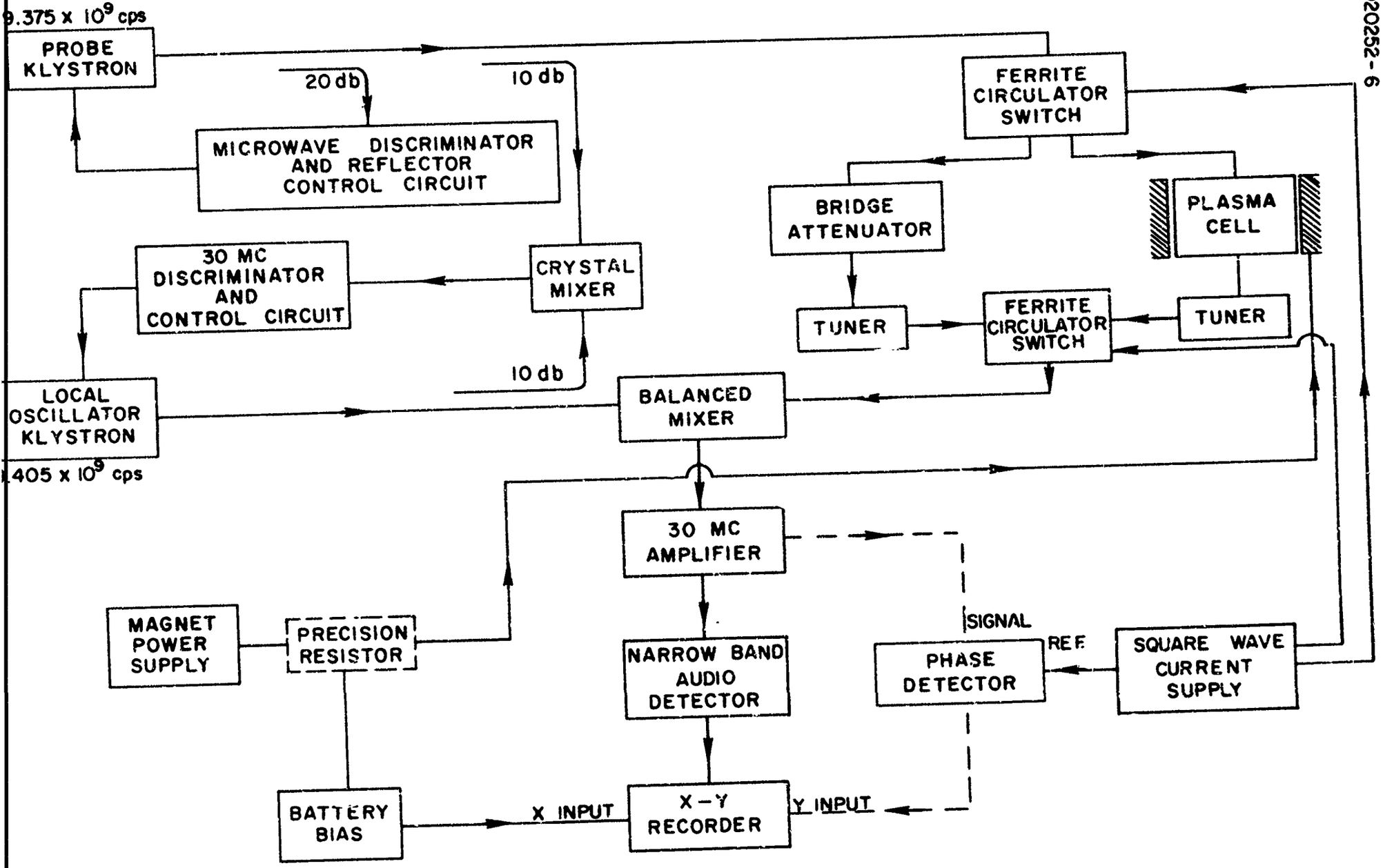

D-920252-6

FIG. 2

D-920252-6

FIG. 3

MICROWAVE BRIDGE ATTENUATOR

D-920252-6

FIG. 4

HIGH PURITY MAGNESIUM OXIDE MEASUREMENT TUBE

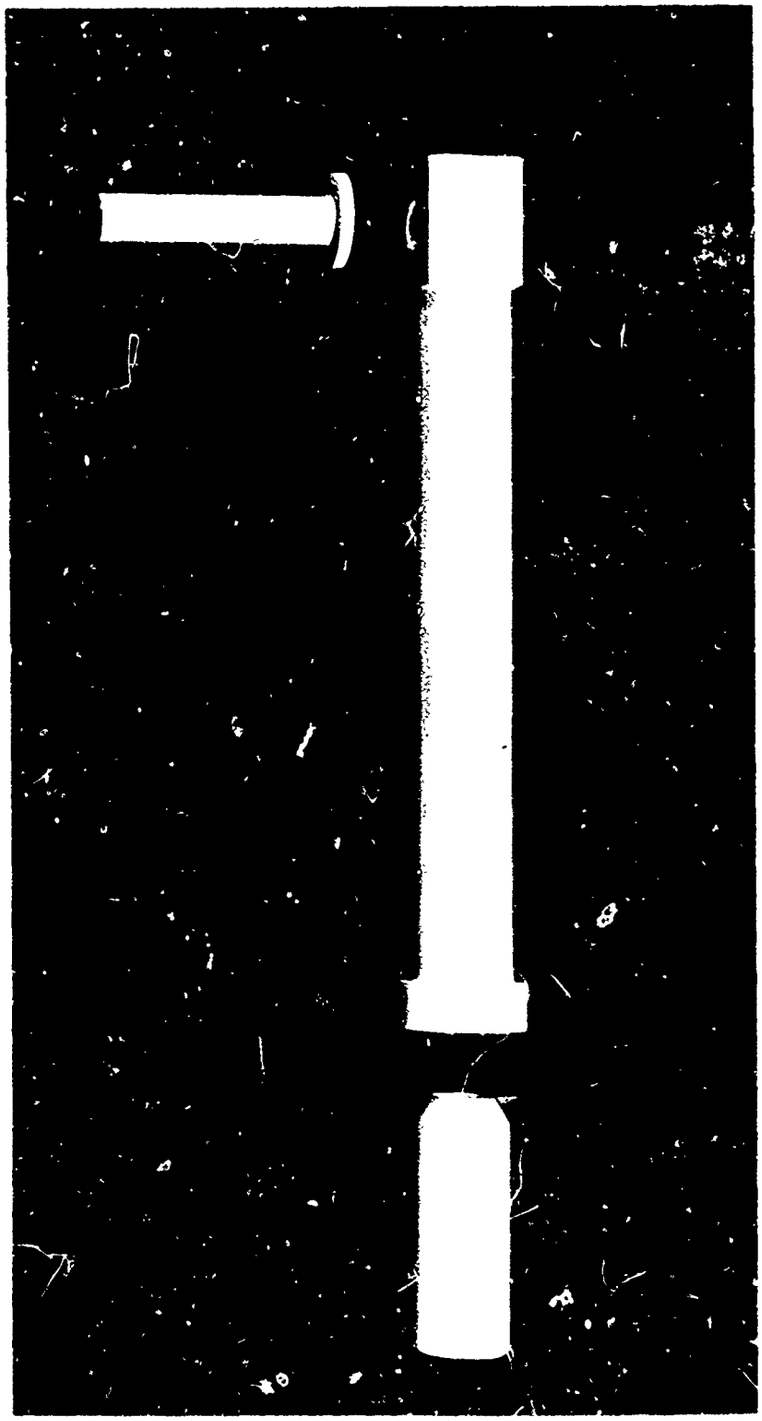

FIG. 5

VACUUM OVEN FOR HIGH TEMPERATURE CYCLOTRON RESONANCE EXPERIMENTS

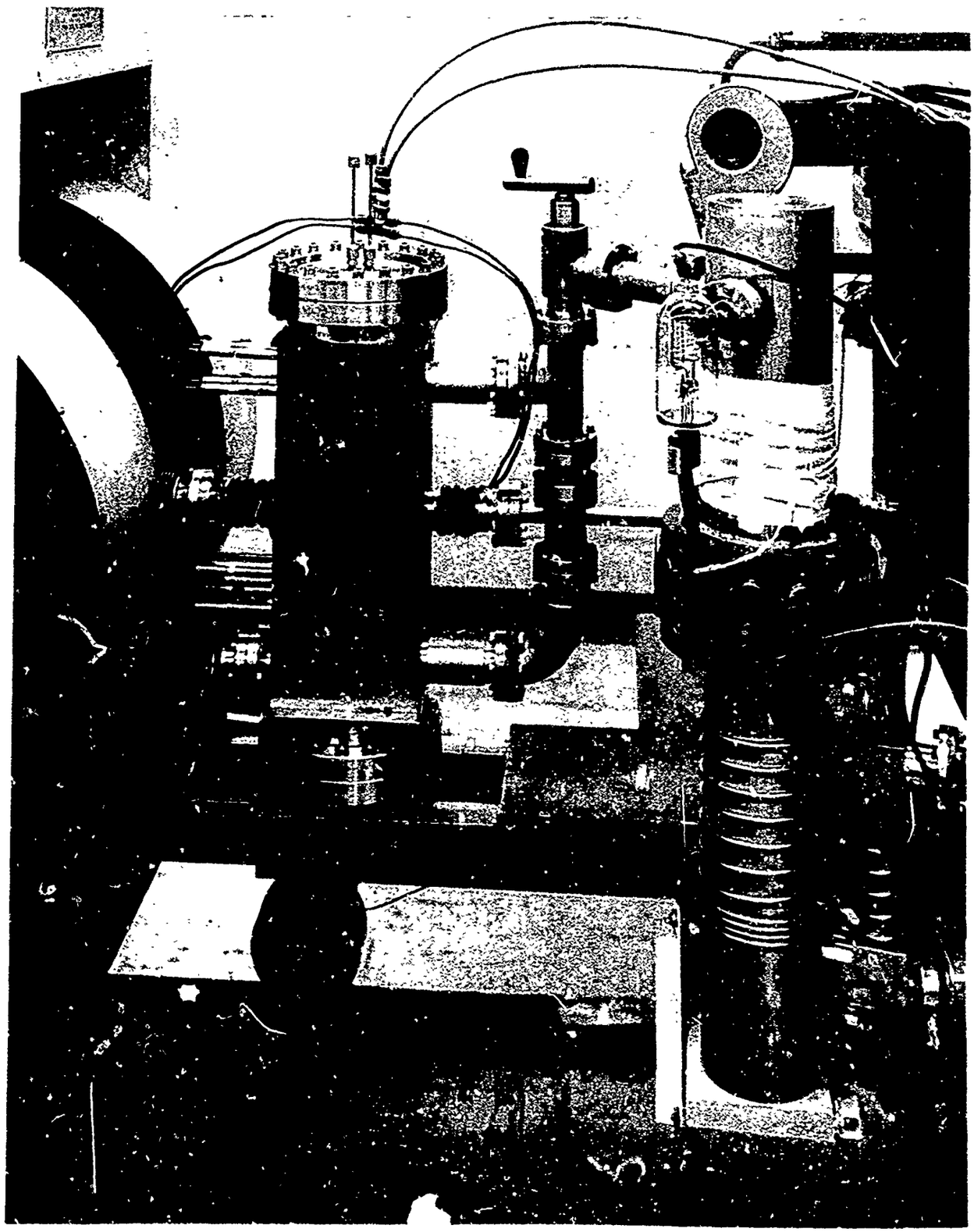

FIG. 6

NaOH AND $(NaOH)_2$ CONCENTRATION IN SUPERHEATED NaOH VAPOR

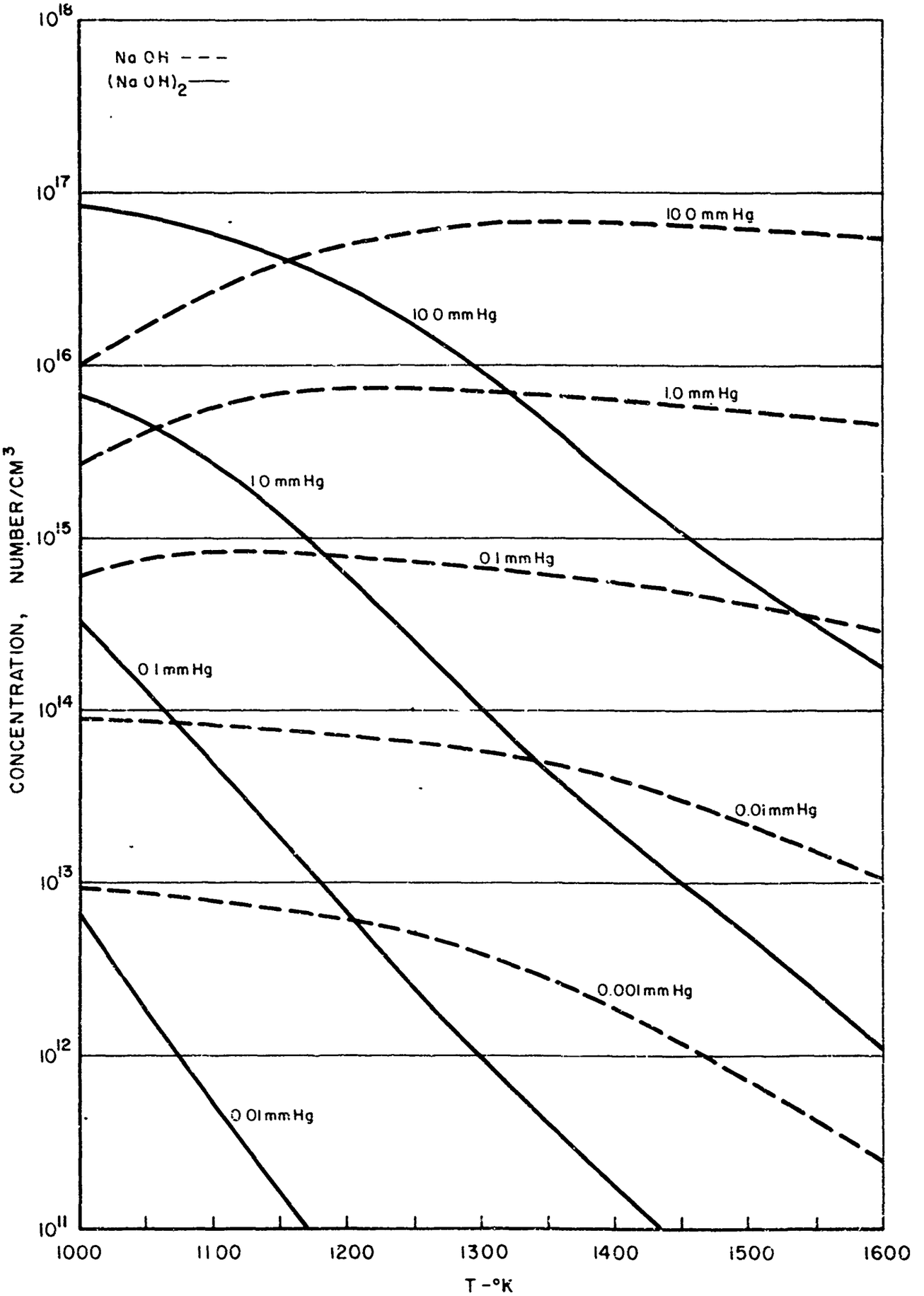

FIG. 7

Na CONCENTRATION IN SUPERHEATED NaOH VAPOR

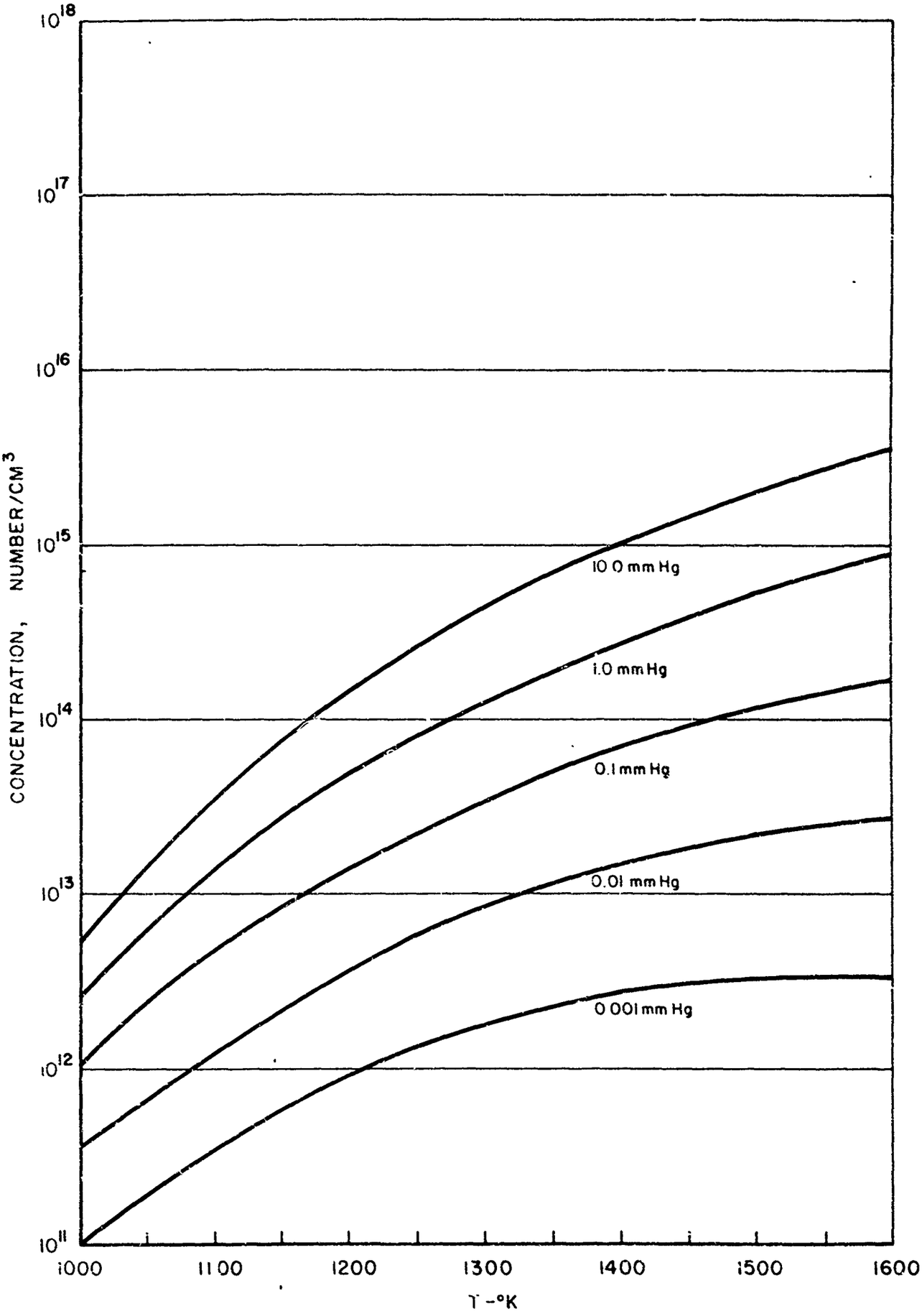

FIG. 8

H_2O CONCENTRATION IN SUPERHEATED NaOH VAPOR

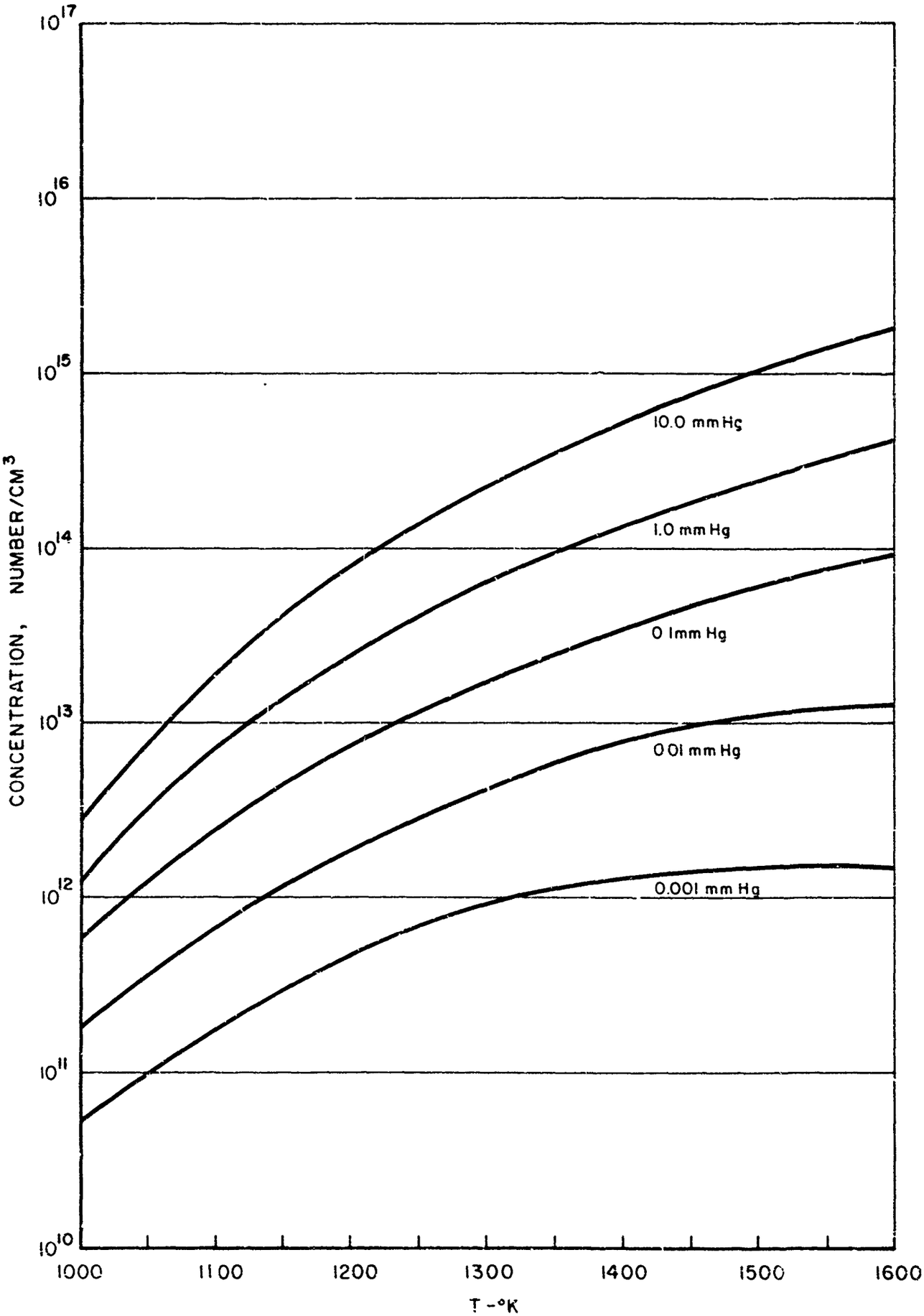

FIG. 9

O_2 CONCENTRATION IN SUPERHEATED NaOH VAPOR

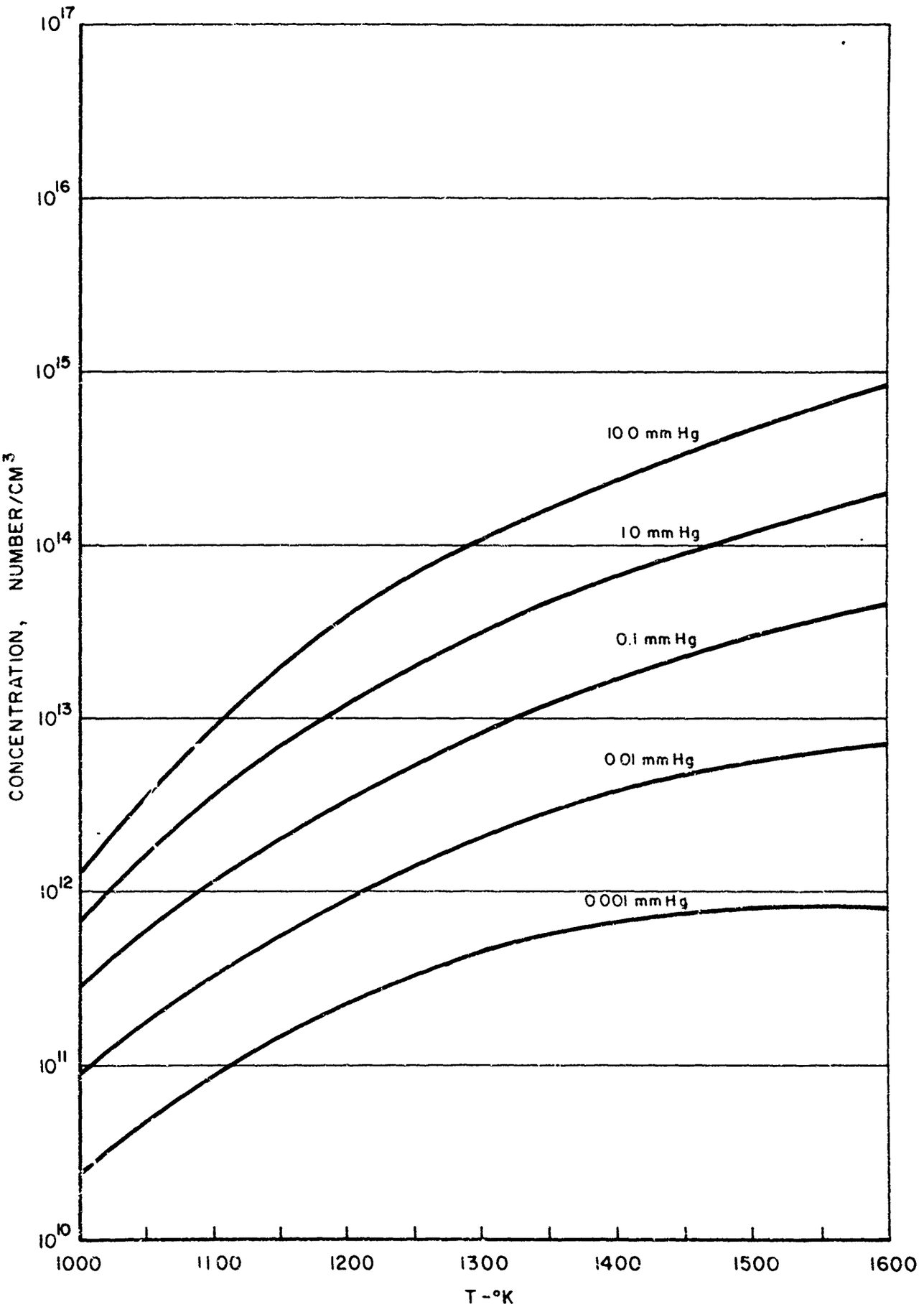

D-920252-6

FIG. 10

NaO CONCENTRATION IN SUPERHEATED NaOH VAPOR

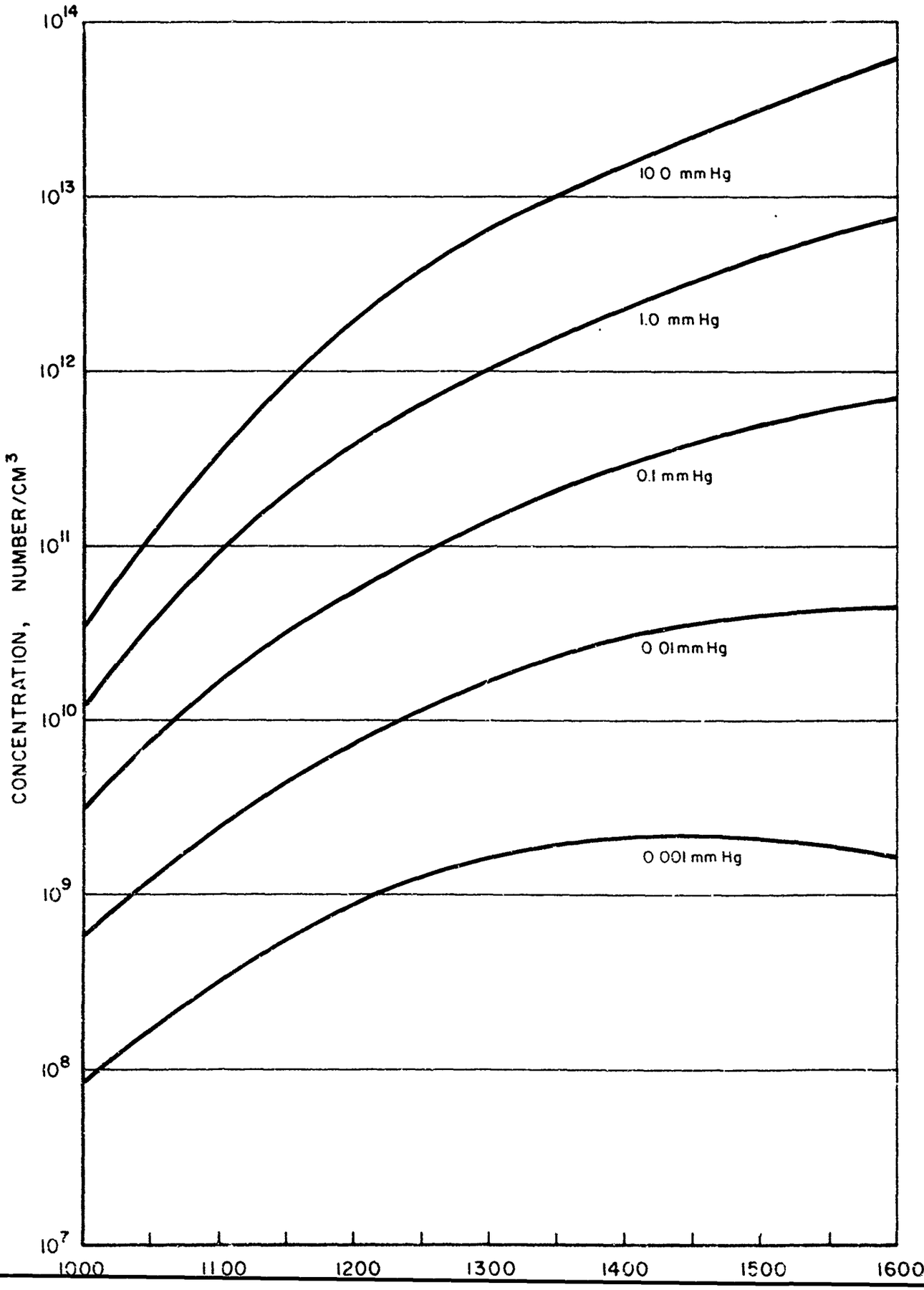

D-920252-6

FIG. 11

OH CONCENTRATION IN SUPERHEATED NaOH VAPOR

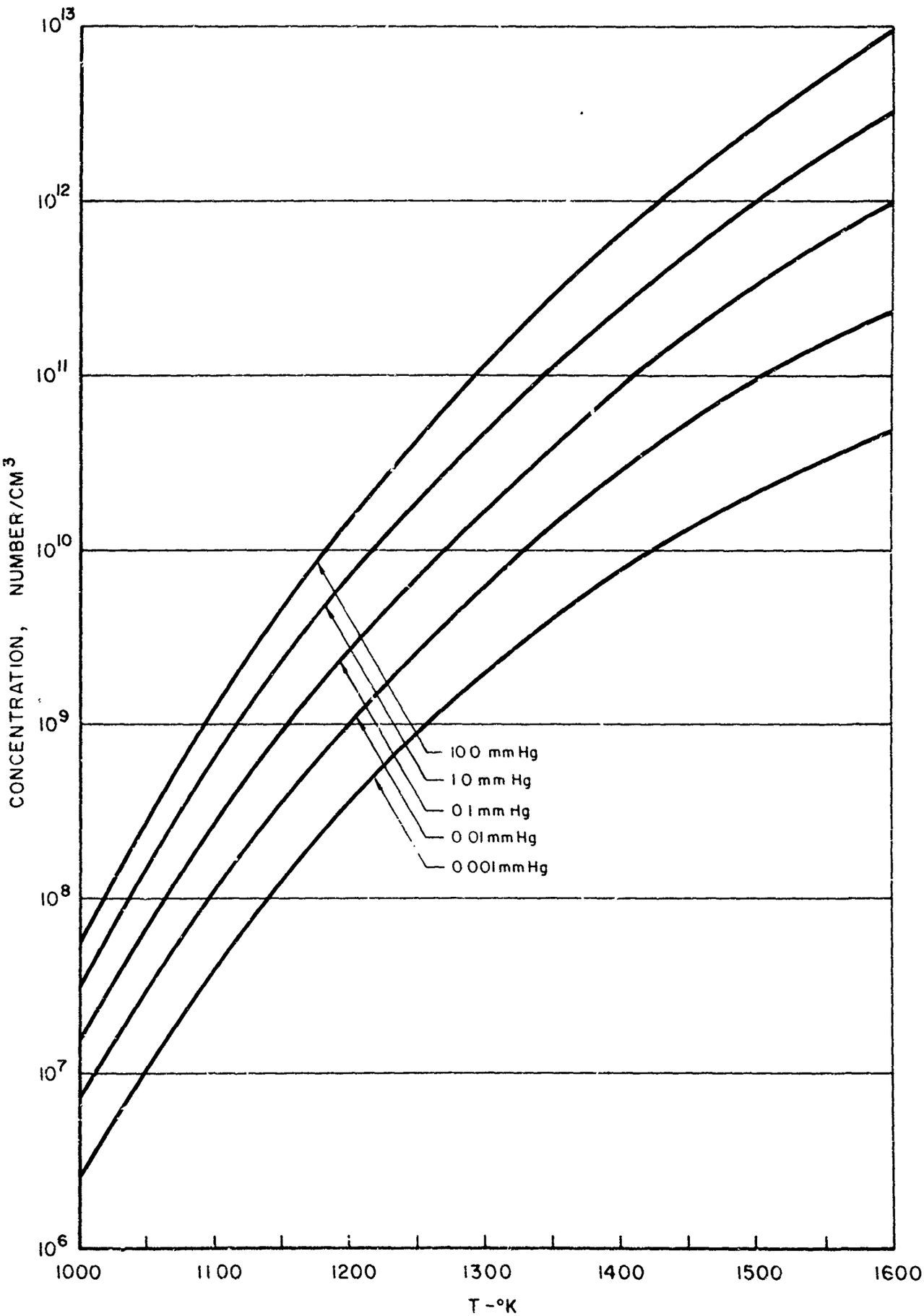

FIG. 12

H_2 CONCENTRATION IN SUPERHEATED NaOH VAPOR

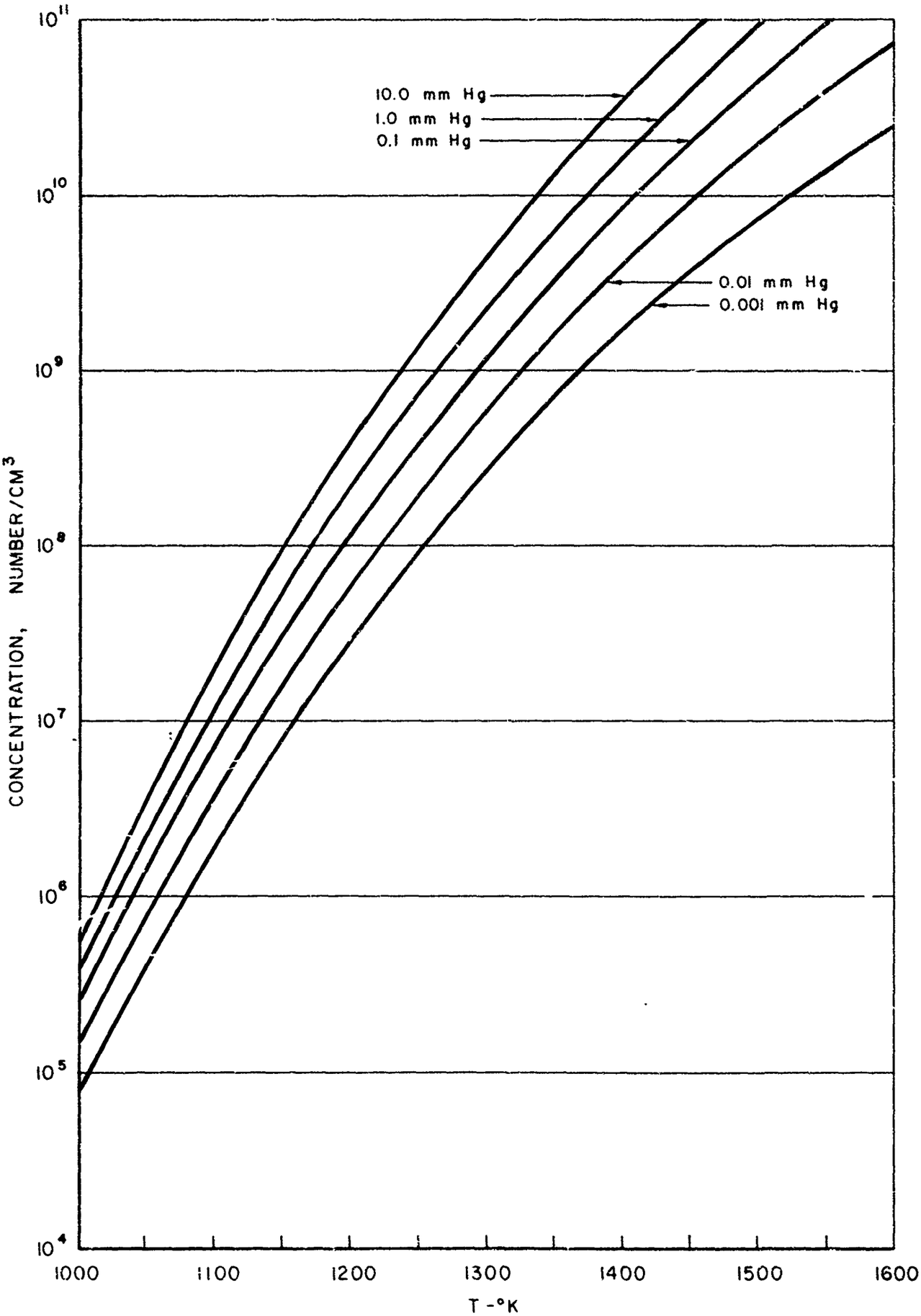

FIG. 13

O CONCENTRATION IN SUPERHEATED NaOH VAPOR

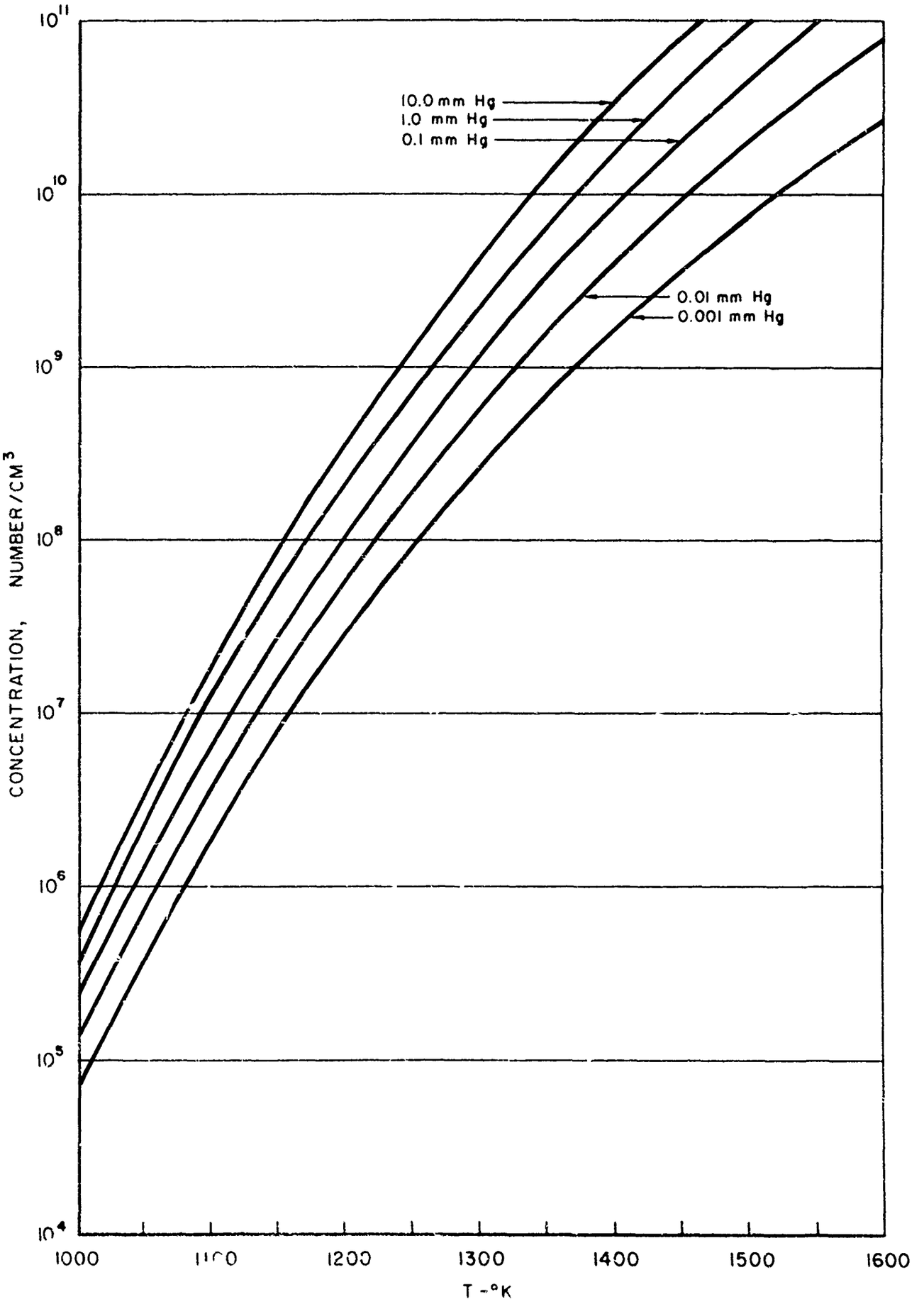

FIG. 14

H CONCENTRATION IN SUPERHEATED NaOH VAPOR

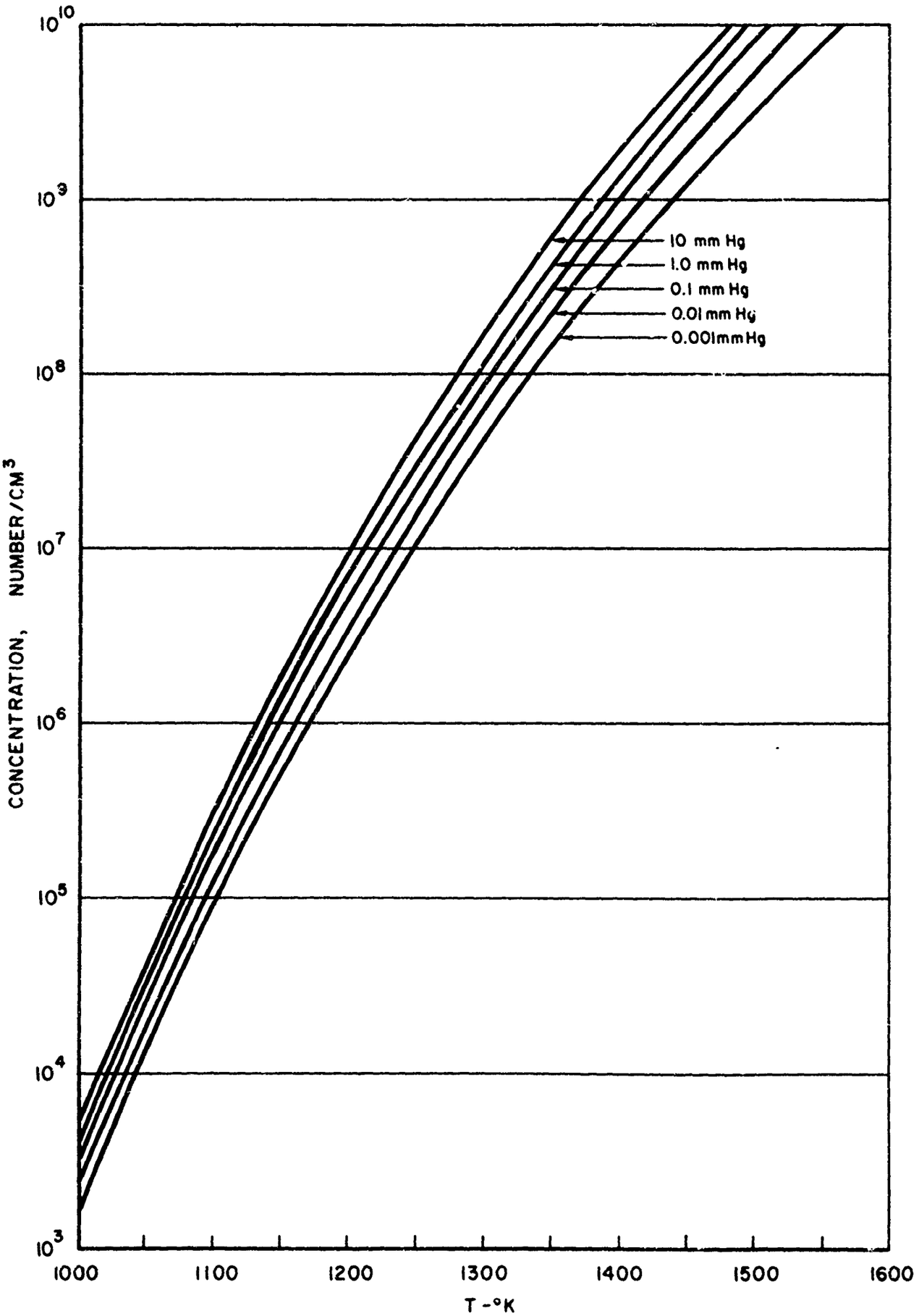

FIG. 15

ELECTRON AND Na^+ CONCENTRATION IN SUPERHEATED NaOH VAPOR

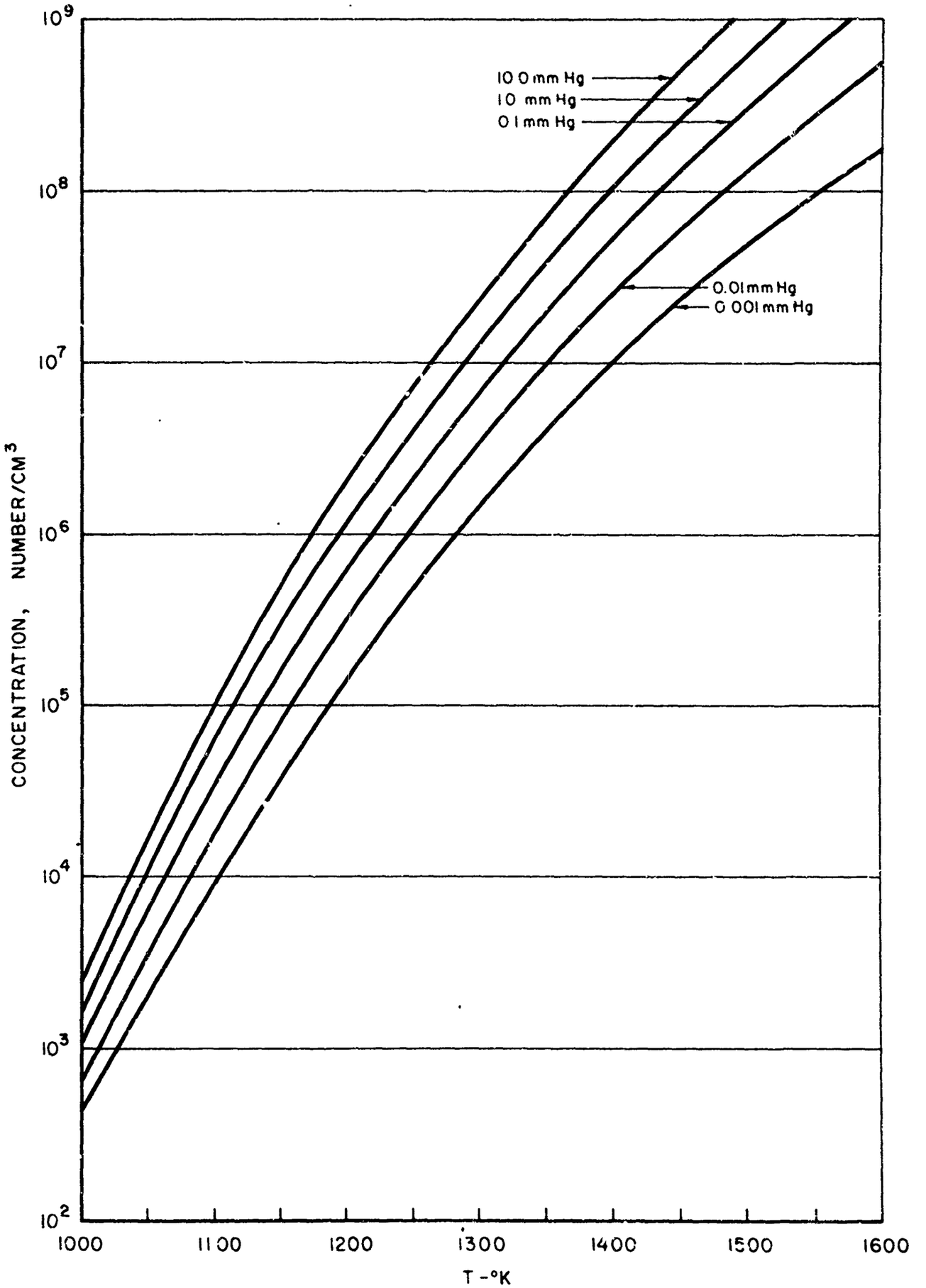

FIG. 16

Na_2 CONCENTRATION IN SUPERHEATED NaOH VAPOR

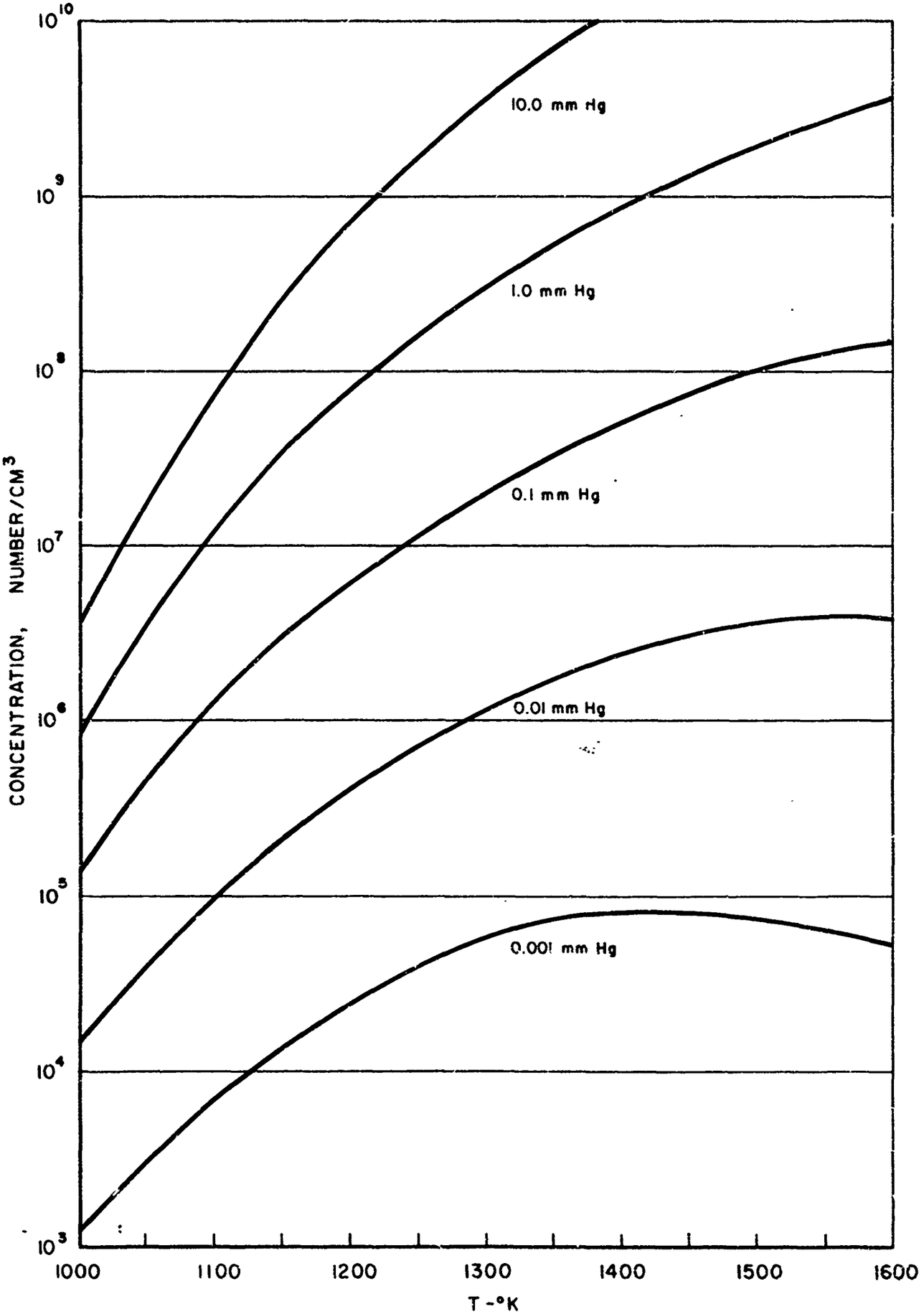

FIG.17

NaH CONCENTRATION IN SUPERHEATED NaOH VAPOR

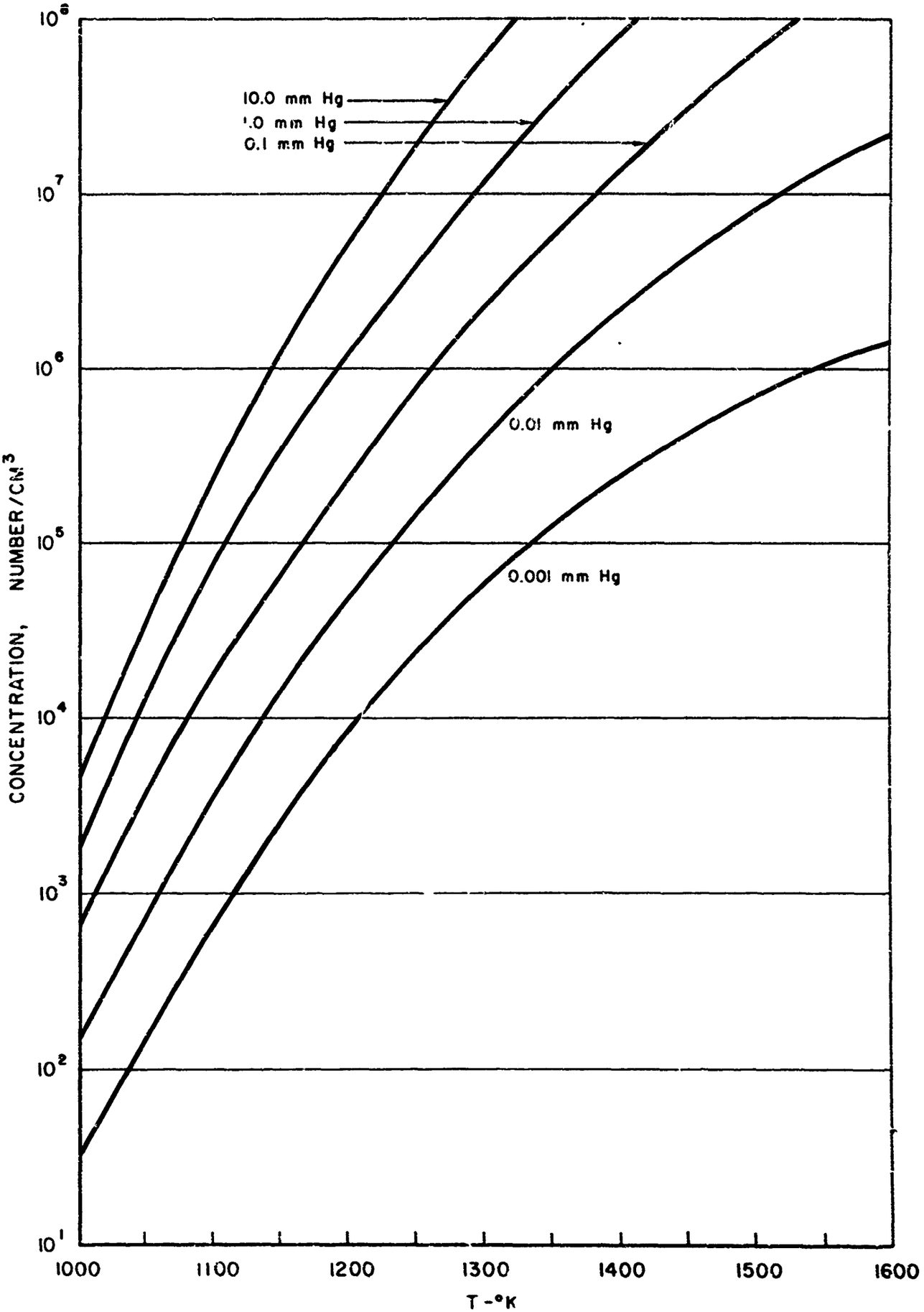

FIG. 18

OH^- CONCENTRATION IN SUPERHEATED NaOH VAPOR

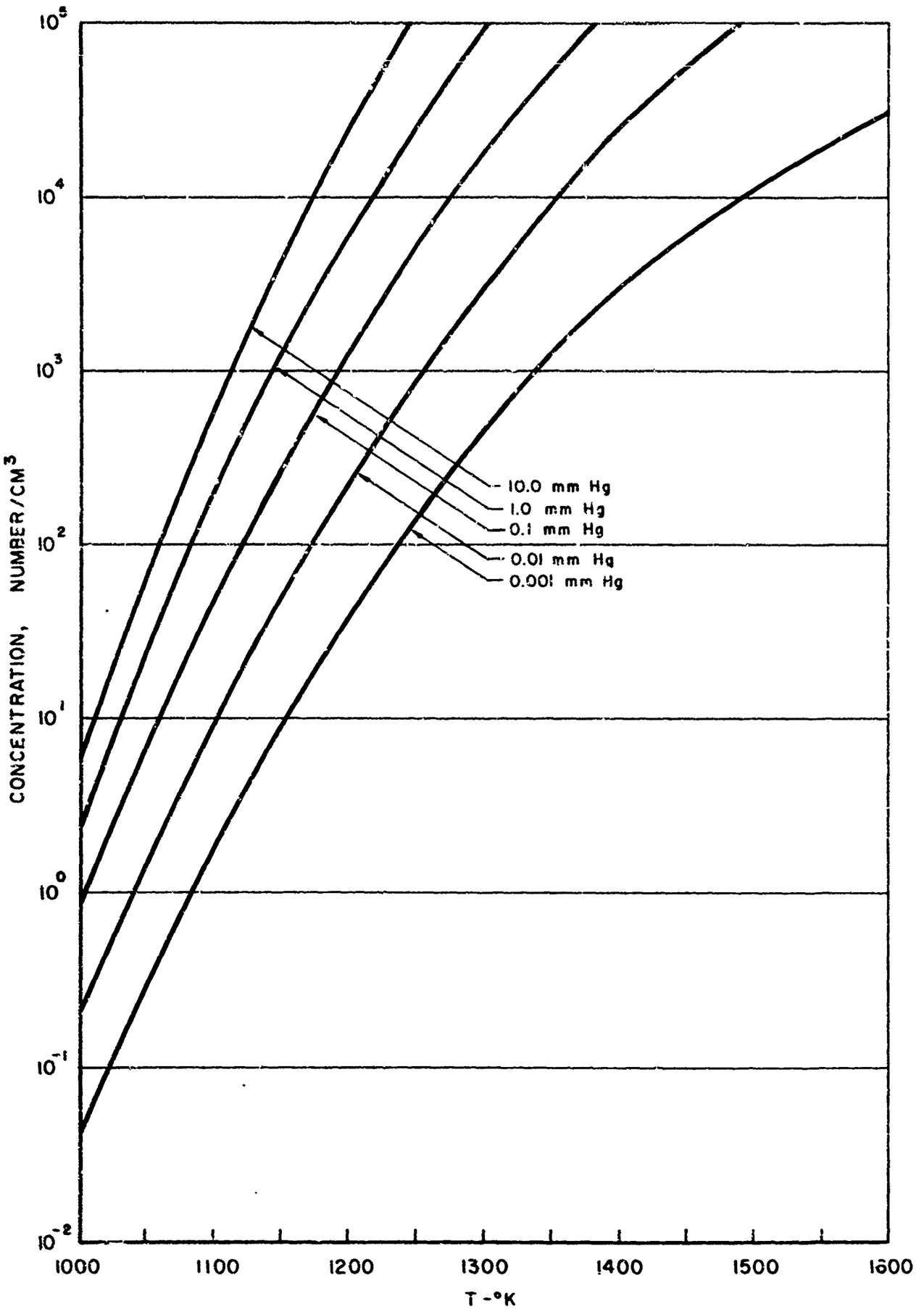

O⁻ CONCENTRATION IN SUPERHEATED NaOH VAPOR

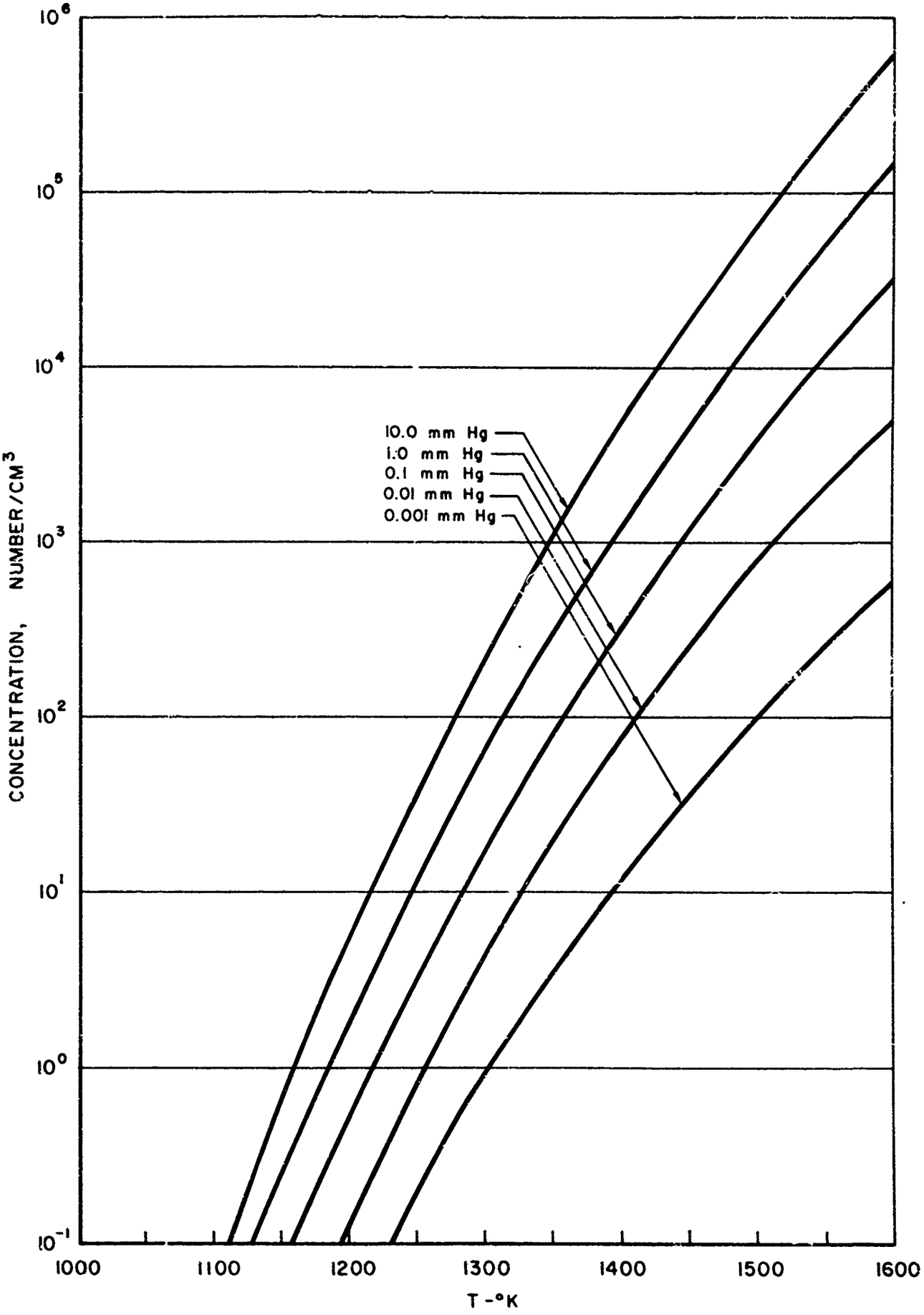

FIG. 20

H^- CONCENTRATION IN SUPERHEATED NaOH VAPOR

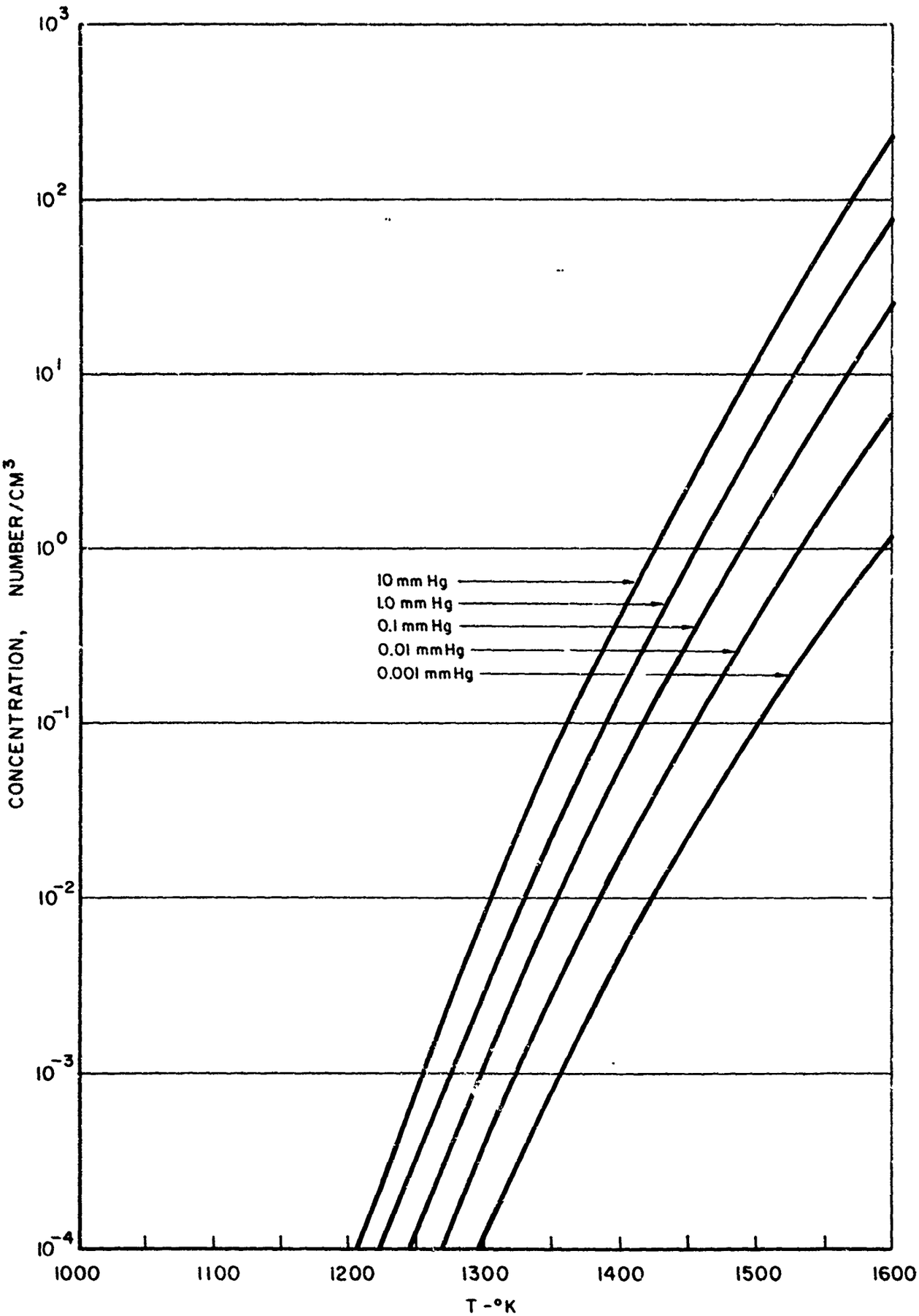

FIG. 21

ELECTRON CONCENTRATION IN NaOH VAPOR WITH EXCESS MgO PRESENT

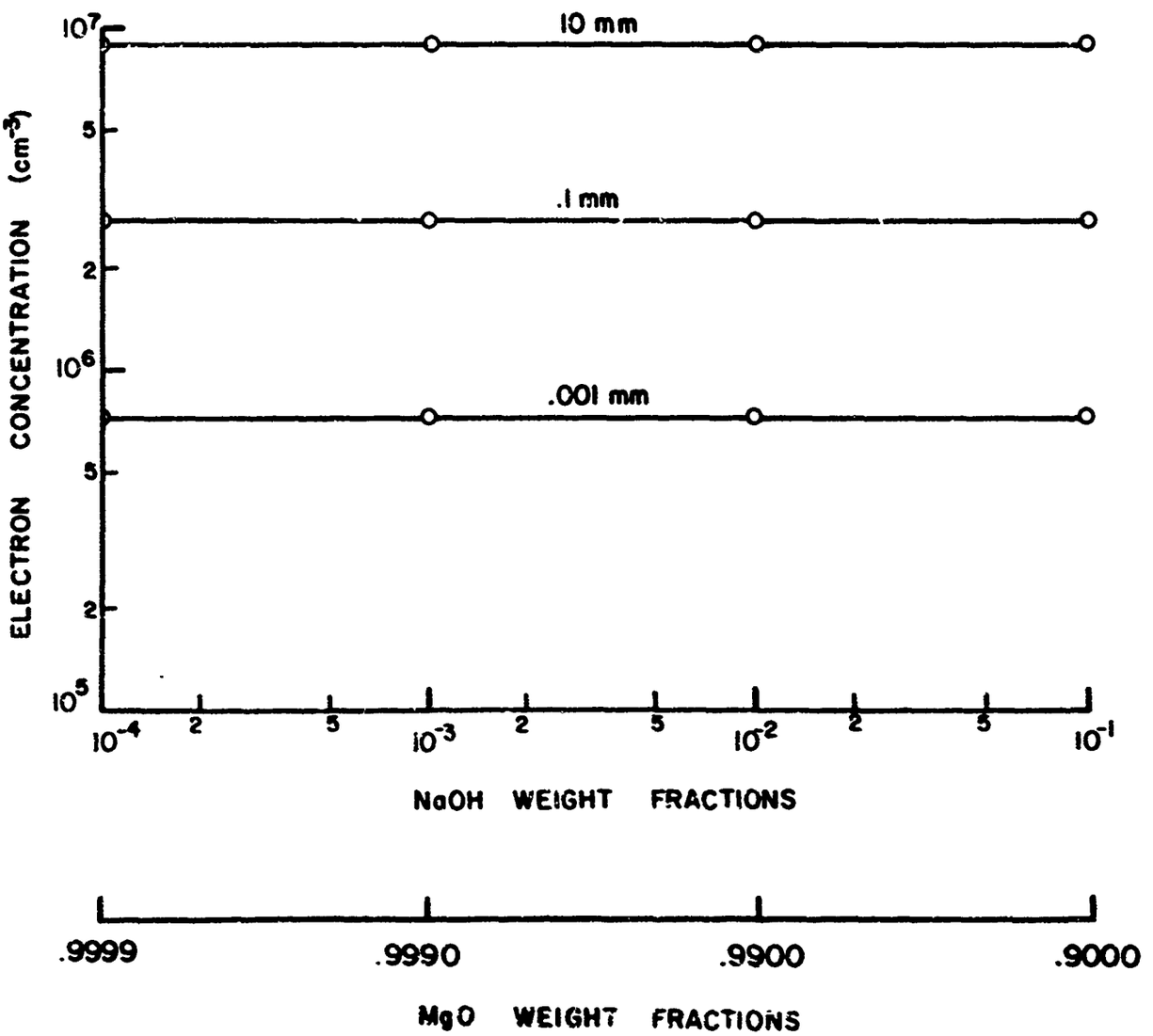

ELECTRON CONCENTRATION IN NaOH VAPOR WITH EXCESS H_2O PRESENT

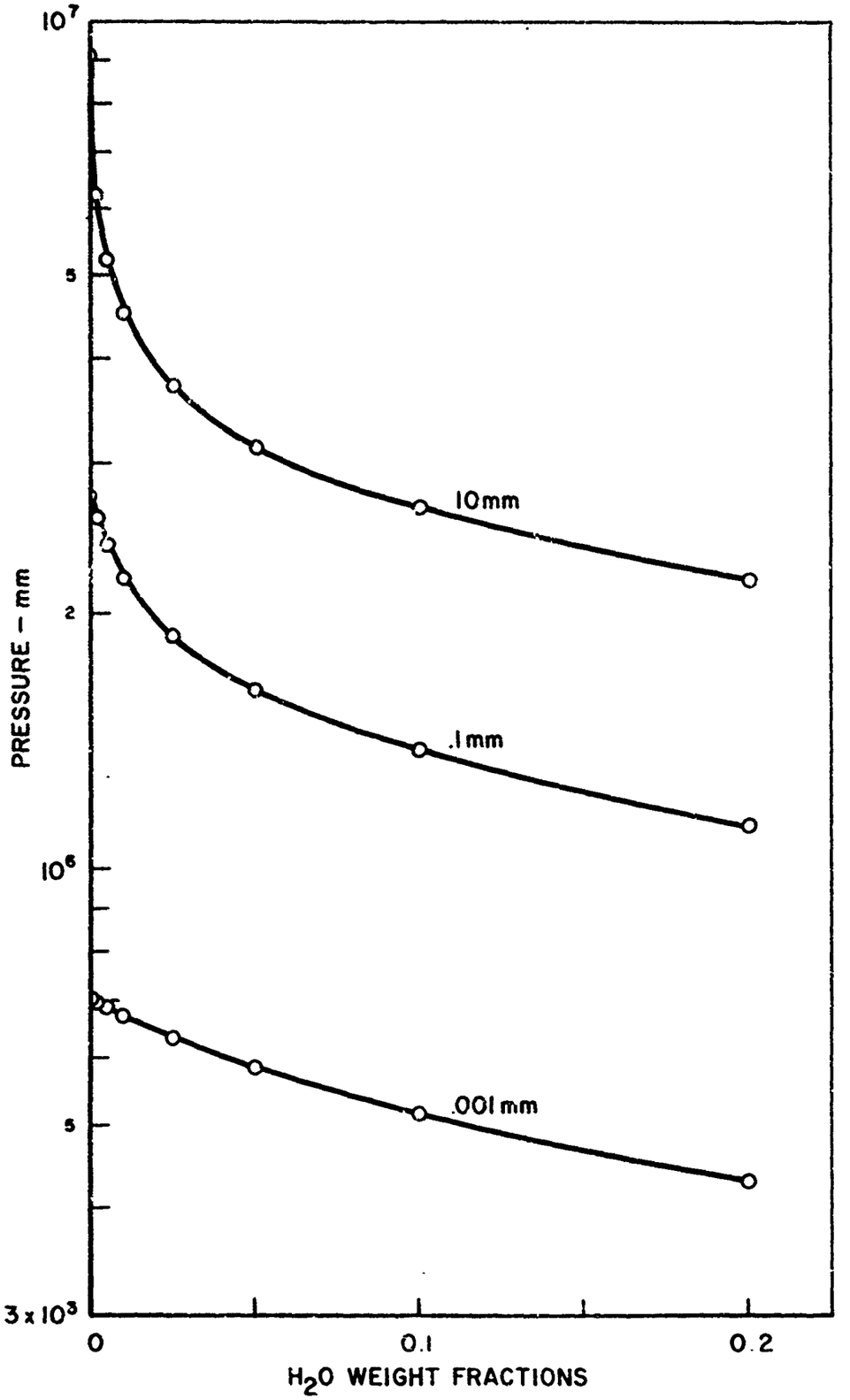

TYPICAL CYCLOTRON RESONANCE ABSORPTION CURVE

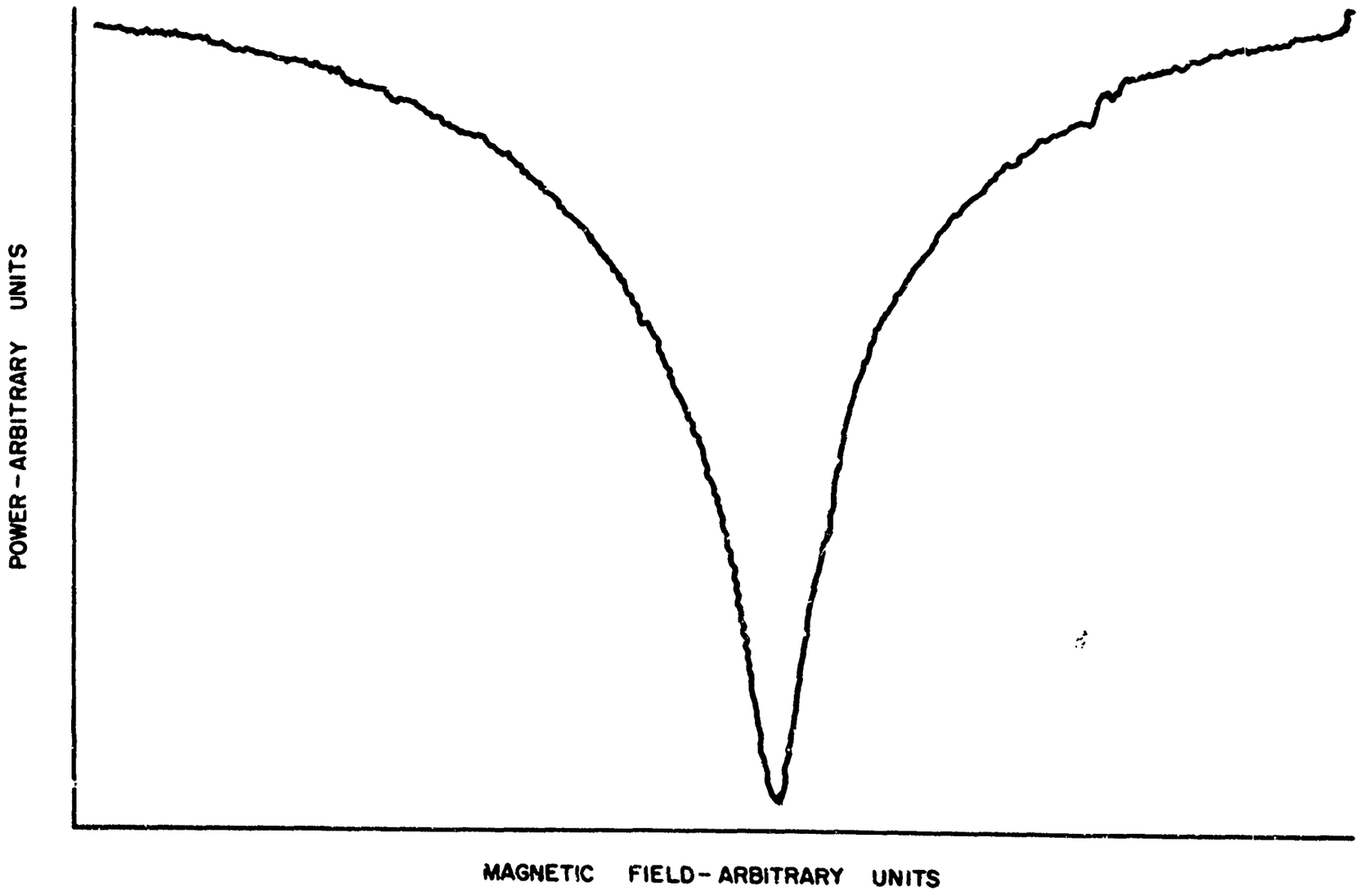

FIG. 24

TABLE OF RESULTS

T (°K)	P (torr)	Ne (per cc)	ν_{eff} (dc) (sec^{-1})	$\Omega_{1/2}$ (sec^{-1})
1162	3.0	3.2×10^6	0.4×10^8	0.9×10^8
1164	3.8	2.4	0.4	1.1
1263	9.2	8.3	1.1	2.9
1265	4.1	3.1	0.4	1.7
1273	8.8	9.2	0.9	2.5
1273	5.9	3.4	0.4	1.3
1277	6.4	4.7	0.5	1.7
1277	4.7	8.6	0.8	2.5
1288	7.6	9.7	0.7	1.6
1294	8.4	1.0×10^7	0.7	1.7
1297	8.8	1.1	0.7	2.3
1300	9.0	1.2	0.8	2.1
1311	10.0	1.5	1.1	3.2
1323	10.1	2.1	1.6	4.2
1347	1.2	1.0	0.2	0.5
1360	10.0	1.6	0.7	3.7
1360	2.4	1.7	0.3	0.8
1362	3.1	1.5	0.3	0.9
1375	11.2	2.4	1.3	3.7
1377	4.8	2.9	0.5	1.2
1410	7.5	1.0×10^8	0.8	1.3
1412	8.3	1.0	0.7	1.4
1446	9.3	1.5	0.7	1.7
1466	9.7	1.9	0.7	1.8

SCHEMATIC OF ION COLLISION CROSS-SECTION APPARATUS

FIG. 1

SCHEMATIC OF ION COLLISION CROSS-SECTION APPARATUS

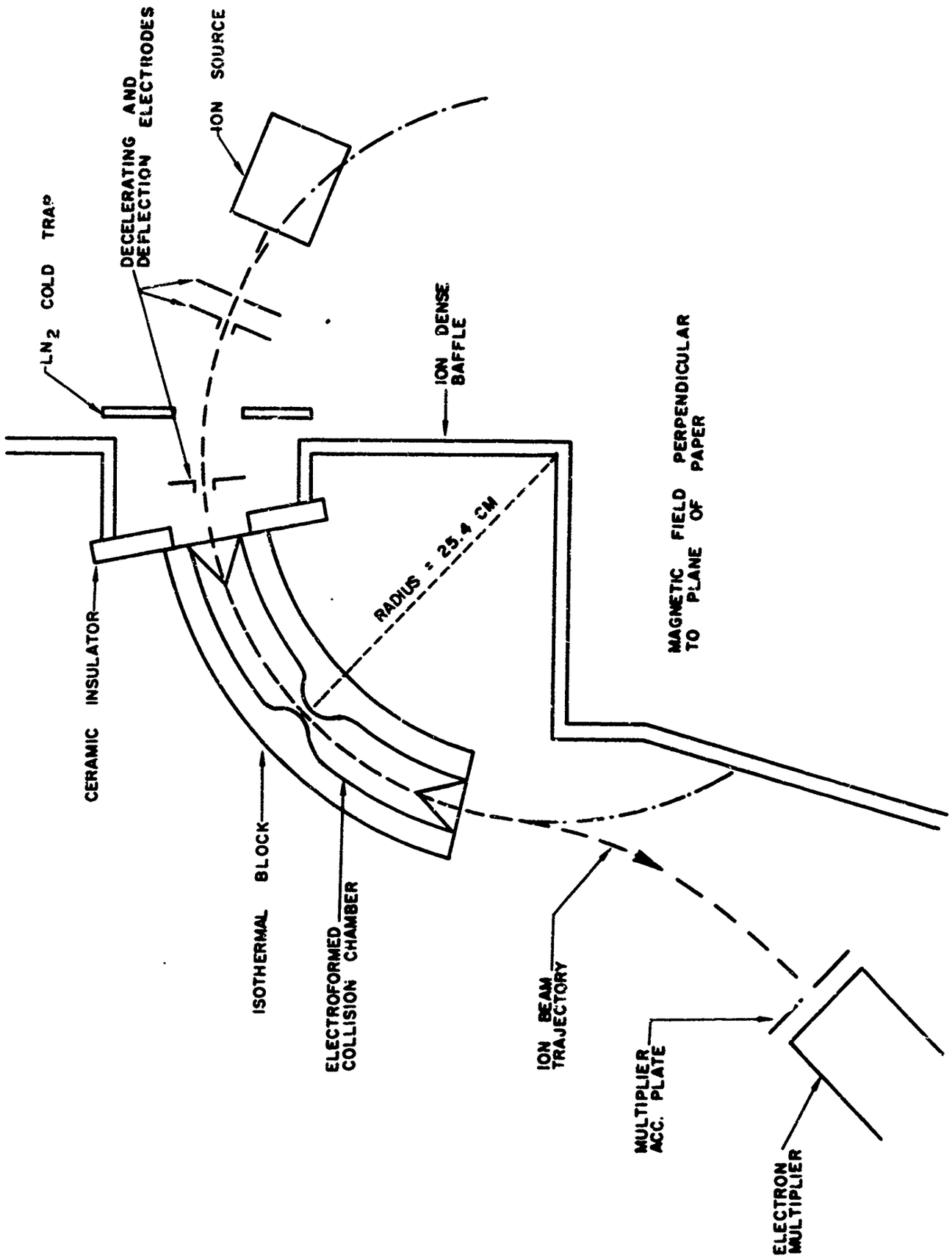

FIG. 26

ION-MOLECULE CROSS-SECTION EXPERIMENT
BAKEABLE ULTRA-HIGH VACUUM SYSTEM

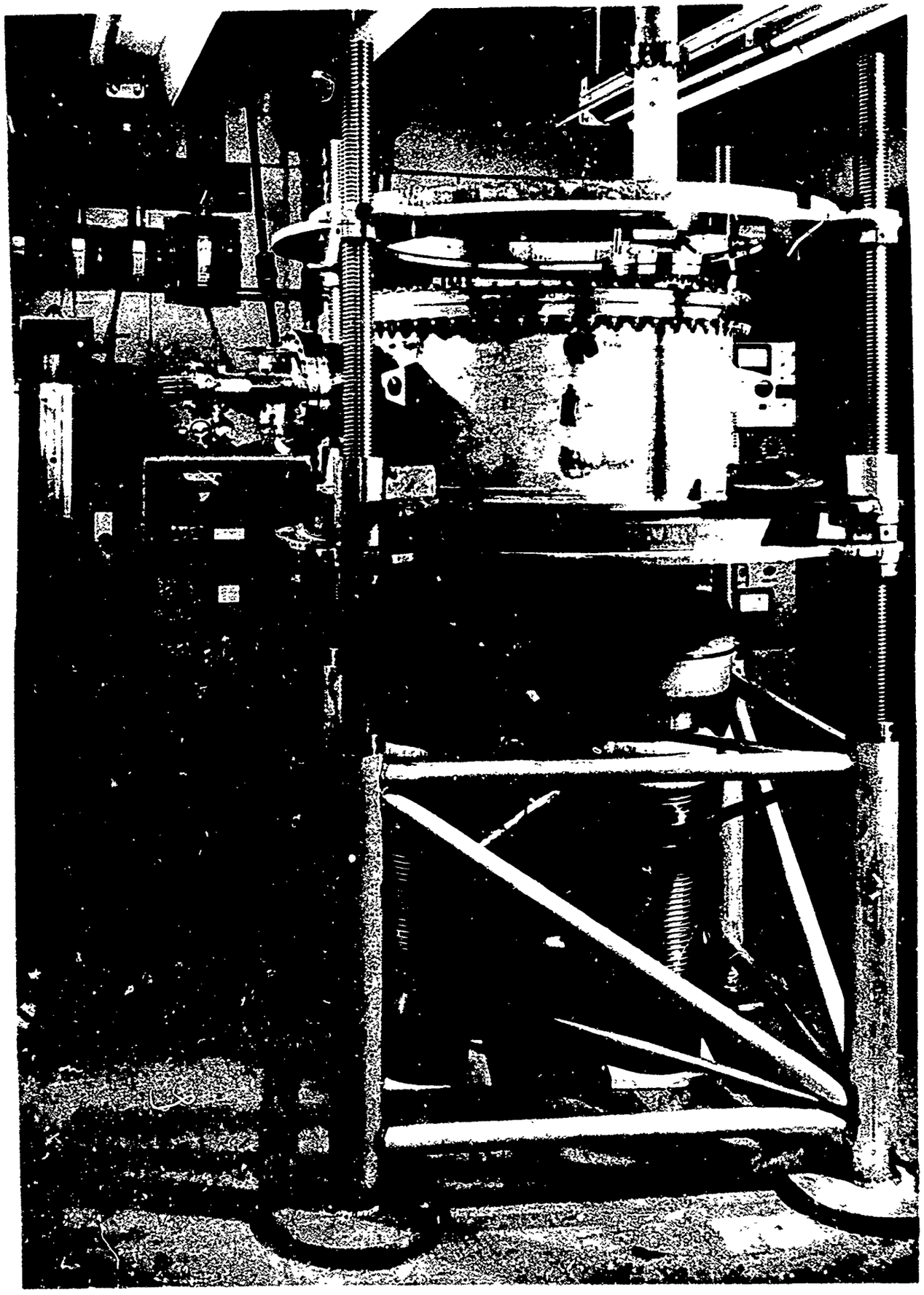

D-920252-6

TARGET GAS FLOW METERING AND CALIBRATION SYSTEM

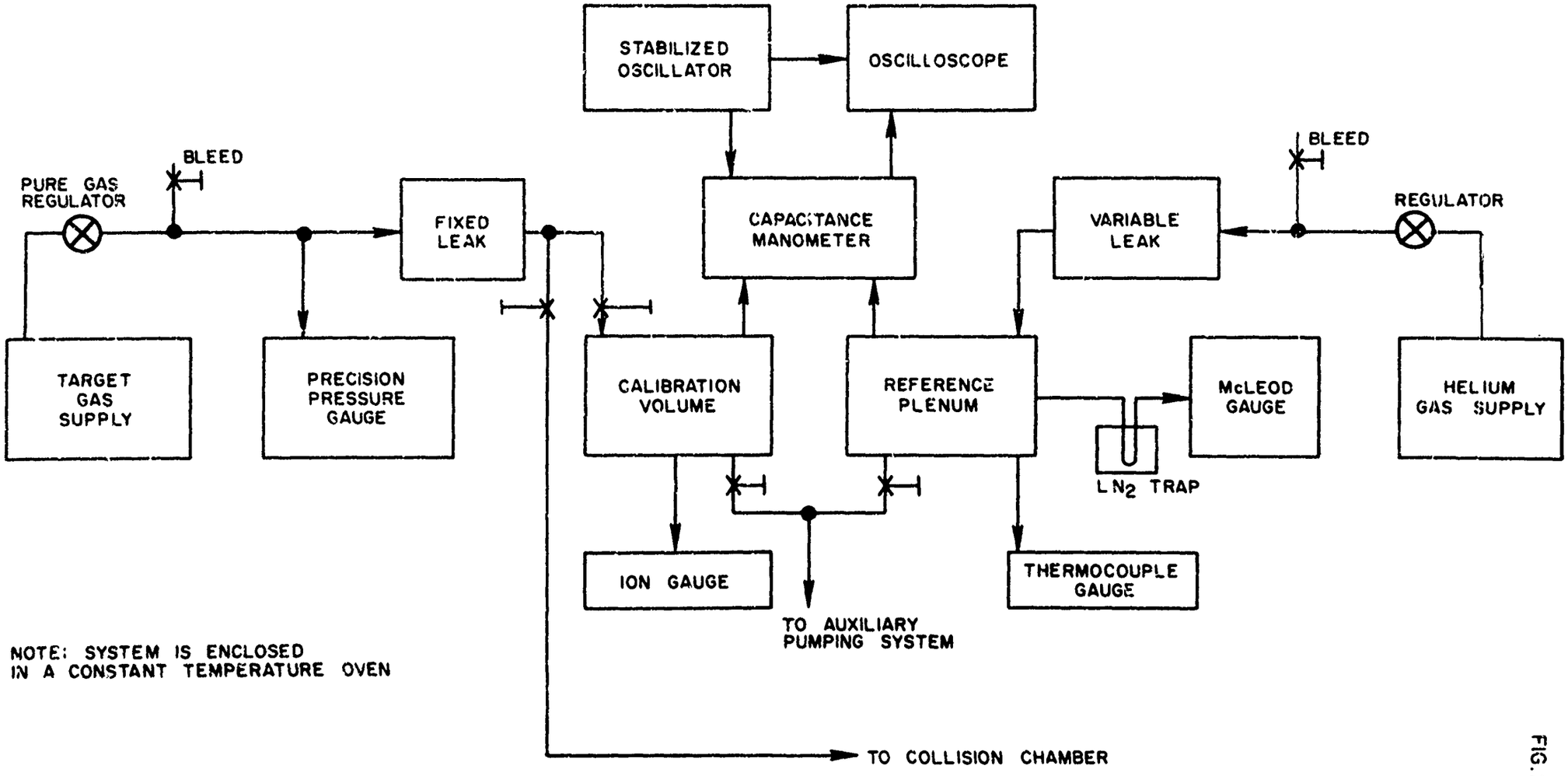

NOTE: SYSTEM IS ENCLOSED IN A CONSTANT TEMPERATURE OVEN

FIG. 27

TARGET - GAS METERING SYSTEM

COLLISION CHAMBER PRESSURE CALIBRATION FOR N_2 AT 25 °C

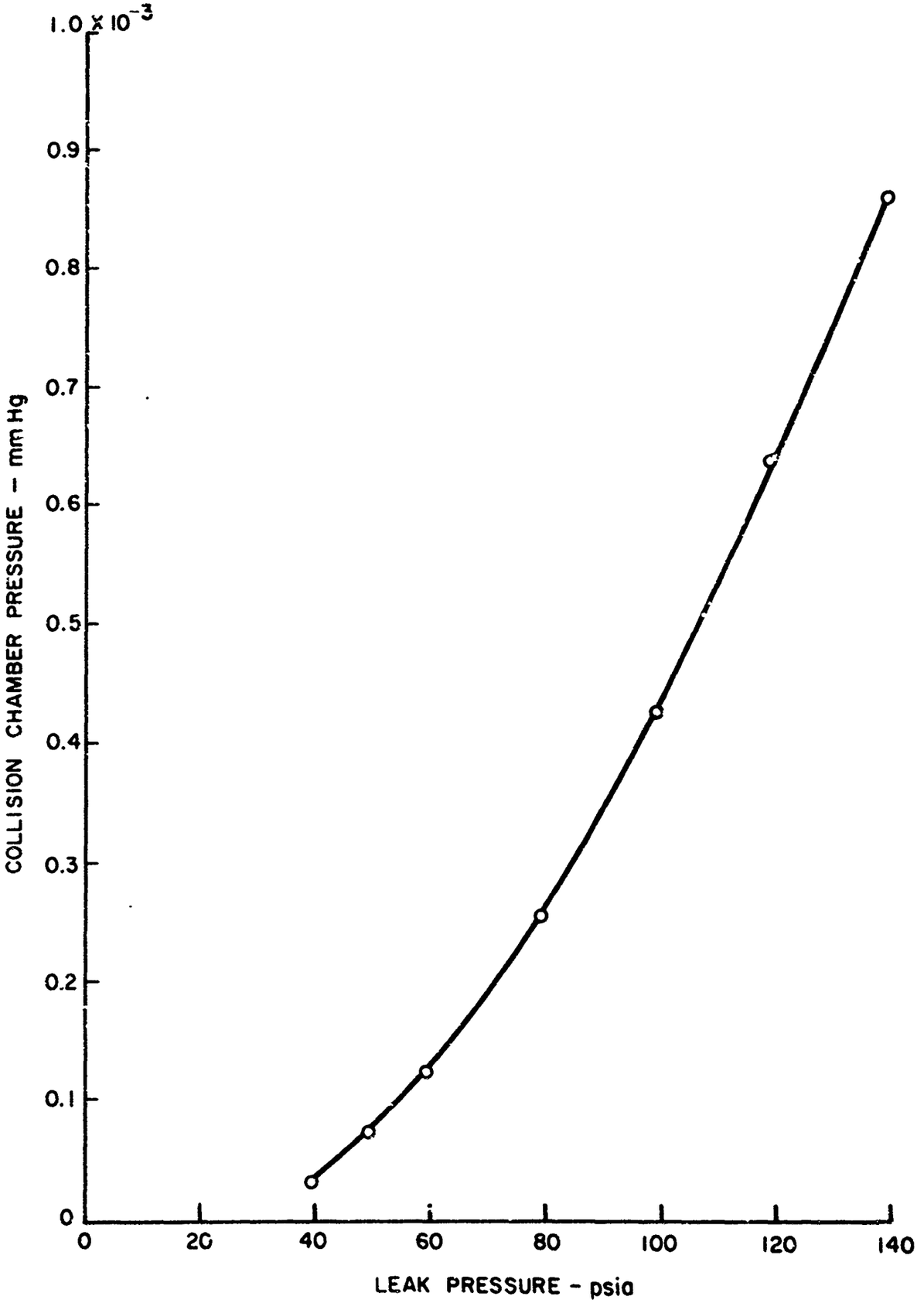

FIG. 30

NORMALIZED ION BEAM ENERGY DISTRIBUTION

WIDTH AT HALF-HEIGHT = 0.81 eV

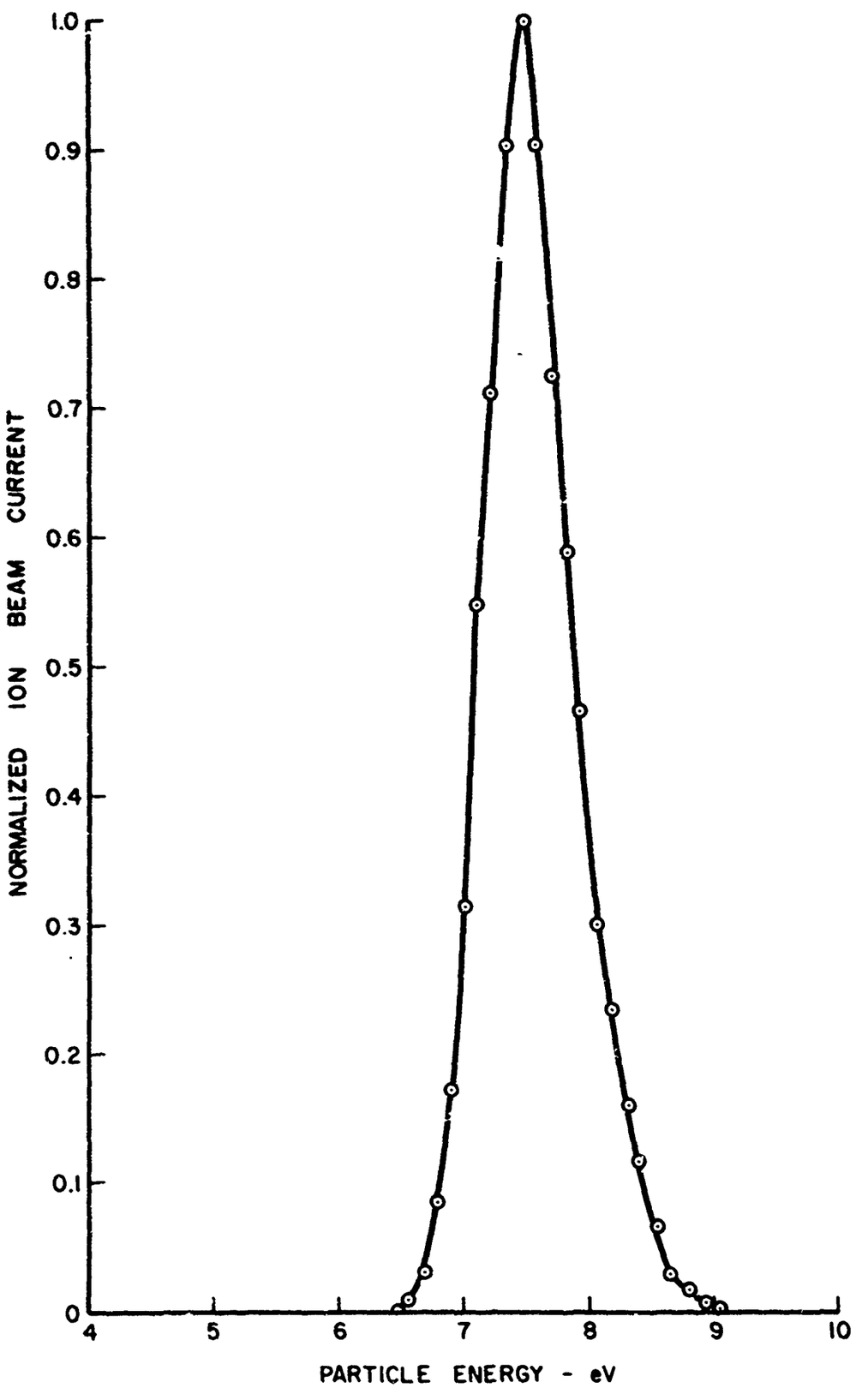

FIG. 31

TYPICAL ION BEAM ATTENUATION WITH INCREASING COLLISION CHAMBER PRESSURE

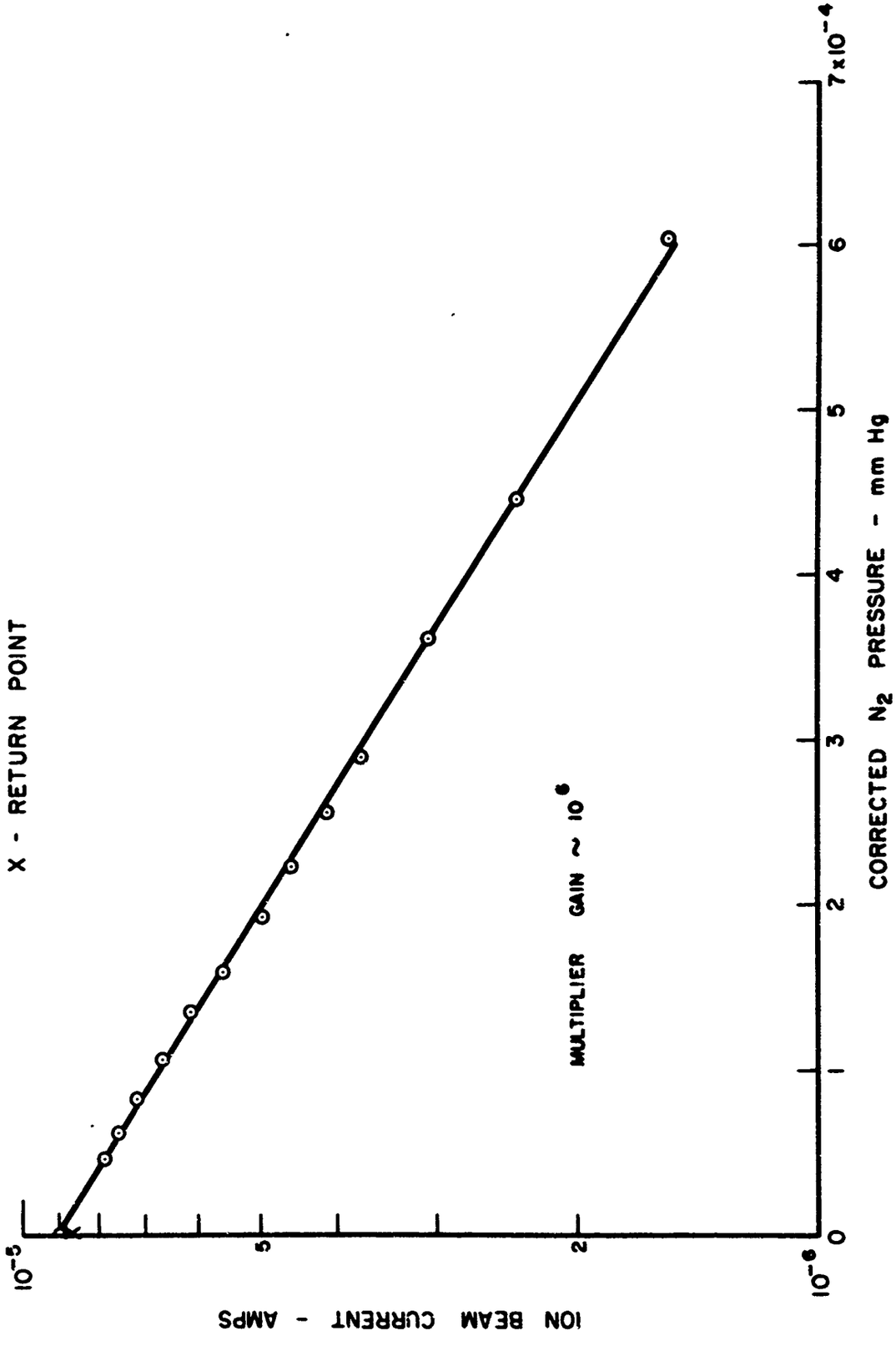

TOTAL COLLISION PROBABILITY FOR SODIUM IONS INTERACTING WITH NITROGEN AT 0 °C

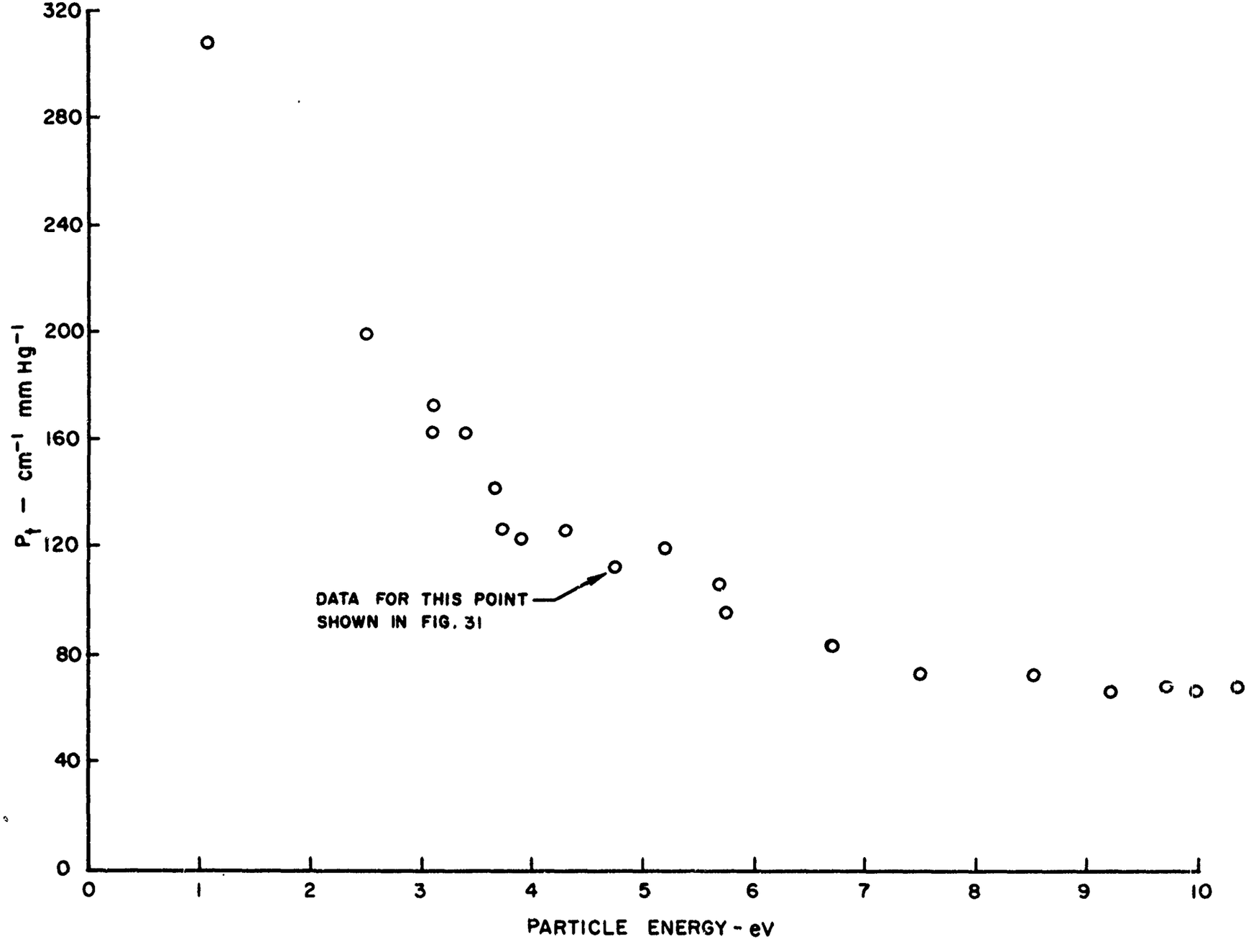

FIG. 32

FIG. 33

TOTAL COLLISION PROBABILITY FOR SODIUM IONS INTERACTING WITH NITRIC OXIDE AT 0°C

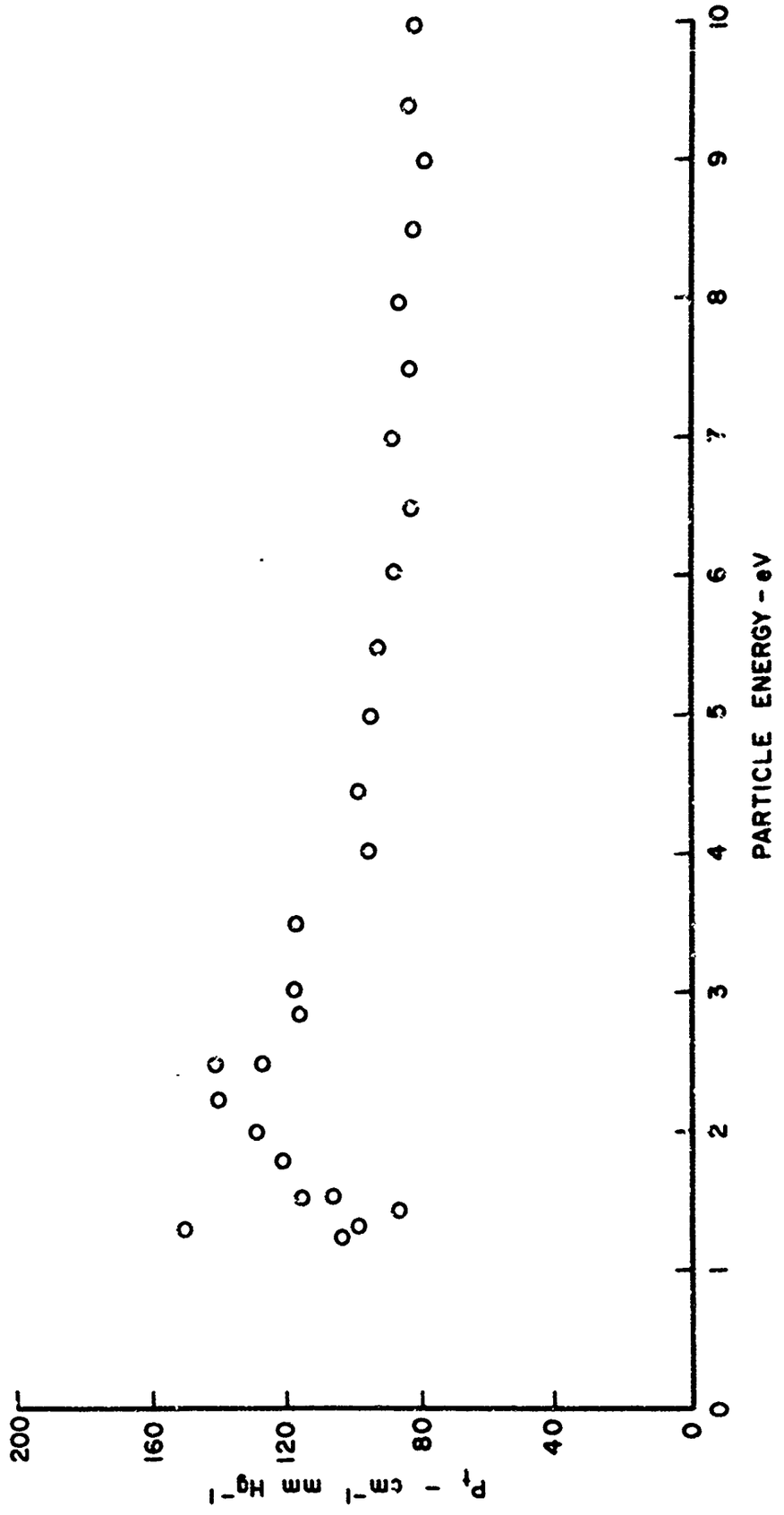

FIG. 34

TOTAL COLLISION PROBABILITY FOR SODIUM IONS INTERACTING WITH OXYGEN AT 0 °C

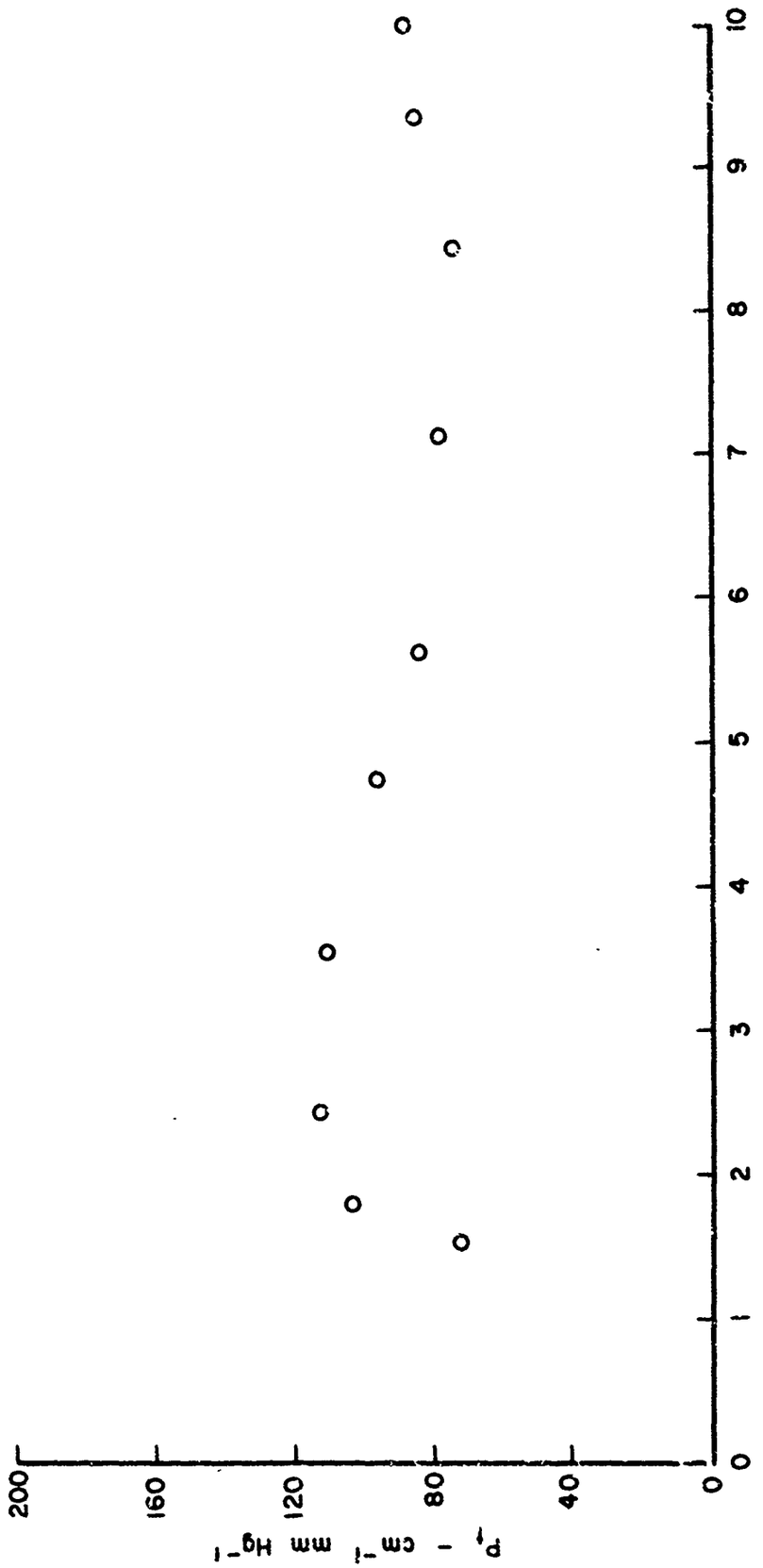

FIG.35

HOLLOW CATHODE ATMOSPHERIC ION SOURCE

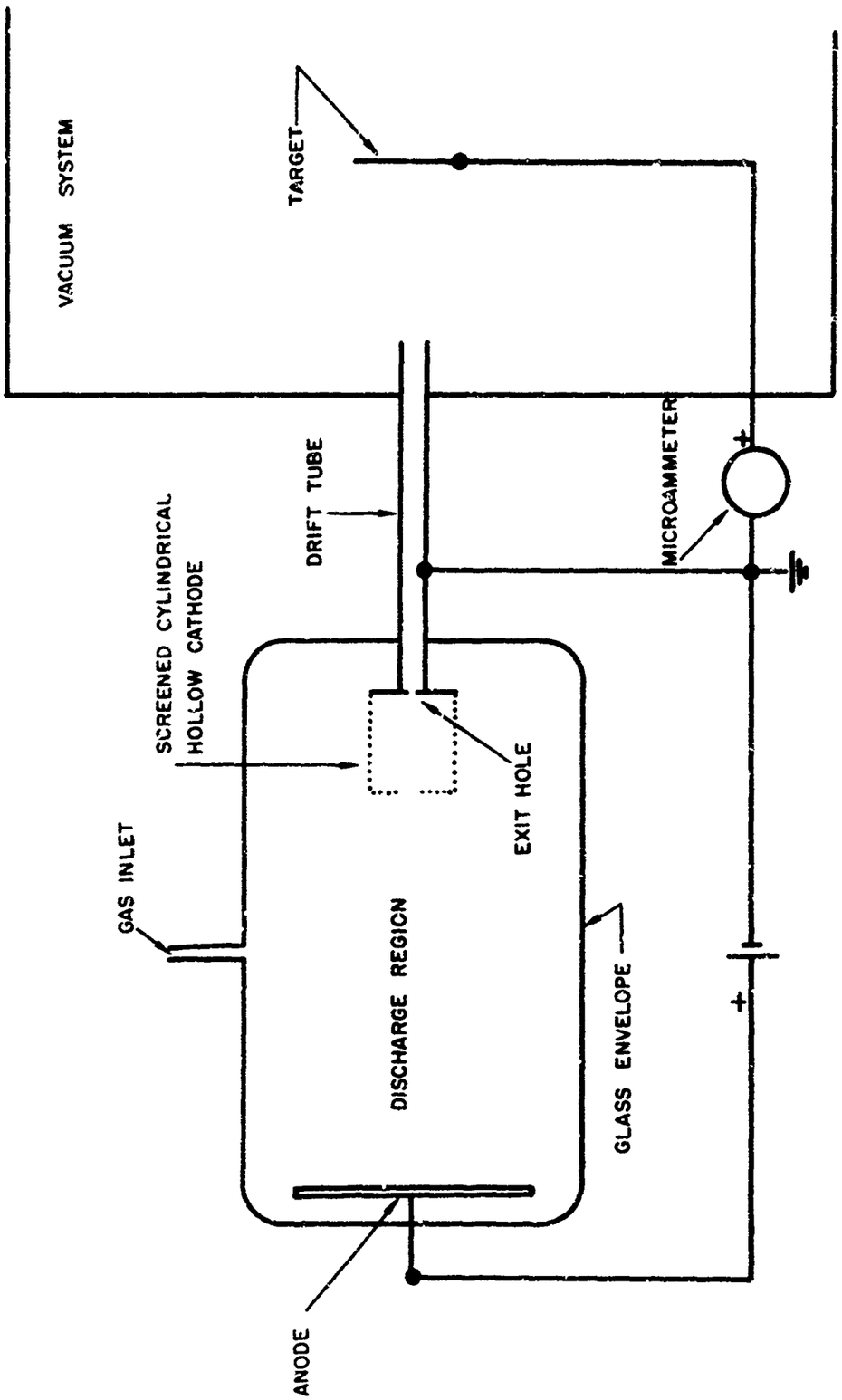

DIAGRAM OF APPARATUS

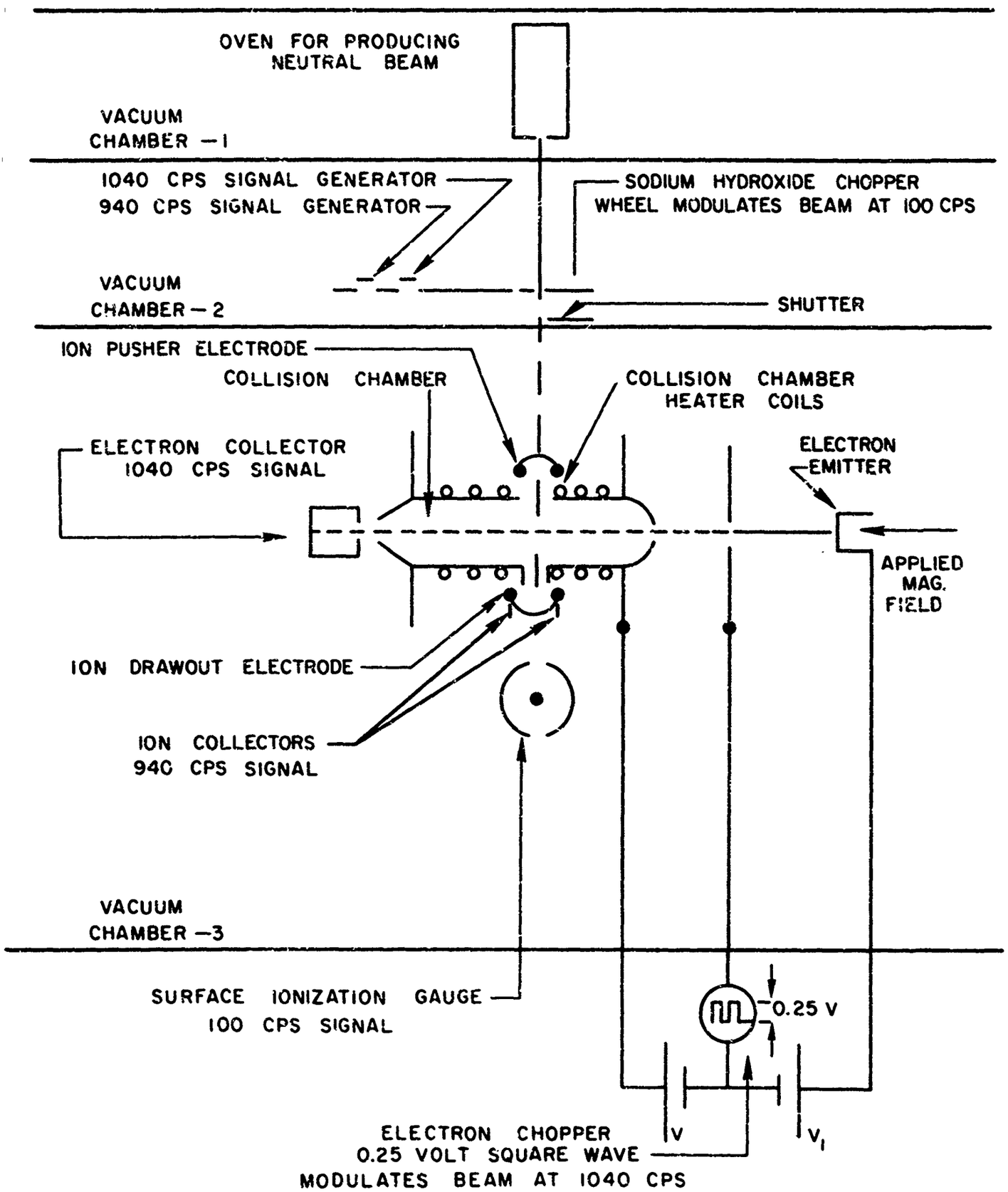

FIG. 37

COPPER COLLISION CHAMBER

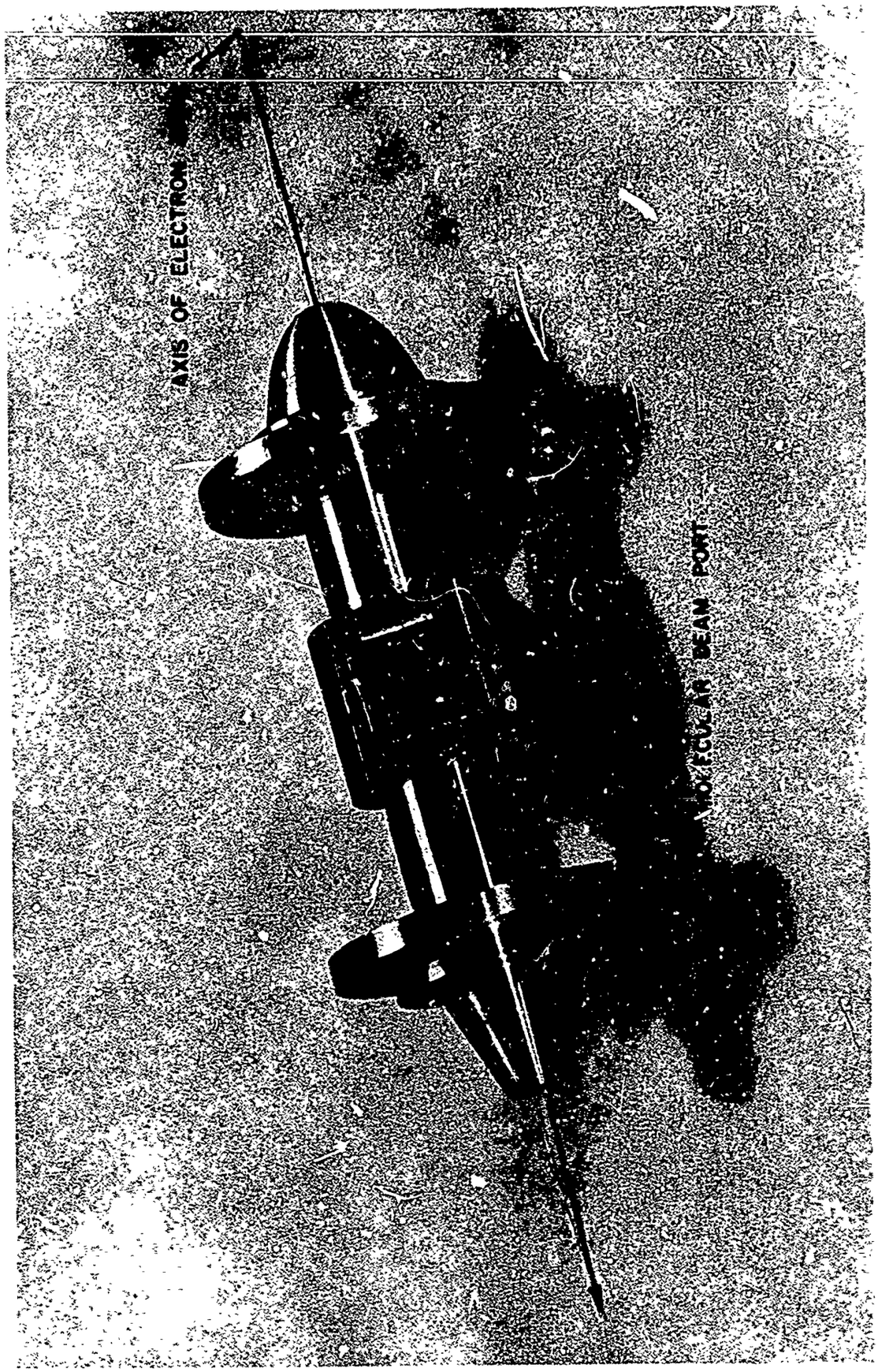

FIG. 38

DIAGRAM OF ELECTRONICS

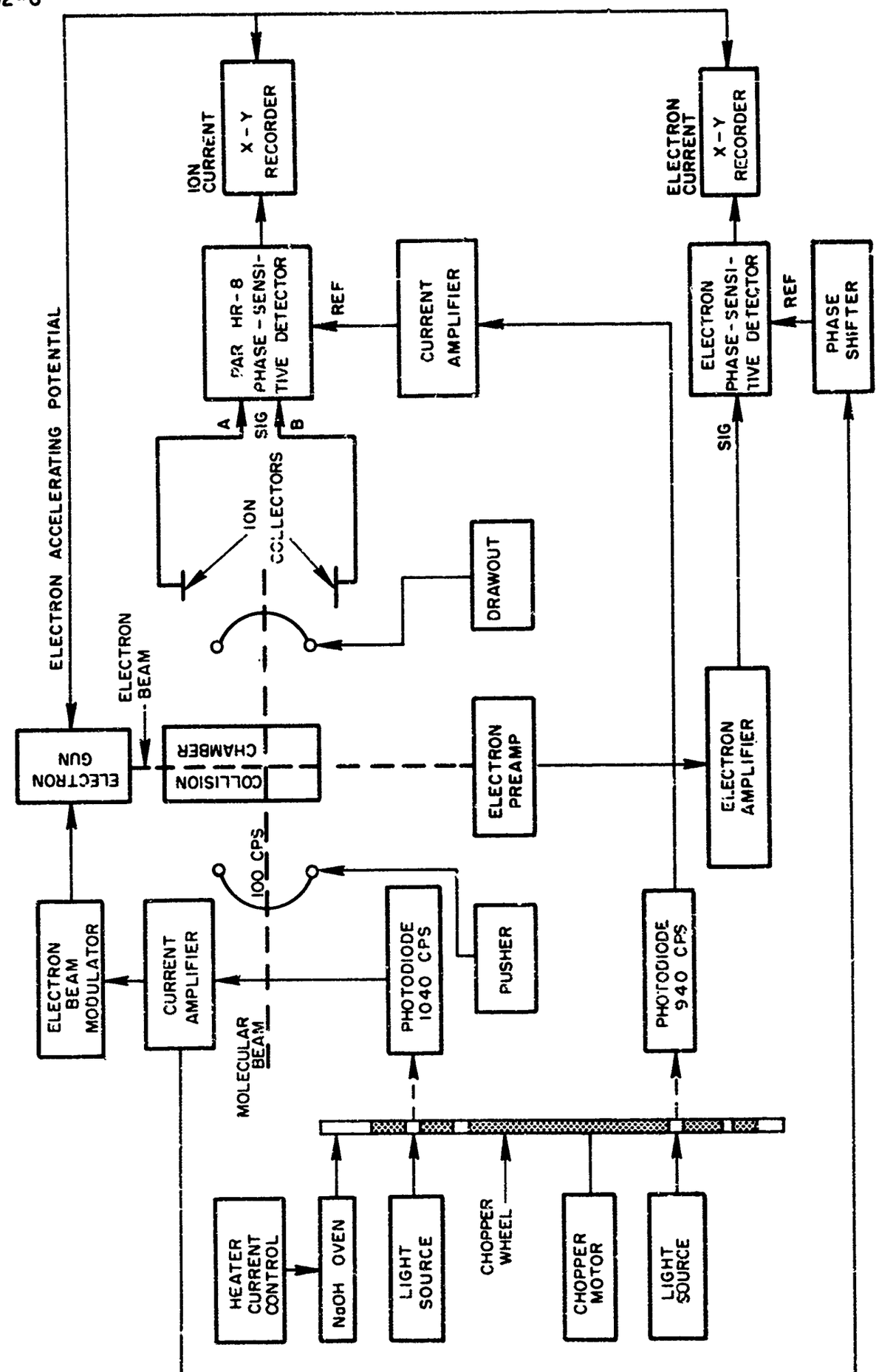

FIG. 39

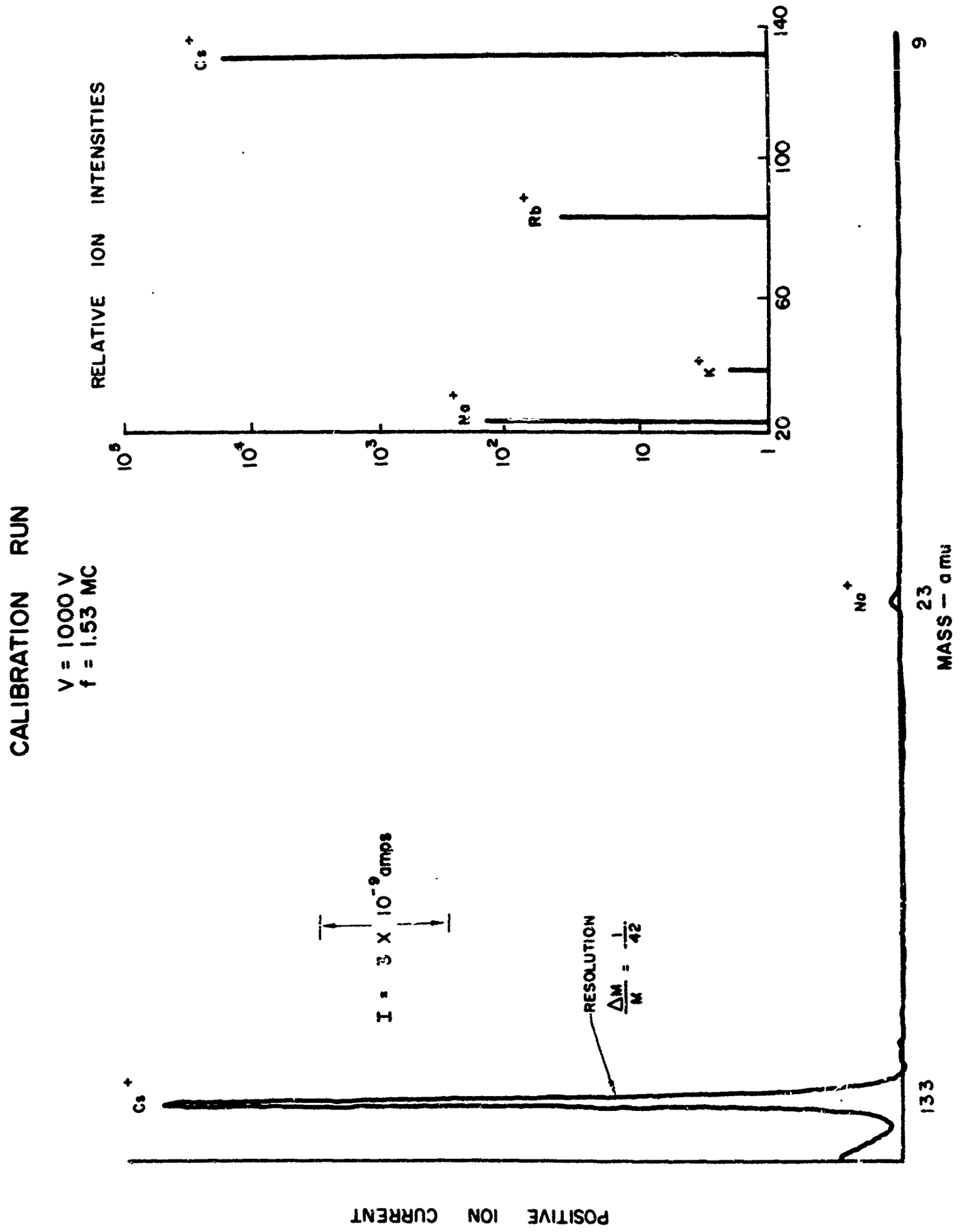
CALIBRATION RUN
V = 1000 V
f = 1.53 MC
RELATIVE ION INTENSITIES
10^5
10^4
10^3
10^2
10
1
20
60
100
140
Na^+
K^+
Rb^+
Cs^+
POSITIVE ION CURRENT
Cs^+
RESOLUTION
$\frac{\Delta M}{M} = \frac{1}{42}$
I = 3 X 10^{-9} amps
Na^+
133
23
9
MASS — amu

FIG. 40

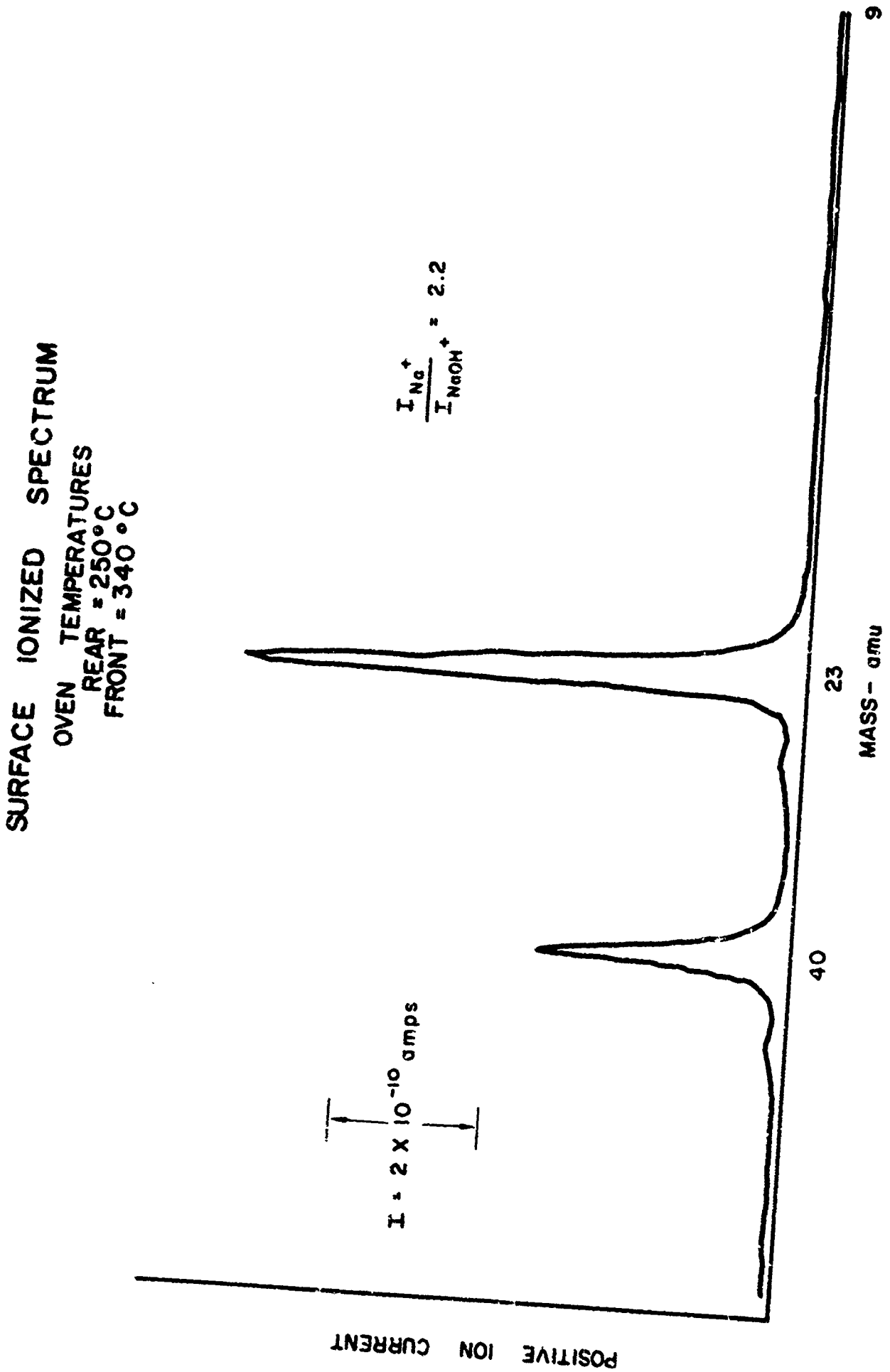
SURFACE IONIZED SPECTRUM
OVEN TEMPERATURES
REAR = 250°C
FRONT = 340 °C
$\frac{I_{Na^+}}{I_{NaOH^+}} = 2.2$
I = 2 X 10⁻¹⁰ amps
POSITIVE ION CURRENT
9
23
40
MASS – amu

FIG. 41

NEGATIVE CURRENT AS A FUNCTION OF ELECTRON ACCELERATING POTENTIAL

(ELECTRON - SODIUM HYDROXIDE INTERACTIONS)

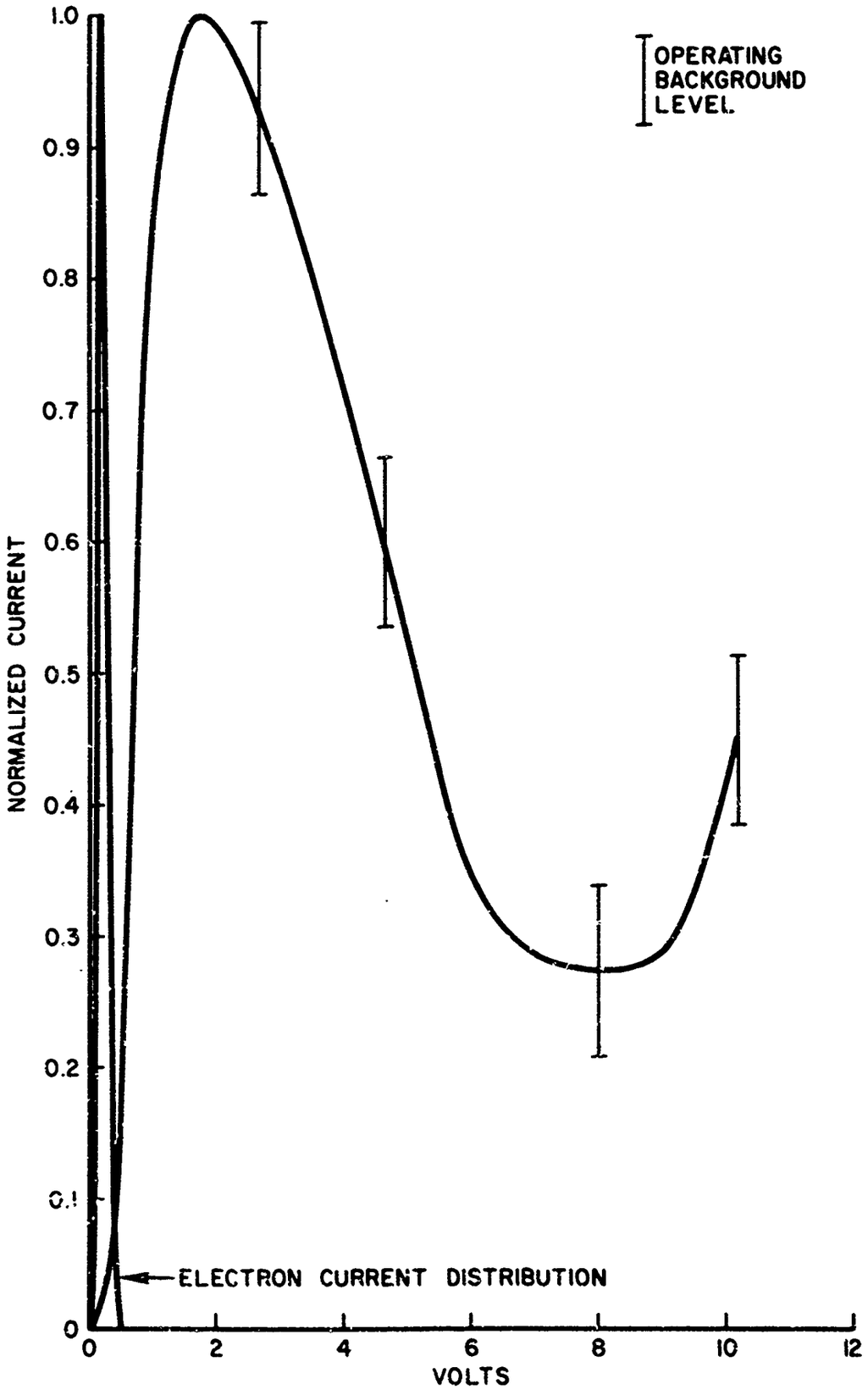

ELECTRON CURRENT AS A FUNCTION OF ELECTRON ACCELERATING POTENTIAL
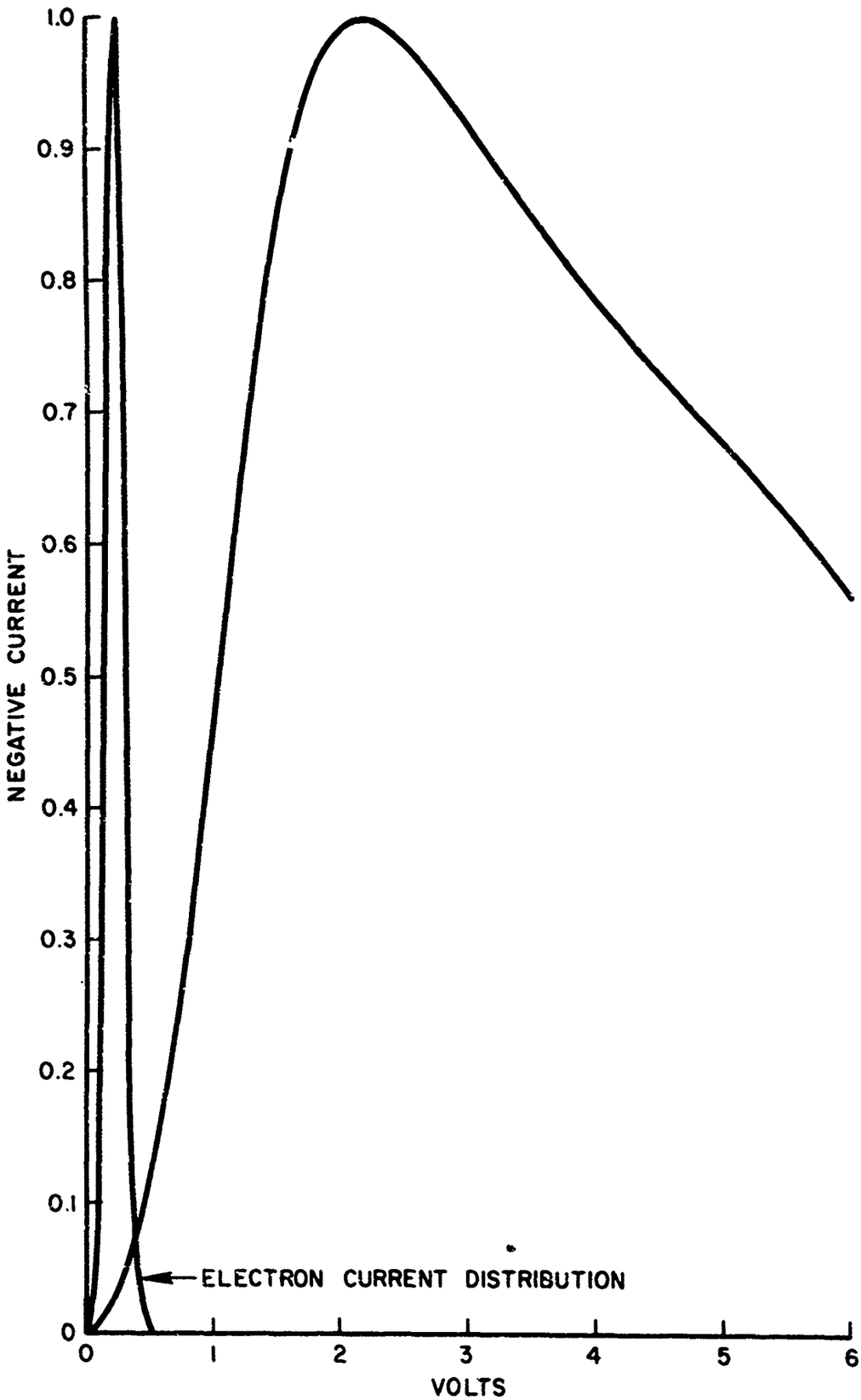
(ELECTRON - HELIUM INTERACTIONS)